

# **Nonequilibrium Spin Noise Spectroscopy on Single Quantum Dots**

Von der Fakultät für Mathematik und Physik  
der Gottfried Wilhelm Leibniz Universität Hannover

zur Erlangung des Grades

Doktorin der Naturwissenschaften

Dr. rer. nat.

genehmigte Dissertation

von

**M.Sc. Julia Susan Wiegand**

**2019**

Referent: Prof. Dr. M. Oestreich  
Korreferent: Prof. Dr. F. Ding  
Korreferent: Prof. Dr. D. Hägele

Tag der Promotion: 28.02.2019

# Abstract

All optical spin noise spectroscopy is typically used to extract the virtually undisturbed spin dynamics from measurements of spin fluctuations in thermal equilibrium. In this thesis, the method is applied to study spin fluctuations in single positively charged InGaAs quantum dots beyond thermal equilibrium conditions, in view of the spin-photon interface provided by the optical transition. Spin noise spectroscopy with a resonantly driven optical transition additionally reveals the spin dynamics in the optically excited state, enables the characterization of the optical transition, and unveils a charge occupation noise which is naturally inherent in optically driven semiconductor quantum dots.

The spin noise measurements in combination with a theoretical model show that the average spin relaxation rate of the optically driven spin is a mixture of hole-spin relaxation in the ground state and electron-spin relaxation in the excited state. The electron-spin relaxation is found to be on the order of a few 10 MHz, and dominates the average spin relaxation rate under quasi-resonant excitation. The dependence of spin dynamics and noise power on the laser detuning is used to determine saturation intensity, line width, and inhomogeneous broadening of the optical transition. It is shown that the unfavorable inhomogeneous broadening due to charge fluctuations in the quantum dot environment becomes very small and can even be absent in high-quality samples with a very low quantum dot density. Beyond the spin relaxation, the spin noise under quasi-resonant driving furthermore contains an additional contribution which is assigned to the temporary escape of the resident hole in the quantum dot. The detailed analysis of this occupation noise shows that the hole escape is initiated by non-radiative Auger recombination. The subsequent reoccupation of the quantum dot depends

crucially on the solid-state environment. The intrinsic Auger rate is determined to be about 2 to 3 MHz for holes in InGaAs quantum dots. The reoccupation of the quantum dot by a hole is in general found to be slow in the investigated weakly  $p$ -doped sample, i.e., on a timescale of a few microseconds. In particular, it is shown that the presence of an ionized acceptor in the close vicinity of the quantum dot can significantly prolong the reoccupation time to several tens of microseconds as the result of a hole-capture competition between ionized acceptor and quantum dot.

**Keywords:** laser spectroscopy, quantum dot, spin dynamics

# Contents

<b>List of Abbreviations, Symbols, and Constants</b>	<b>7</b>
<b>1. Introduction</b>	<b>13</b>
<b>2. General Background</b>	<b>19</b>
2.1. InAs Quantum Dots . . . . .	19
2.1.1. Semiconductor Artificial Atoms . . . . .	19
2.1.2. Optical Properties . . . . .	22
2.1.3. Spin Dynamics . . . . .	31
2.2. Spin Noise Spectroscopy . . . . .	38
2.2.1. Spin Fluctuations and Noise Spectrum . . . . .	39
2.2.2. Faraday and Kerr Rotation . . . . .	42
<b>3. Experimental Aspects</b>	<b>49</b>
3.1. Sample: Quantum Dots in a Microcavity . . . . .	49
3.2. Low-Temperature Confocal Microscope . . . . .	53
3.3. Photoluminescence . . . . .	56
3.4. Spin Noise Spectroscopy . . . . .	60
3.4.1. Measurement of Kerr Rotation Noise . . . . .	60
3.4.2. Spin Noise Spectrum and Projection of Spin Components . . . . .	62
3.4.3. Background Noise and Detector Response Func- tion . . . . .	65
<b>4. Measurements &amp; Results</b>	<b>69</b>
4.1. Homogeneous Broadening and Reoccupation Noise . . . . .	70
4.1.1. Homogeneous Noise Power Spectrum . . . . .	70
4.1.2. Quasiresonant Spin Noise Spectra . . . . .	72
4.1.3. Theoretical Model . . . . .	75

4.1.4.	Nonequilibrium Spin Noise . . . . .	80
4.1.5.	Occupation Noise . . . . .	83
4.2.	Inhomogeneous Broadening and Acceptor-Occupation Noise . . . . .	90
4.2.1.	A More Complex Form of Occupation Noise .	91
4.2.2.	Broadening due to Slow Charge Fluctuations	94
4.2.3.	Theoretical Model of Coupled Spin and Charge Dynamics . . . . .	96
4.2.4.	Comparison of Experiment and Theory . . .	103
<b>5.</b>	<b>Conclusion &amp; Outlook</b>	<b>111</b>
	<b>Appendices</b>	<b>117</b>
	<b>A. Additional Information on the Sample</b>	<b>119</b>
	<b>B. Alternative Models of Charge Dynamics</b>	<b>123</b>
	<b>Bibliography</b>	<b>131</b>
	<b>List of Figures</b>	<b>149</b>
	<b>CV &amp; Publications</b>	<b>151</b>
	<b>Acknowledgements</b>	<b>157</b>

# List of Abbreviations, Symbols, and Constants

## Abbreviations

**AAs** Aluminum Arsenide

**DBR** Distributed Bragg Reflector

**FFT** Fast Fourier Transformation

**FWHM** Full Width at Half Maximum

**GaAs** Gallium Arsenide

**HFI** Hyperfine Interaction

**HWHM** Half Width at Half Maximum

**InAs** Indium Arsenide

**(InGa)As** Indium Gallium Arsenide

**LCR** Liquid Crystal Retarder

**MBE** Molecular Beam Epitaxy

**ML** Monolayer

**ON** Occupation Noise

**PL** Photoluminescence

**PSU** Photon Shot-noise Units

**QD** Quantum Dot

**SN** Spin Noise

**SNS** Spin Noise Spectroscopy

## Symbols

$B_x$  transversal magnetic field

$B_z$  longitudinal magnetic field

$B_N$  nuclear magnetic field

$d$  transition dipole moment

$E$  electric field

$\mathcal{E}$  trion optical transition matrix element

$G$  generation rate

$g_e$  electron g-factor

$g_h$  hole g-factor

$I$  laser intensity

$I_S$  saturation intensity of the optical transition

$\tilde{n}$  complex refractive index

$n_h$  population of the QD ground state (hole)

$n_{\text{tr}}$  population of the QD excited state (trion)

$n$  QD population,  $n = n_h + n_{\text{tr}}$

$n_{\text{out}}$  population of states outside the QD

$P$  power



$R$  recombination rate  
 $S_z$  spin projection on the measurement direction  $z$   
 $S_z^e$  electron-spin projection  
 $S_z^h$  hole-spin projection  
 $T$  temperature  
 $T_1$  spin relaxation time  
 $T_1^e$  electron-spin relaxation time  
 $T_1^h$  hole-spin relaxation time  
 $\tilde{T}_1$  average spin relaxation time  
 $T_2$  spin dephasing time  
 $T_2^*$  inhomogeneous spin dephasing time  
 $X^0$  exciton  
 $X^{1+}$  positively charged trion  
 $\Delta E_{\text{FS}}$  fine-structure splitting energy  
 $\alpha$  primary noise contribution in the SN spectrum  
 $\beta$  additional noise contribution in the SN spectrum (ON)  
 $\gamma$  intrinsic transition linewidth  
 $\gamma_0$  spontaneous recombination rate  
 $\gamma_A$  Auger rate  
 $\tilde{\gamma}_A$  effective Auger rate  $\propto n_{\text{tr}}/n \cdot \gamma_A$   
 $\gamma_I$  transition linewidth at a given laser intensity,  $\gamma_I = \gamma\sqrt{1 + I/I_S}$   
 $\gamma_n$  correlation rate of the occupation noise

$\gamma_r$  reoccupation rate

$\gamma_s$  spin relaxation rate

$\gamma_s^e$  electron-spin relaxation rate,  $\gamma_s^e = 1/T_1^e$

$\gamma_s^h$  hole-spin relaxation rate,  $\gamma_s^h = 1/T_1^h$

$\gamma_{C,D}$  reoccupation rate from continuum into the QD

$\gamma_{C,O}$  reoccupation rate from continuum into the outer state

$\gamma_{O,D}$  reoccupation rate from the outer state into the QD

$\Gamma$  renormalized  $\gamma_I$  of the nonequilibrium noise power spectra

$\delta\omega_0$  inhomogeneous broadening of the optical transition

$\Delta$  laser detuning with respect to the optical resonance,  $\Delta = \omega - \omega_0$

$\Delta_+$  effective laser detuning for  $\sigma^-$  polarized light,  $\Delta_+ = \Delta + \Omega_z/2$

$\Delta_-$  effective laser detuning for  $\sigma^+$  polarized light,  $\Delta_- = \Delta - \Omega_z/2$

$\epsilon$  dielectric function

$\theta_F$  Faraday rotation angle

$\theta_K$  Kerr rotation angle

$\lambda$  coupling parameter between QD pseudo spin and occupancy

$\lambda'$  coupling parameter between QD occupancy and pseudo spin

$\nu$  noise frequency

$\nu_L$  Larmor frequency

$\sigma^-$  right-handed circular polarization

$\sigma^+$  left-handed circular polarization

$\omega_0$  resonance frequency

$\omega$  laser frequency

$\Omega_z^h$  Larmor frequency corresponding to the Zeeman splitting  $\hbar\Omega_z^h$  of the hole-spin states in  $z$ -direction

$\Omega_z^e$  Larmor frequency corresponding to the Zeeman splitting  $\hbar\Omega_z^e$  of the electron-spin states in  $z$ -direction

$\Omega_z$  Larmor frequency corresponding to the effective trion Zeeman splitting  $\hbar\Omega_z = \hbar\Omega_z^e - \hbar\Omega_z^h$  in  $z$ -direction

## Constants

$c$  speed of light,  $299\,792\,458\text{ m s}^{-1}$

$e$  elementary charge,  $1.602\,176\,62 \times 10^{-19}\text{ C}$

$h$  Planck's constant,  $6.626\,070\,040 \times 10^{-34}\text{ J s}$

$\hbar$  reduced Planck constant,  $1.054\,571\,800 \times 10^{-34}\text{ J s}$

$k_B$  Boltzmann constant,  $1.380\,648\,52 \times 10^{-23}\text{ J K}^{-1}$

$\mu_B$  Bohr magneton,  $9.274\,009\,994 \times 10^{-24}\text{ J T}^{-1}$



# 1. Introduction

A single spin in conjunction with an optical transition is among the most popular systems considered in the context of quantum information processing. The spin provides a two-level quantum system, referred to as qubit, which can be interrogated and controlled by laser light. The superposition principle inherent to such a quantum system can be exploited to enhance the performance of information processing beyond the capabilities of a classical computer [1, 2].

The general concept of a qubit can be realized in many different systems. A naturally occurring well-isolated qubit system is provided by two levels in an (ionized) atom. In this system, encouraging experiments involving the realization of computational tasks by optical control of the qubit have been demonstrated within the last decade [3–8]. However, single atoms are extremely volatile and considerable effort is necessary to store them in a fixed spatial position. This fact makes the future utilization of atoms for common quantum information devices rather unfavorable. In order to circumvent this problem, the realization of a qubit in a solid-state system is very desirable. The technological progress in the fabrication of semiconductor nanostructures provides a high-potential candidate for an optically addressable spin qubit: nanometer-sized indium arsenide dots embedded in gallium arsenide yield a three dimensional trapping potential for charge carriers with a spin. The strong confinement in these so-called quantum dots (QDs) results in quantized energy levels for the confined carriers and bright optical transitions at discrete photon energies. Optical studies on QDs reproduced most of the characteristic quantum optical phenomena shown for atoms. For example, QDs exhibit single photon emission which is observed as photon anti-bunching in intensity correlation measurements [9, 10]. Furthermore, Rabi oscillations and the Mollow-triplet

can be observed in optically driven QDs [11–13], which signifies strong, coherent light-matter interaction. The striking similarity to the physical properties of a single atom coined the term artificial atom, although a QD typically consists of more than ten thousand atoms. To some extent the artificial atoms might even be superior to real atoms: the level structure and optical emission energy can be tailored by varying QD size and material composition. This enables the fabrication of QDs which emit light, for example, at telecom band wavelengths [14, 15]. In addition, the optical transition of a semiconductor QD has typically a much larger oscillator strength compared to an atomic transition, providing a significantly higher photon yield. Furthermore, the solid-state implementation facilitates the incorporation of QDs into existing semiconductor optoelectronic structures to build up technologically relevant, scalable devices. Regarding quantum-information applications, several groups demonstrated the optical initialization, manipulation, and read-out of a single electron spin confined in a QD [16–20], which represent some of the key requirements for the physical implementation of a qubit [21]. An important parameter in this context is the spin relaxation or decoherence time, which defines the timescale on which a spin information can be maintained by the qubit. Ideally, this time should be as long as possible. Here, the otherwise convenient solid-state environment poses a major challenge for the realization of a suitable qubit. The solid-state matrix constitutes a rich source of noise and interactions which usually lead to a rapid loss of the spin information. At low temperatures, the spin decay of a carrier confined in the QD is dominated by the hyperfine interaction with the huge number of atomic nuclear spins in the QD [22, 23]. This interaction causes a fast electron spin decay within a few nanoseconds. The detrimental effect of the hyperfine interaction can be mitigated by using a hole spin instead of an electron spin. As a result of its  $p$ -type Bloch wave function, the hole spin interacts only weakly with the nuclear spins which yields a significantly longer hole-spin lifetime [24, 25]. The spin decay due to hyperfine interaction can further be suppressed applying external magnetic fields, which enables promisingly long spin lifetimes up to a millisecond

---

timescale [22, 26]. Apart from the spin, the noisy solid-state environment also affects the optical transition that provides the interface to the spin qubit. Fluctuating charge distributions in the QD environment lead to changes of the resonance energy over time [27]. In addition, nonradiative decay processes like Auger recombination can strongly decrease the efficiency of the optical interface [28]. Altogether, the dynamics guiding the decay of spin information and the degradation of the optical transition due to the solid-state environment are crucial in view of the implementation of a QD spin qubit and require special consideration.

A versatile tool to study spin dynamics and properties of the optical transition at the same time is the method spin noise spectroscopy (SNS). The principle of SNS is to map fluctuations of the spin in the ground state on a linearly polarized probe laser via Faraday rotation. Initially, this method was developed to study spin dynamics in atomic gases [29, 30]. The first SNS measurements on electron spins in bulk gallium arsenide have been demonstrated in 2005 [31]. Thereafter, SNS gained increasingly more attention in semiconductor spin physics as a convenient and powerful replacement of pump-probe techniques, which require optical excitation of spin-polarized carriers by an additional pump laser [32, 33]. In contrast, SNS does not need spin-polarized carriers to measure the spin decay times. Instead, the intrinsic spin dynamics are extracted from the spin fluctuations (spin noise, SN) in thermal equilibrium using a nonresonant probe laser. For sufficient detuning between probe-laser and optical transition this avoids increased spin relaxation as a result of optical excitation and yields the nearly undisturbed spin dynamics of the investigated system [34]. The spectroscopy of spin fluctuations proved to be a highly sensitive tool, leading recently to the first observation of the spin noise of a single hole spin localized in a QD [35]. These measurements revealed a long hole-spin relaxation time of 180  $\mu\text{s}$  in a small magnetic field of a few 10 mT for a well-detuned probe laser of very low light intensity. The spin relaxation time and the Faraday rotation signal depend strongly on the detuning between optical transition and probe laser, which can be exploited to gain information about the QD optical transition. The

SN investigation in Ref. [35] revealed a strong inhomogeneous broadening of the QD optical transition due to charge fluctuations in the environment. The spin dynamics determined from the equilibrium fluctuations of the system will only remain valid if external perturbations of the system are kept small. This relation follows from the fluctuation-dissipation theorem which builds the theoretical basis of the SNS method by linking the noise spectrum in thermal equilibrium to the linear response function of the system [36]. However, optical interrogation and manipulation of a spin qubit constitutes a strong external perturbation which drives the system far away from its equilibrium state. Under such strongly nonequilibrium conditions the physical properties of the system can change significantly and require a separate investigation.

In this thesis, SNS is applied to study the fluctuations of a single hole-spin in a QD beyond the bounds of thermal equilibrium conditions. For this purpose, the SNS probe laser is tuned into resonance with the optical transition such that it not only probes the spin information but also drives the optical transition at the same time. The resonant optical excitation creates a nonequilibrium situation very similar to the optical addressing of a spin qubit. The measured nonequilibrium spin fluctuations in combination with a theoretical analysis of the SN spectra beyond the fluctuation-dissipation theorem provide rich information about the physical properties of the optically driven spin system. While the equilibrium SN measurements contain only information about the spin dynamics in the ground state, the nonequilibrium fluctuations are additionally governed by the spin dynamics in the optically excited state. Moreover, an additional new noise contribution appears in the nonequilibrium SN spectra. The additional noise is found to originate from the temporary loss of the spin carrier residing in the QD as a result of Auger recombination. In general, this QD occupation noise in the nonequilibrium SN measurements provides information about the dynamics of charge exchange between the QD and its environment. Concerning the properties of the optical transition, laser-detuning dependent SN measurements on different QDs show that negligible inhomogeneous broadening of the optical transition can in principle



---

be achieved in the natural solid-state environment: for the case of a low QD density and a small number of charged defect states, a QD with a homogeneously broadened optical transition is observed which signifies negligible charge fluctuations in the QD environment.

The thesis is structured as follows: chapter 2 provides a general introduction to spin noise spectroscopy on single quantum dots. The first part of the chapter describes the optical properties and spin dynamics in self-assembled InAs QDs. The second part outlines the general concept of SNS to study spin dynamics. Chapter 3 provides information about the sample structure and the experimental setup. Furthermore, experimental aspects of photoluminescence and SN measurements on single QDs are discussed. Chapter 4 presents the nonequilibrium SN measurements under resonant optical driving with the corresponding theoretical analysis for two selected QDs. The two QDs show consistent but yet complementary results which can be attributed to distinct differences in their environment. SN measurements on the first QD reveal a homogeneously broadened optical transition and show that the spin fluctuations under resonant optical driving contain the spin dynamics of the ground and excited state simultaneously. Additionally, the quasi-resonant SN measurements show a new noise contribution, which is assigned to charge occupation noise of the QD as a result of Auger recombination. SN measurements on the second QD show a small inhomogeneous broadening of the optical transition, but confirm the excited state spin dynamics and Auger recombination dynamics observed previously. Moreover, the occupation noise of the second QD appears more complex, revealing the presence of a nearby ionized acceptor and a coupling of spin and charge dynamics in a magnetic field. Finally, chapter 5 provides a conclusion on the results and a brief outlook on further extensions of single QD SN measurements.



## 2. General Background

This chapter summarizes the basic knowledge related to spin noise spectroscopy (SNS) on single quantum dots (QDs) which is the main subject of this thesis. Section 2.1 introduces the studied semiconductor nanostructures: self-assembled InAs QDs. The section focusses in particular on their optical properties and on the spin dynamics of localized charge carriers in the QDs. Section 2.2 introduces the basic principle and the general theory of the optical method SNS which will be applied for the investigation of the QD spin dynamics.

### 2.1. InAs Quantum Dots

#### 2.1.1. Semiconductor Artificial Atoms

A semiconductor QD is a nm-sized heterostructure which confines charge carriers in all three dimensions. The small size of the dot leads to quantization effects in the electronic and optical properties of the semiconductor heterostructure which established the denotation as “quantum dot”.

In the last two decades many different QD fabrication techniques for various semiconductor materials have evolved, each with their own benefits for the resulting QD and its application [37–40]. A very popular type of QD in view of light-matter interaction and spin physics – and the type of QD studied in this thesis – are self-assembled QDs consisting of indium arsenide (InAs) or the alloy indium gallium arsenide ((InGa)As) embedded in a gallium arsenide (GaAs) matrix. These QDs are fabricated by molecular beam epitaxy (MBE) in the Stranski-Krastanov growth mode [41, 42] which

## 2. General Background

---

describes the epitaxial growth of semiconductor heterostructures with a significant lattice mismatch ( $\gtrsim 5\%$ ) [43]. **InAs** has a 7% larger lattice constant compared to **GaAs**. The epitaxial growth of a small amount of **InAs** on a **GaAs** substrate yields a thin **InAs** layer with a lattice constant adapted to the substrate. This layer is called the wetting layer. As a result of the lattice mismatch strain accumulates in the wetting layer until a critical thickness of about 1.7 monolayers [44] is reached. At this thickness the strain in the **InAs** layer relaxes partially by forming small randomly distributed islands [45]. Capping these islands again with **GaAs** results in a three-dimensional confinement potential for electrons and holes due to the energy band offsets in the **InAs/GaAs** heterostructure, so that the capped islands form the **InAs QDs**. Owing to the strain-driven random island formation on the substrate, the **QDs** are referred to as self-assembled **QDs**. The growth conditions and the amount of deposited Indium have to be controlled very carefully to obtain **InAs** islands which are free of crystal defects to ensure good optical properties [44, 45].

The **InAs QDs** are typically lens shaped [see Fig. 2.1(a)] with a diameter of about 20 nm and a height of about 5 nm, which corresponds to a number of approximately  $10^5$  atoms in the **QD** [26]. The **QD** dimensions are significantly smaller than the extent of the bulk wave function of electrons or holes, thereby yielding a quasi zero-dimensional object with quantization in every direction [44, 46]. As a result, the density of states is discrete and the **QD** exhibits a shell structure comparable to a single atom [45, 46]. Similar to atoms, the occupation of the shells is governed by Pauli's principle. The discrete levels in valence and conduction band have an energy separation on the order of 10 meV [26]. To maintain the quantization effects, the **QDs** are typically operated at liquid helium temperatures (4.2 K) which ensures that the thermal energy  $k_B T$  is smaller than the level spacing [44].

The energy of the levels, and thereby the optical emission energy, is determined by the size, shape, and composition of the **QDs** [45, 47]. This enables tailoring of the optical properties of the artificial atoms over a wide range by changing the growth conditions and the mate-

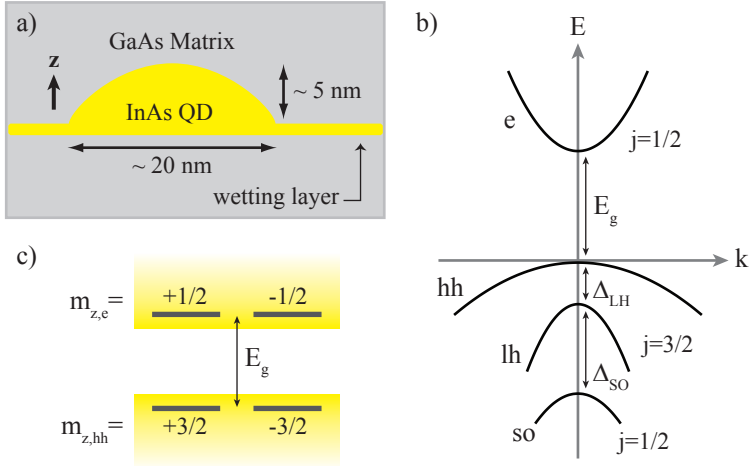


Figure 2.1.: (a) Typical shape and dimensions of a self-assembled **InAs QD** in a **GaAs** matrix. The  $z$  direction is defined as the growth direction of the heterostructure. (b) Schematic of the bulk **InAs** band structure in the presence of uniaxial strain along  $z$ . The valence band splits into heavy-hole band (hh), light-hole band (lh), and split-off band (so). (c) The s-shell of the **QD** consisting of the lowest confined **QD** states of electrons and holes at the band edge.

rial composition. In addition, the fabrication of the **QDs** in layers facilitates the incorporation in more complex structures enabling high-performance optoelectronic devices. On the other hand, the self-organized growth inevitably leads to slight variations of the size, material composition, and strain distribution, so that **QDs** – unlike atoms – are not identical within the same “species” [44, 45]. These variations manifest themselves as an inhomogeneous broadening of the quantities obtained in (optical) measurements on **QD** ensembles.

### 2.1.2. Optical Properties

The optical properties of the QDs are determined by the zero-dimensional density of states resulting in a shell structure with discrete optical transitions. The lowest energy states of electrons and holes at the band edges represent the QD s-shell. The optical measurements presented in this thesis are conducted in a way that only the optical transitions related to the QD s-shell are relevant. Higher energy states in the QD will be neglected in the following.<sup>1</sup>

Figure. 2.1(b) depicts the band structure of bulk InAs close to the band gap at the  $\Gamma$  point ( $k = 0$ ) in the presence of strain. This band structure applies as well for the strained InAs islands, although the quantization due to confinement is not yet taken into account here [44]. The corresponding Bloch wave function of electrons in the conduction band is  $s$ -type with an angular momentum quantum number of  $j = 1/2$ . In the valence band the hole Bloch wave function is  $p$ -type corresponding to 2 bands with  $j = 3/2$  and  $j = 1/2$ , respectively, which are split by the spin orbit interaction [ $\Delta_{\text{SO}}$  in Fig. 2.1(b)]. The  $j = 3/2$  band consists of 2 sub bands with the momentum projections  $m_z = \pm 3/2$  and  $m_z = \pm 1/2$ , denoted as the heavy-hole (hh) and the light-hole (lh) band, owing to their different curvatures associated with the effective particle masses. In the presence of uniaxial strain (along  $z$ ) the heavy- and light-hole bands are split by  $\Delta_{\text{LH}}$ . In InAs QDs the splittings  $\Delta_{\text{SO}}$  and  $\Delta_{\text{LH}}$  in the valence band are typically large enough to neglect lh and so-states for optical transitions [44]. As a result, the QD s-shell can be represented by a four-level system with the states  $m_z = \pm 1/2$  for electrons in the conduction band and the states  $m_z = \pm 3/2$  for holes in the valence band [see Fig. 2.1(c)]. Note that the QD band gap  $E_g$  is increased by almost 1 eV compared to the band gap of bulk InAs due to the confinement energy [46].

The optical selection rule  $\Delta j = \pm 1$  allows for optical transitions between the QD valence and conduction band states. The increased overlap of electron and hole wave functions due to the strong spatial

---

<sup>1</sup>Optical emission from higher QD shells becomes relevant for high-intensity nonresonant laser excitation.

confinement yields a particularly strong interaction with light [44, 46]. At the same time, the increased overlap leads to the formation of excitons which further define the QD optical properties.

### Neutral and Charged Excitons

The exciton is a hydrogen-like complex of an electron-hole pair, which is bound by Coulomb interaction. The energy of the exciton is reduced by the binding energy of the complex with respect to the single particle states in the QD. The binding energy due to Coulomb interaction is determined by the spatial overlap of electron and hole wave functions [44]:

$$E_B^{eh} = \frac{e^2}{4\pi\epsilon} \langle \psi_e \psi_h | \frac{1}{|\mathbf{r}_e - \mathbf{r}_h|} | \psi_e \psi_h \rangle, \quad (2.1)$$

where  $e$  is the elementary charge and  $\epsilon$  the dielectric constant. The binding energy is typically on the order of 10 meV in InAs QDs [48, 49] and the energy of the optical transition is reduced by  $E_B^{eh}$  compared to the energy difference of the single-particle states. In addition, exciton complexes consisting of multiple particles can exist in the QD. Especially in the case of a doped heterostructure, negatively or positively charged excitons can be observed. They consist of two electrons and one hole or two holes and one electron, respectively. The charged excitons are also referred to as trions due to their three constituents. A complex of two electrons and two holes is called a biexciton and corresponds to a completely filled QD s-shell. The binding energy of trions and biexciton is obtained by summing up all respective two-particle coulomb interaction terms [Eq. (2.1)] [44]. Note that the interaction terms of equally charged particles decrease the total binding energy due to their repulsion, they are subtracted. The total binding energy of trions and biexciton is typically higher than the exciton binding energy, so that their optical transitions lie energetically below the exciton transition in the emission spectrum. However, the respective wave function overlaps in the QD depend strongly on the QD size and morphology which can also lead to higher trion and biexciton transition energies

## 2. General Background

---

with respect to the exciton. In the following, the neutral exciton and the positively charged trion will be considered in more detail since they are the dominant complexes in the QDs investigated in this thesis due to a low  $p$ -type doping (see Sec. 3.1).

In addition to the Coulomb interaction, the neutral exciton is also subject to the electron-hole exchange interaction. This interaction corresponds to an effective coupling between electron spin  $S_e$  and hole angular momentum  $J_h$ , described by the exchange Hamiltonian: [50]

$$H_{exc} = \sum_{i=x,y,z} (a_i J_{h,i} S_{e,i} + b_i J_{h,i}^3 S_{e,i}). \quad (2.2)$$

The exciton eigenstates of the Hamiltonian depend on the symmetry of the QD. For QDs with rotational symmetry ( $b_x = b_y$ ) the states are characterized by the angular momentum projection  $M_z = S_{e,z} + J_{h,z}$ , yielding the 4 exciton states  $|\pm 1\rangle$  and  $|\pm 2\rangle$  [50]. The exchange interaction results in an energetic splitting between the states  $|\pm 1\rangle$  and  $|\pm 2\rangle$ . However, optical recombination of the states  $|\pm 2\rangle$  is forbidden since the angular momentum can not be conserved by the interaction with a single photon which has an angular momentum of  $\pm 1$ . For this reason, these states are called dark excitons and can be neglected for optical processes. The states  $|\pm 1\rangle$  conserve the angular momentum in an optical transition and are therefore called bright excitons. In the case of rotational symmetry, the bright exciton states are degenerate in energy. The self-assembled InAs QDs do generally not provide rotational symmetry, but are elongated in the  $xy$  plane resulting in  $b_x \neq b_y$ . In this case, the exchange interaction is anisotropic which leads to a mixing of the  $|\pm 1\rangle$  states [50]. The eigenstates of the anisotropic exchange Hamiltonian are given by the linear superpositions  $1/\sqrt{2}(|+1\rangle + |-1\rangle)$  and  $1/\sqrt{2}(|+1\rangle - |-1\rangle)$ . These states are split by the exchange energy  $\Delta E_{FS}$  [cf. Fig. 2.2(a)] which is usually referred to as fine-structure splitting following atomic physics. In InAs QDs this splitting is on the order of a few 10  $\mu\text{eV}$  to 100  $\mu\text{eV}$  [50, 51].

For the positively charged trion the situation is much simpler: The total angular momentum  $J_h$  of the holes is zero since the QD



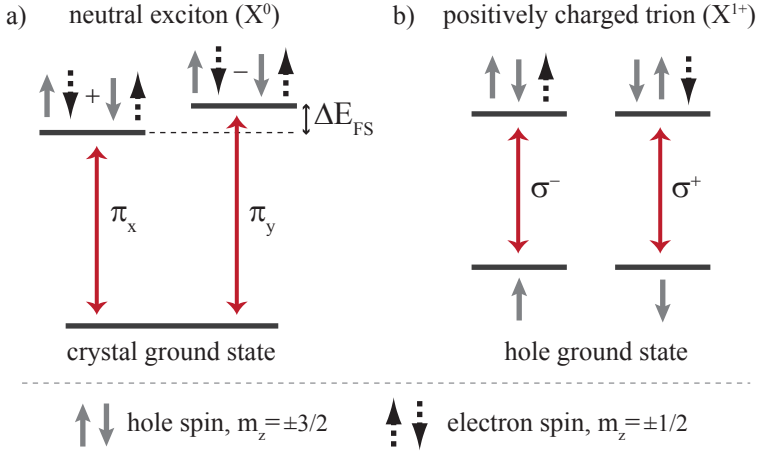


Figure 2.2.: (a) The superposition states of the neutral exciton (see text) and the respective linearly polarized optical transitions to the crystal ground state of the empty QD. The exciton states are split by the fine structure splitting  $\Delta E_{\text{FS}}$ . (b) The states of the positively charged trion and the respective circularly polarized optical transitions to the ground state with a single hole in the QD. Ground and trion states are spin degenerate if no magnetic field is present.

s-shell can only accommodate two holes with opposite spin due to Pauli's principle. As a result, the exchange interaction [Eq. (2.2)] vanishes and the trion states are given by the pure (unmixed) total angular momentum projections  $S_{e,z} = |\pm 1/2\rangle$  which are degenerate in energy [see Fig. 2.2(b)].<sup>2</sup>

<sup>2</sup>The same applies for the negatively charged trion with total electron spin  $S_e = 0$ , resulting in the trion states  $J_{h,z} = |\pm 3/2\rangle$ .

### Optical Selection Rules

The selection rules for the QD optical transitions follow from the total angular momentum of the exciton and trion states and are illustrated in Fig. 2.2. The mixed states of the exciton have a total angular momentum of zero as a result of the superposition of the angular-momentum eigenstates. An optical transition to the crystal ground state, i.e. the empty QD, can therefore only occur for photons with zero angular momentum which corresponds to linearly polarized light. The two exciton states exhibit the linearly cross-polarized optical transitions  $\pi_x$  and  $\pi_y$ , where the polarization axes  $x$  and  $y$  are oriented along the major and minor axis of the elliptic QD base [44]. The axes  $x$  and  $y$  often coincide with the crystal axes but their orientation can also deviate [51, 52].

Optical recombination of the positively charged trion results in a ground state with a single hole in the QD s-shell, which has an angular momentum of  $m_z = +3/2$  or  $m_z = -3/2$ . The trion states are defined by the electron momentum of  $m_z = +1/2$  or  $m_z = -1/2$ . The spin-conserving optical transitions (without change of the sign of  $m_z$ ) have an angular momentum difference of  $\pm 1$ , respectively. They can be mediated by circularly polarized photons, which provide this angular momentum. The diagonal, spin-flipping optical transitions are not allowed since they have an angular momentum difference of  $\pm 2$ . For the positively charged trion, these selection rules are very strict providing a spin-selective light-matter interaction with circularly polarized light at zero magnetic field [26, 53]. In contrast, the negatively charged trion (containing an unpaired hole spin) suffers from strain-induced mixing of heavy-hole and light-hole states, which leads to the occurrence of weak spin-flip transitions [16, 26].

The optical selection rules of the trion are altered in the presence of a magnetic field that is not parallel to the  $z$  direction. A magnetic field perpendicular to  $z$  results in linearly polarized diagonal and vertical transitions, while in a tilted magnetic field linearly and circularly polarized transitions can be observed [54, 55]. A magnetic field parallel to the growth direction maintains the selection

rules shown in Fig. 2.2(b), but induces a Zeeman splitting of the hole states and the trion states which results in different transition energies of the  $\sigma^+$  and  $\sigma^-$  polarized transitions. Note that the QD spin states experience an intrinsic nonzero magnetic field due to the interaction with the nuclear spins. This effective magnetic field is called the Overhauser field and will be discussed in more detail in Sec. 2.1.3. However, for the positively charged trion, the corresponding Zeeman splittings and the alteration of the optical selection rules is typically negligible [53].

The energies and polarizations of the QD exciton and trion transitions can conveniently be investigated by photoluminescence (PL) spectroscopy. Here, a PL excitation laser with a high photon energy creates electron-hole pairs in the GaAs matrix. The carriers relax into the QD, forming an exciton or trion which recombines radiatively. A polarization-resolved detection and spectral analysis of the PL light reveals the fine-structure splitting of the exciton (see Sec. 3.3) or the Zeeman splitting of the optical transitions in an external magnetic field [50].

### Auger Effect

The Auger effect, named after Pierre Auger [56], describes a non-radiative recombination process well-known from X-ray generation and electron spectroscopy on ionized atomic vapors [57]. An electron from the inner shell of an atom is removed, leaving a vacancy which is subsequently filled by an electron from the outer shell. The high energy difference of this transition can be emitted in the form of an X-ray photon, but it can also be transferred to another electron of the outer atomic shell which is thus ejected as a secondary electron of the ionization process [58]. The transition with the emission of another electron instead of an X-ray photon is referred to as an Auger or Auger-Meitner process.

In semiconductors, an Auger process occurs for three-particle complexes, e.g., for positively charged trions in a QD which is depicted schematically in Fig. 2.3(a). The recombination energy of the electron-hole pair is not emitted radiatively, but instead trans-

ferred to the second hole as kinetic energy. As a result, the hole is no longer confined to the QD and excited into the semiconductor continuum, which is the lower valence band in the case of a hole. The electron of a negatively charged trion is in turn excited into the conduction band by an Auger process. The excited particle relaxes usually very fast by multi-phonon emission which transfers the recombination energy into heat and makes Auger recombination a typical non-radiative process in semiconductors [57].

Non-radiative recombination channels often degrade the quality of an optical emitter. The Auger recombination in QDs leads to blinking of the optical transition which results in a reduced average quantum efficiency [59, 60]. Additionally, it causes a broadening of the optical linewidth [28]. The efficiency of Auger recombination in QDs depends strongly on the QD size [28, 61]. In small chemically-synthesized QDs with a diameter of about 4 nm the Auger recombination is very efficient, occurring with a rate of  $0.1 \text{ ps}^{-1}$  which leads to strong quenching of the radiative recombination [62]. The self-assembled InAs QDs are much larger with a typical base diameter of 10 to 20 nm. As a result, the Auger recombination rate is significantly reduced to about  $2 \text{ } \mu\text{s}^{-1}$  which is much slower than the radiative recombination rate [28]. Nevertheless, the resonance fluorescence measurements on a negatively charged trion in Ref. [28] revealed a strong impact of the Auger process for slow recharging dynamics of the self-assembled QD. Since the Auger recombination leaves the QD in the “empty” crystal ground state, the optical transition of the trion is completely quenched under resonant excitation (cf. Fig 2.2) until a new charge carrier is supplied to the QD by the solid-state environment. In samples with a charge reservoir, i.e., a highly-doped layer of GaAs close to the QD layer, the recharging time of the QD is precisely defined by the tunneling time which depends exponentially on the distance between doped layer and QDs. A tunneling time an order of magnitude longer than the Auger recombination time results in a quenching of the trion transition by 80 %, while for a tunneling time an order of magnitude shorter, the quenching is less than 5 % [28]. Hence, the detrimental effect of Auger recombination on the optical properties of the QD

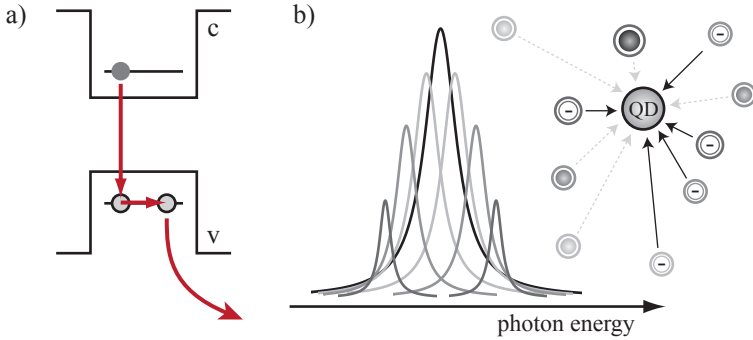


Figure 2.3.: (a) Auger recombination of a positively charged trion in the QD. The recombination energy of the electron-hole pair is transferred to the additional hole which is thus excited into the valence band continuum. (b) Schematic illustration of charge fluctuations in the QD environment. The redistribution of charges leads to shifts of the trion resonance energy resulting in an inhomogeneous broadening of the optical transition (see text).

trion can be compensated by a fast tunneling time between QDs and solid-state environment. On the other hand, however, fast tunneling times are not desirable in view of spin-photon interfaces since frequent tunnel processes degrade the intrinsically long spin coherence time in the QD [63]. In this case, a trade-off between optical efficiency and spin coherence has to be considered, so that Auger recombination is usually not negligible.

### Charge Fluctuations

Not only the charge dynamics between QD and environment, but also the charge dynamics which take place in the surroundings of the QD have an effect on the optical properties. Although MBE growth can produce very clean samples, there are typically still a

## 2. General Background

---

few trapping centers for free charges in the QD environment which can be related to, e.g., interface-fluctuations between different heterostructure layers [64] or to ionized doping centers, which provided resident charge carriers for the QDs [35]. Free charges which can be distributed between the localized trapping centers are provided in particular by non-resonant optical excitation [64], by the doping [35] or by Auger-recombination from QDs [65]. If the number of trapping centers is higher than the number of available charges, the distribution of charges changes on a slow timescale on the order of milliseconds to seconds [27, 66]. These dynamics are known as charge fluctuations or charge noise. The charge noise in the solid-state environment leads to a varying local electric field at the QD position which alters the energy of the optical transition via the quantum confined Stark effect: the electric field causes a bending of the band structure and thereby a displacement between electron and hole wave functions in the QD. This results in a shift of exciton and trion transitions to lower energies, proportional to the square of the electric field amplitude [44, 46]. Figure 2.3(b) depicts schematically how the redistribution of charges in the environment affects the QD optical transition over time. The electric field at the QD and the corresponding shift of the optical transition caused by a single charged defect depends strongly on the distance between defect and QD. In Ref. [64] it was shown that a trapped hole with a small distance of 30 nm to the QD leads to a huge shift of the optical resonance by 20  $\mu\text{eV}$ , which is more than an order of magnitude larger than the typical transition line width. Defects with a larger distance to the QD result in only small shifts of the resonance, depending on their charge status. In many cases, e.g., for ionized doping centers which are randomly distributed in the solid-state matrix, charge trapping centers with a larger distance to the QD are more probable than centers with just a few nm separation to the QD. For this reason, the overall charge fluctuations in the environment typically result with a higher probability in small energy shifts of the optical transition compared to large shifts [cf. Fig. 2.3(b)] [66, 67]. In general case, the charge dynamics in the QD environment are often very complex including a huge numbers of trapping centers and environment

charge configurations. As a result, the average optical transition is typically described by a Gaussian or Lorentzian distribution of resonance energies [35, 53]. Hence, in measurements which are averaged over timescales much longer than the charge fluctuations (i.e., seconds), an inhomogeneous broadening of the optical transition is observed which corresponds to the amplitude of charge fluctuations in the QD environment.

### 2.1.3. Spin Dynamics

An arbitrary spin state  $\psi_S$  can generally be decomposed into a superposition of its eigenstates  $|\uparrow\rangle$  (“spin up”) and  $|\downarrow\rangle$  (“spin down”) with respect to a given quantization axis: [44]

$$|\psi_S\rangle = \cos\frac{\theta}{2}|\uparrow\rangle + e^{i\phi}\sin\frac{\theta}{2}|\downarrow\rangle. \quad (2.3)$$

The parameters  $\theta$  and  $\phi$  can be interpreted as spherical coordinates, representing the spin state  $\psi_S$  as a point on a sphere which is known as the Bloch sphere (cf. Fig. 2.4). The time evolution of the spin state  $|\psi_S(t)\rangle = \exp\left[-\frac{i}{\hbar}\hat{H}t\right]|\psi\rangle$  is determined by the energy splitting  $\hbar\omega$  of the eigenstates. The equations of motion for the  $x$ ,  $y$ , and  $z$  projections of the spin state (2.3) in a magnetic field defining the quantization axis  $z$  have been formulated by Felix Bloch in 1946 [68] and are therefore known as Bloch equations. Their solution yields a constant polar angle  $\theta(t) = \theta_0$ , while the azimuthal angle  $\phi(t) = \omega_L t + \phi_0$  changes with the Larmor frequency  $\omega_L = g\mu_B B_z/\hbar$ : The spin precesses around the magnetic field direction leading to oscillating  $x$  and  $y$  spin projections over time, while the spin projection onto the  $z$  axis stays constant (cf. Fig. 2.4). A perfectly isolated spin would maintain this dynamics forever. However, interaction with the environment leads to a decay of the spin state after a certain time. To account for this, two decay times have been introduced phenomenologically to the Bloch equations. The longitudinal decay time  $T_1$  describes the decay of the initial spin projection along the magnetic field direction into the spin ground

## 2. General Background

---

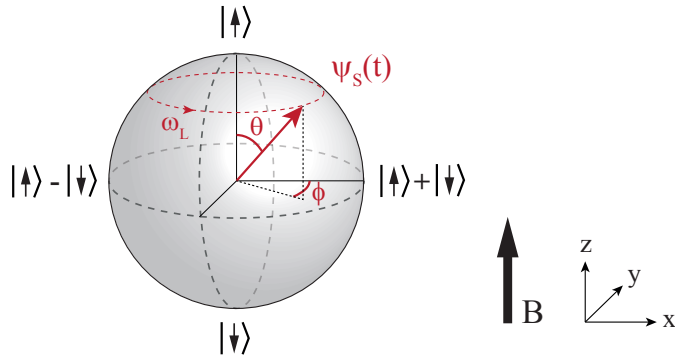


Figure 2.4.: The time evolution of an arbitrary spin state  $\psi_S(\theta, \phi)$  in a magnetic field along the  $z$  direction depicted on the Bloch sphere. The spin precesses around the magnetic field direction with the Larmor frequency  $\omega_L$ .

state. The transversal decay time  $T_2$  describes the loss of the phase information encoded in  $\phi$ , leading to unpredictable  $x$  and  $y$  projections [44]. The  $T_2$  time is therefore referred to as spin dephasing or decoherence time. The  $T_1$  time is connected with a loss of energy since the two eigenstates  $|\uparrow\rangle$  and  $|\downarrow\rangle$  are split by the Zeeman energy  $\Delta E = \hbar\omega_L = g\mu_B B_z$ . The  $T_1$  time is referred to as spin relaxation time. The relaxation of the spin state into one of the eigenstates along  $z$  also causes a loss of the in-plane coherence, so that the  $T_1$  time imposes an upper limit on the dephasing time:  $T_2 \leq 2T_1$  [69]. In a small magnetic field, the Zeeman splitting becomes negligible and  $T_1$  processes are no longer accompanied by energy dissipation, yielding  $T_1 \approx T_2$ . In addition to spin relaxation and dephasing, a spin decay due to an inhomogeneous environment, e.g., fluctuations of the direction and magnitude of the magnetic field, is usually considered separately since it leads to dephasing which acts on all three spin projections. The corresponding decay time is referred to



as inhomogeneous spin dephasing time  $T_2^*$  which is typically shorter than the  $T_2$  time [70].

In semiconductors, there exist several processes which cause efficient spin relaxation or dephasing. The four dominant mechanisms for electrons in bulk semiconductors are the Dyakonov-Perel mechanism, the Elliott-Yafet mechanism, the Bir-Aronov-Pikus mechanism, and the hyperfine interaction [70]. In the Dyakonov-Perel mechanism spin-orbit coupling in the absence of inversion symmetry yields a momentum dependent effective magnetic field for the electrons or holes [71]. Scattering into other momentum states results in a fluctuating effective field, which leads to spin dephasing. The Elliott-Yafet mechanism relates to a spin-orbit coupling induced mixing of the spin states, which encourages spin-flip processes by impurity scattering [72, 73]. The Bir-Aronov-Pikus mechanism is most relevant for electrons in the presence of holes (highly  $p$ -doped samples or optically created electron-hole pairs) and mediates spin-flips via the electron-hole exchange interaction [74]. At very low doping densities with quasi-localized electrons the hyperfine interaction dominates the spin dephasing as a result of the interaction with the fluctuating nuclear spin bath [75]. The hole-spin relaxation in bulk semiconductors is typically governed by the strong mixing of the valance band states (Elliott-Yafet), yielding a fast spin relaxation compared to electrons [70]. However, for localized carriers in quantum dots with  $\langle k_{e,h} \rangle = 0$ , spin-state mixing is reduced by the confinement-induced splitting of the bands, and the interaction with phonons is strongly suppressed at low temperatures [26, 76]. As a result, the hyperfine interaction with the nuclear spins dominates the dynamics of the resident electron or hole spin in a QD.

### Hyperfine Interaction

A typical self-assembled InAs QD comprises a number of approximately  $N = 10^5$  atoms with each having a nuclear spin. The hyperfine interaction (HFI) describes the magnetic interaction between the confined particle with spin  $\mathbf{S}$  and angular momentum  $\mathbf{L}$  and all nuclear spins  $\mathbf{I}_j$ , which is also known as the central spin problem.

## 2. General Background

---

In general, the Hamiltonian of the hyperfine interaction is given by: [77]

$$H_{hf} = \hbar g \mu_B \sum_{j=1}^N \gamma_j \mu_B \mathbf{I}_j \left[ \frac{8\pi}{3} \mathbf{S} \delta(\mathbf{r}_j) + \frac{\mathbf{L} - \mathbf{S}}{r_j^3} + 3 \frac{\mathbf{r}_j (\mathbf{S} \cdot \mathbf{r}_j)}{r_j^5} \right]. \quad (2.4)$$

Here, the sum runs over all nuclei in the QD,  $g$  and  $\gamma_j$  are the gyromagnetic factors of particle and nuclei, respectively,  $\mu_B$  is Bohr's magneton,  $\mathbf{r}_j = \mathbf{r} - \mathbf{R}_j$  defines the relative position of the spin  $\mathbf{S}$  with respect to the  $j$ th nuclei, and  $r_j$  corresponds to their distance. The first term in Eq. (2.4) with the delta function  $\delta(\mathbf{r}_j)$  describes the Fermi contact interaction, whereas the second and third term correspond to the dipole-dipole coupling. The Fermi contact interaction dominates the HFI for electron spins as a result of their  $s$ -type wave function. The  $s$ -type wave function has a large probability density at the lattice sites  $\mathbf{R}_j$  of the nuclei (cf. Fig. 2.5) resulting in a strong coupling of electron and nuclear spins. In contrast, the  $p$ -type heavy-hole wave function is dropping to zero at the lattice sites which suppresses the Fermi contact interaction. Therefore, the HFI of the heavy-hole spins is given by the much weaker dipole-dipole interaction. Apart from the coupling strength, this yields another striking difference for the HFI of electrons and holes: the magnetic dipole moment of the heavy-hole is oriented solely along the  $z$  direction, such that the HFI due to  $x$  and  $y$  components of the nuclear spins is cancelled and only a  $z$  component (Ising-form) remains [26]. However, the heavy-hole states in the QD are not absolutely pure, but have a small admixture of light-hole states. Typically, this yields a small HFI coupling in  $x$  and  $y$  direction, but still the heavy-hole HFI stays highly anisotropic [78]. In contrast, the Fermi contact interaction of the electron spin is isotropic.

Although, the physical origin of the HFI of electrons and holes is different, the simplified representation of their HFI Hamiltonian appears qualitatively very similar: [22, 78]

$$H_{hf}^\sigma = v_0 \sum_{j=1}^N |\psi^\sigma(\mathbf{R}_j)|^2 (A_x^{\sigma,j} I_x^j S_x + A_y^{\sigma,j} I_y^j S_y + A_z^{\sigma,j} I_z^j S_z), \quad (2.5)$$

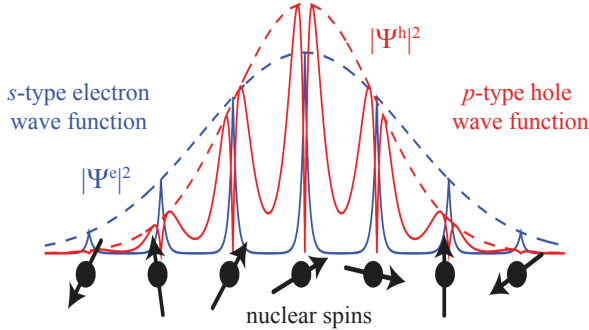


Figure 2.5.: Schematic of electron and hole wave functions in the QD, illustrating their difference in hyperfine interaction with the nuclear spins (adopted from [78]). The  $s$ -type electron wave function has maxima at the nuclei which yields a strong hyperfine interaction. The  $p$ -type hole wave function drops to zero at the lattice sites, resulting in a weak coupling to the nuclear spins. The dashed lines represent the envelope of electron and hole wave functions in the QD with the maximum at the QD center.

with  $\sigma = e, h$  denoting the electron or hole, respectively. Here,  $v_0$  is the unit cell volume,  $\psi^{e,h}(\mathbf{R}_j)$  is the envelope of the wave function at the  $j$ th nucleus (cf. Fig. 2.5), and  $A^j$  is the isotope specific coupling coefficient with  $A_x^e = A_y^e = A_z^e$  and  $0.1 \cdot A_{x,y,z}^e \approx A_z^h \gg A_{x,y}^h$ , where the coefficients  $A_{x,y}^h$  are determined by the light-hole admixture [25]. The expectation value of the Hamiltonian (2.5) taken over the nuclear ensemble of  $N$  atoms yields an effective nuclear magnetic field: [23, 25]

$$\mathbf{B}_N^\sigma = \frac{v_0}{\mu_B g_\sigma} \sum_{j=1}^N \mathbf{A}^{\sigma,j} |\psi^\sigma(\mathbf{R}_j)|^2 \mathbf{I}^j. \quad (2.6)$$

This effective magnetic field is called the Overhauser field. The Overhauser field is not constant, but varies in magnitude and di-

## 2. General Background

---

rection over time due to thermal fluctuations of the nuclear spins  $\mathbf{I}^j$ , known as nuclear spin noise [27]. The stochastic fluctuations are described by a Gaussian probability distribution with a width  $\Delta_B^\sigma$  [23]. The precession of the electron or hole spin in the fluctuating Overhauser field results in an inhomogeneous spin dephasing on a time scale: [23, 25]

$$T_2^* = T_\Delta^\sigma = \frac{\hbar}{\mu_B g_\sigma \Delta_B^\sigma}. \quad (2.7)$$

The magnitude of  $\Delta_B^\sigma$  scales with the number of nuclei as  $1/\sqrt{N}$  and is proportional to the coupling coefficients  $A_{x,y,z}^j$ . The isotropic hyperfine interaction of the electron corresponds to a magnetic field fluctuation  $\Delta_B^e$  of about 10 to 30 mT in InAs QDs [22], which results in fast electron spin dephasing on the order of  $T_\Delta^e \approx 500$  ps [25, 79]. The smaller coupling coefficients for the HFI of the hole spin yield a weak in-plane ( $x, y$ )  $\Delta_B^h$  of about 5 mT [25, 80] and a dephasing time  $T_\Delta^h \approx 14$  ns [25], which is more than an order of magnitude longer compared to the electron but depends in general on the heavy-hole and light-hole mixing in the individual QD.

### Spin Dynamics in an External Magnetic Field

The application of a magnetic field in  $z$  direction results in a carrier spin precession around the direction of the total magnetic field  $\mathbf{B} = \mathbf{B}_z + \mathbf{B}_N$ . If  $B_z \gg \Delta_B$ , the fluctuations of the Overhauser field perpendicular to  $z$  can be considered as a small perturbation of the total magnetic field direction. As a result, the dominant external field  $\mathbf{B}_z$  “stabilizes” the carrier-spin projection along  $z$  [22]. Strictly speaking, the Zeeman splitting of the carrier spin in the external magnetic field has to be larger than the inhomogeneous broadening of the spin levels resulting from the interaction with the fluctuating nuclear spins [23]. In this case, the spin decay due to the hyperfine interaction (Eq. (2.7)) is efficiently suppressed along the direction of the external magnetic field. For the electron spin this requires a magnetic field on the order of  $B_z = 100$  mT yielding a  $T_1$  time about an order of magnitude longer compared to  $T_\Delta^e$  at  $B_z = 0$  [79].

For the hole spin already a few 10 mT are sufficient to observe prolonged spin relaxation times as long as 180  $\mu\text{s}$  [35]. However, the uni-directional external field can not shield the  $x$  and  $y$  component of the spin from the hyperfine interaction and these components still exhibit a fast dephasing in the total magnetic field [23]. Note, that for a pure heavy-hole spin with an Ising-like hyperfine coupling restricted to the  $z$  component, the hyperfine interaction can be completely switched off by applying a strong magnetic field in the  $x, y$  plane [78, 81].

For strong external magnetic fields along  $z$ , the suppression of the spin relaxation by hyperfine interaction yields long electron and hole  $T_1$  times, which can reach values of milliseconds up to a second in a magnetic field of a few Tesla [53, 63, 82]. In higher magnetic fields, the  $T_1$  time decreases again following a power-law dependence on the magnetic field ( $\sim B_z^{-5}$ ) [26, 82]. The strong magnetic field dependence suggests that, beyond hyperfine interaction, the spin relaxation is governed by phonon-assisted spin-flip processes between the Zeeman sublevels which are mediated by spin-orbit interaction [82–84]. The phonon-related spin relaxation becomes especially important at higher temperatures as it exhibits a linear temperature dependence [85, 86]. In the case of hole-spins, a deviation from the one-phonon mediated spin relaxation can be observed in low magnetic fields ( $B < 3$  T) [53, 85]. A theoretical analysis suggests that the hole-spin relaxation at low magnetic fields is determined by two-phonon processes. The two-phonon processes depend only weakly on the magnetic field and limit the hole spin relaxation time to milliseconds above 2 K [26, 86].

Regarding the spin dephasing time, a route to circumvent the inhomogeneous dephasing by the fluctuating Overhauser field is Hahn-echo decoupling of the carrier spin on timescales faster than the nuclear spin fluctuations [87]. In this technique, an optical  $\pi$ -pulse reverses the direction of spin dephasing which protects the spin coherence from slow changes of the Overhauser field. However, Overhauser field dynamics faster than the pulse-sequence for decoupling and read-out can not be filtered and limit the electron-spin  $T_2$  time to a few microseconds in a transverse magnetic field of a few

Tesla [87, 88]. Theoretical modeling and experiments suggest that the fast Overhauser field dynamics result from quadrupolar coupling of the nuclear spins to inhomogeneous electric field gradients which are induced by the strain in the self-assembled QDs [88, 89]. Since hole spins exhibit a weaker interaction with the nuclear spins, their  $T_2$  time should be less affected by the nuclear quadrupole interaction. However, in contrast to electrons, the coherence of the hole spin is sensitive to charge noise in the environment (cf. Sec. 2.1.2) due to an electric field dependence of the hole g-factor [90, 91]. For this reason, hole spin dephasing times in the microsecond regime are only possible in very clean samples [78].

## 2.2. Spin Noise Spectroscopy

Spin noise (SN) refers to the stochastic temporal fluctuations of the entity spin in (quasi) thermodynamic equilibrium. Analysis of these fluctuations provides insight into the intrinsic spin dynamics of the studied system according to the fluctuation-dissipation theorem [92]. Spin noise spectroscopy (SNS) is an optical technique which allows to measure the fluctuations of the spin projection in the direction of laser propagation. SNS was introduced in 1981 by Alexandrov and Zapasskii who demonstrated the technique on sodium vapor atoms [29]. In 2005, Oestreich et al. transferred the method to semiconductors and demonstrated the first spin noise measurements on donor electrons in GaAs [31]. Thereafter, SNS evolved into a versatile tool to study the spin dynamics in various semiconductors and semiconductor nanostructures [32, 33, 93].

Figure 2.6 illustrates the basic principle of SNS on a single spin in a QD. A linearly polarized probe laser interacts with the QD. The photon energy of the laser is tuned well below the resonance of the optical transition such that no trion excitation occurs and the laser light is transmitted. However, the polarization plane of the light is sensitive to the projection of the ground-state spin onto the propagation axis via the Faraday effect. As a result, the transmitted laser light shows a small rotation of the polarization plane

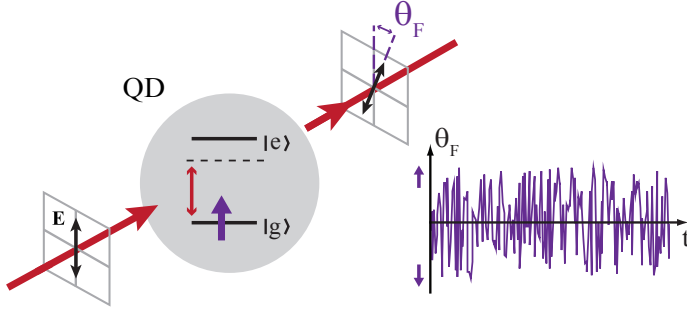


Figure 2.6.: Principle of spin noise spectroscopy. Thermal fluctuations of the spin in the QD ground state are mapped onto the polarization of a nonresonant probe laser via Faraday rotation.

by an angle  $\theta_F$  which depends on the spin state averaged over the corresponding measurement time bin. Thus, the spin fluctuations manifest themselves as noise of the Faraday rotation angle. The Faraday rotation noise is analyzed by a time-resolved polarimetric measurement of the transmitted beam. A spectral analysis of the average noise signal reveals the dynamics of the spin in the QD ground state.

In the following, section 2.2.1 provides further details on spin fluctuations and their connection to spin dynamics. Section 2.2.2 introduces the principle of Faraday and Kerr rotation. Details about the experimental realization of SNS are provided in section 3.4.

### 2.2.1. Spin Fluctuations and Noise Spectrum

Stochastic thermal fluctuations are inherently present in any physical system and lead to a statistical distribution in repeated measurements of a specific physical quantity. The statistical variation of the mean value is referred to as noise, which is also observed in measure-

## 2. General Background

---

ments of a carrier's spin state. In thermal equilibrium,<sup>3</sup> it is equally probable to detect the QD spin in one of the two ground states with pseudo-spin projections  $S_z = \pm 1/2$ . As a result, a measurement on an infinite ensemble of identical spins, or equivalently, an infinite number of repeated measurements on a single spin yields an average spin projection of  $\langle S_z \rangle = 0$ . However, a finite number of  $n$  measurements leads to incomplete statistical cancellation with an average spin projection  $\langle S_z \rangle_n \neq 0$  [33]. Repeated measurements yield a statistical distribution of  $\langle S_z \rangle_n$  around zero which is characterized by the standard deviation  $\sigma_{\text{SN}}$  related to the spin noise. The spin noise can be optimally analyzed by considering the spectral distribution of the noise power ( $\propto \sigma_{\text{SN}}^2$ ). The noise power spectral density, i.e., the noise power as a function of frequency, is obtained as the absolute square of the Fourier transform of a finite time trace of the fluctuating average spin projection. Statistical physics provides a mathematical theorem which links the power spectral density of the fluctuations in thermal equilibrium to the linear response function of the system under a small external perturbation. This theorem is known as the fluctuation-dissipation theorem [92]. Applied to the case of single spins, the perturbation can be considered as a preparation of the spin in one of its eigenstates  $S_z = \pm 1/2$ . In response, the spin will decay to its time-averaged equilibrium value according to the spin dynamics introduced in Sec. 2.1.3, i.e., on the characteristic timescales  $T_1$  and  $T_2$  which are determined by the interaction of the spin with its environment. According to the fluctuation-dissipation theorem, the same time scales govern the spin fluctuations in thermal equilibrium and the spin dynamics can be extracted from the spin noise power spectral density without the need of performing any spin manipulations.

The noise power spectral density and the fluctuation dynamics in the time domain are connected via the autocorrelation function  $C(\tau)$  of the spin fluctuations. The Wiener-Chintchin theorem [94, 95] states that the power spectral density of the spin noise is repre-

---

<sup>3</sup>This allows the presence of small external magnetic fields, provided that  $g\mu_B B \ll k_B T$ .



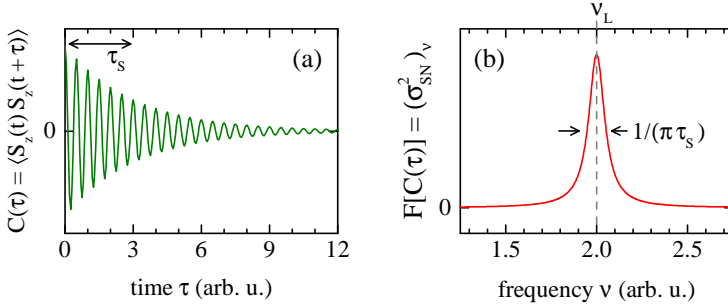


Figure 2.7.: Auto correlation function (a) and power spectral density (b) of a fluctuating spin which precesses in a transverse magnetic field with the Larmor frequency  $\nu_L$ . A stochastic spin projection  $S_z$  at  $\tau = 0$  decays on a time scale  $\tau_s$ . The noise power spectral density is linked to the autocorrelation by Fourier transformation.

sented by the Fourier transform of its autocorrelation function, i.e.  $F[C(\tau)] = \sigma_{SN}^2(\nu)$  [36]. This can be illustrated as follows: a stochastic instantaneous spin polarization  $S_z(t) \neq 0$  at an arbitrary time  $t$  will decay on a characteristic time scale  $\tau_s$  (as stated above). The decay of the spin polarization can be described by an exponential function in the case of a homogeneous dephasing process. If a transverse magnetic field is applied, the “noisy amplitude” of the spin projection  $S_z$  will be modulated over time. The autocorrelation function of  $S_z$  is then given by: [33, 96]

$$C(\tau) = \langle S_z(t) S_z(t + \tau) \rangle \propto \cos(2\pi\nu_L\tau) e^{-\tau/\tau_s}, \quad (2.8)$$

where  $\nu_L$  is the Larmor frequency of the spin. The autocorrelation function shows a damped oscillation over time which is plotted in Fig. 2.7(a). Fourier transformation of Eq. (2.8) yields a Lorentzian type power spectral density, which is centered at the Larmor frequency [cf. Fig. 2.7(b)]. The FWHM of the Lorentzian is inverse proportional to the spin life time  $\tau_s$ . Hence, the width of the power

spectral density yields the information about the characteristic spin decay times. The Lorentzian noise spectrum is solely linked to an exponential decay of the spin. Depending on the mechanism which determines the spin decay, the spectrum can have a different shape. For example, inhomogeneous processes which lead to spin dephasing typically result in a Gaussian noise spectrum and also more complex spectral shapes are possible if different dephasing mechanisms contribute to the spin decay [33, 75, 97, 98].

The general concept of spin noise spectroscopy is to determine the intrinsic spin dynamics in thermal equilibrium by omitting any perturbation of the system. This has the advantage that the measured spin dynamics will not be enhanced by additional dephasing effects caused by the perturbation itself, like the creation of optically excited carriers [34]. In order to maintain the thermal equilibrium, it is essential that the SN probe laser is sufficiently detuned from the optical transition since light absorption drives the system out of equilibrium. However, in view of applications it might not be feasible to provide equilibrium conditions since the spin has to be initialized and read out. Spin fluctuations are also present under nonequilibrium conditions, e.g., under optical excitation or in oscillating magnetic fields, and thereby provide rich information about the nonequilibrium spin dynamics [99, 100]. Hence, spin noise spectroscopy is not necessarily restricted to the “non-perturbative” regime, but can also be applied when the probe-laser is quasi-resonant to the optical transition and excites trion states. However, under nonequilibrium conditions the fluctuation-dissipation theorem is not longer valid and thus a non-generalized theoretical treatment is required to link the SN spectrum to the nonequilibrium dynamics in the system [101]. A theoretical model which derives the nonequilibrium SN spectrum in the presence of strong optical driving by the probe laser will be presented in chapter 4.

### 2.2.2. Faraday and Kerr Rotation

Materials which possess optical transitions with spin-selective optical selection rules offer the possibility to read out the spin infor-

mation optically. Spin-dependent selection rules are found in most III-V and II-VI semiconductor structures which promotes the optical investigation of their spin dynamics [34]. In particular, the optical transition of the positively charged trion in the InAs QDs (cf. Fig. 2.2) provides a 1:1-relation between spin projection and light polarization which yields an optimal sensitivity of SN measurements. In comparison, the selection-rules in bulk GaAs link the light polarization only with a 3:1-probability to the electron spin state [96], but still enable SN measurements.

The impact of the (average) population of spin-up and spin-down states on the electromagnetic field of a laser is fully described by the dielectric response function. The complex dielectric function corresponding to a single optical transition with the resonance frequency  $\omega_0$  has the following form as a function of laser frequency  $\omega$ : [43]

$$\epsilon_{\pm}(\omega) = 1 + \frac{f_{\pm}}{\omega_0^2 - \omega^2 - i\omega\Gamma}. \quad (2.9)$$

Here,  $\Gamma$  is the linewidth of the optical transition. The coupling strength  $f_{\pm}$  for  $\sigma^+$  and  $\sigma^-$  polarized light is proportional to the transition matrix element and depends on the population of spin-up and spin-down states. In the case of a QD hole-spin in the spin-down (spin-up) state an optical transition with  $\sigma^-$  ( $\sigma^+$ ) polarized light is not possible so that  $f_-$  ( $f_+$ ) vanishes.

The square root of the dielectric function (2.9) yields the complex refractive index:<sup>4</sup>

$$\tilde{n}_{\pm}(\omega) = n_{\pm}(\omega) - i\alpha_{\pm}(\omega), \quad (2.10)$$

where the real part corresponds to the refractive index  $n$  and the imaginary part describes the light absorption  $\alpha$  for laser light with a frequency  $\omega$ . Figure 2.8 shows the absorption and the refractive index for  $\sigma^+$  and  $\sigma^-$  polarized light in the vicinity of the optical transition as a function of the laser detuning  $\Delta = \omega - \omega_0$ . An imbalance in the occupation of spin-up and spin-down states leads

---

<sup>4</sup>In general case,  $\tilde{n} = \sqrt{\mu\epsilon}$ , with  $\mu$  being the magnetic permeability, but in non-ferromagnetic materials  $\mu = 1$  and  $\tilde{n} = \sqrt{\epsilon}$  [102].

## 2. General Background

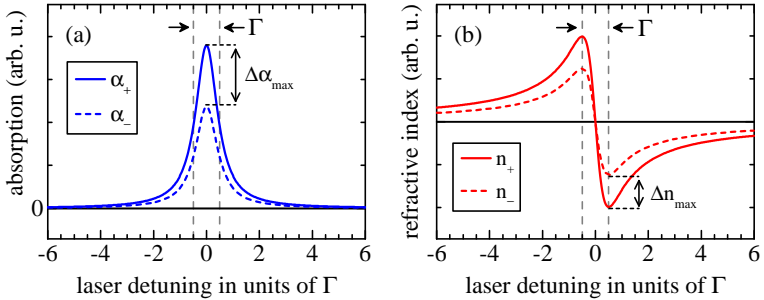


Figure 2.8.: Absorption (a) and refractive index (b) as a function of the laser detuning  $\Delta$  for an optical transition with linewidth  $\Gamma$ . An imbalance in the population of spin-up and spin-down states results in unequal absorption and dispersion of  $\sigma^+$  and  $\sigma^-$  polarized light.

to different amplitudes of  $\alpha(\Delta)$  and  $n(\Delta)$  for the different circular polarizations. SNS uses linearly polarized laser light which is a superposition of  $\sigma^+$  and  $\sigma^-$  polarized light:

$$E_x(z, t) = 1/\sqrt{2} [E_{\sigma^+}(z, t) + E_{\sigma^-}(z, t)], \quad (2.11)$$

for light polarized along the  $x$  axis and propagating along  $z$ . Unequal absorption of the  $\sigma^+$  and  $\sigma^-$  parts transforms the initial linear polarization to an elliptic polarization. This effect is therefore known as induced ellipticity. The absorption difference  $\Delta\alpha(\Delta)$  between  $\sigma^+$  and  $\sigma^-$  polarized light is maximal at zero detuning, i.e., for  $\omega = \omega_0$  linearly polarized light is most sensitive to ellipticity, which reveals an unequal spin population based on light absorption. The ellipticity sensitivity scales with  $\Delta\alpha(\Delta)$  and follows a Lorentzian detuning-dependence (proportional to  $\alpha_{\pm}(\Delta)$ ) if inhomogeneous broadening of the optical transition can be neglected [96].

The refractive index is an odd function of the laser detuning with maximum/minimum values at  $\Delta = \pm\Gamma/2$ . A refractive index dif-

ference  $\Delta n$  between  $\sigma^+$  and  $\sigma^-$  polarized light does not affect the amplitudes of  $E_{\sigma^+}$  and  $E_{\sigma^-}$ , but leads to a phase difference between the circularly polarized field components. As a result, the initial linear polarization along  $x$  is rotated in the  $x$ - $y$  plane. The rotation of the polarization axis of linearly polarized light due to a circular refractive index difference is known as the Faraday effect. The Faraday rotation angle is proportional to  $\Delta n$  and scales with the propagation length  $l$  through the birefringent medium: [96]

$$\theta_F = \pi \frac{l}{\lambda} \Delta n, \quad (2.12)$$

with  $\lambda$  being the laser wavelength. SNS typically measures the Faraday rotation angle, which is proportional to the average spin population via  $\Delta n$ . The dependence of  $\Delta n$  on the laser detuning is again proportional to  $n_{\pm}(\Delta)$ . As a result, Faraday rotation and thereby SNS is most sensitive for a laser detuning equal to the half linewidth of the optical transition, but is insensitive for  $\omega = \omega_0$  where  $\Delta n$  vanishes. Additionally, Fig. 2.8 shows that  $n_{\pm}$  and  $\Delta n$  decrease much slower as a function of laser detuning compared to the absorption  $\alpha_{\pm}$ . This fact is essential for SN measurements in thermal equilibrium (cf. Sec. 2.2.1) since light absorption becomes negligible for sufficiently large laser detuning, while the refractive index difference is still finite and enables the extraction of the spin information.

Note that the description of  $\alpha_{\pm}$  and  $n_{\pm}$  as presented in Figure 2.8 is only valid in the case of negligible Zeeman splitting between the spin states. A significant Zeeman splitting results in different resonance frequencies  $\omega_{0,+}$  and  $\omega_{0,-}$ . As a result, the circular components  $n_+$  and  $n_-$  ( $\alpha_+$  and  $\alpha_-$ ) are shifted with respect to the laser detuning and  $\Delta n$  ( $\Delta\alpha$ ) can exhibit a very different dependence on the laser detuning, which leads to Faraday rotation (ellipticity) even for equal spin state populations. For a fixed laser detuning the (constant) Faraday rotation due to the Zeeman splitting is proportional to the applied magnetic field. However, the SN measurements focus on the temporal changes of the amplitude of  $\Delta n$  which reveal variations in the average spin population over time caused by the

## 2. General Background

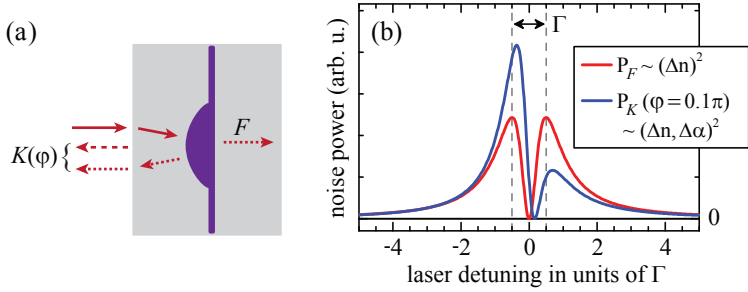


Figure 2.9.: (a) Schematic illustration of Faraday and Kerr rotation signal. The Faraday signal is simply given by the transmitted beam. The light reflected from the QD interferes with the light reflected from the sample surface. The phase  $\varphi$  between the two beams determines the Kerr signal. (b) Noise power of Faraday and Kerr rotation signal as a function of the laser detuning for an optical transition with linewidth  $\Gamma$ .

spin fluctuations. The spin fluctuations translate into noise of the Faraday rotation angle proportional to the noise in  $\Delta n$ . Hence, the noise power of the Faraday rotation angle is proportional to the spin noise power and scales with the laser detuning according to the square of  $\Delta n$ :

$$\sigma_{\text{SN}}^2 \propto \sigma_{\theta_F}^2 \propto [\Delta n(\Delta)]^2. \quad (2.13)$$

The noise power of the Faraday rotation angle due to the fluctuating spin population is shown by the red line in Fig. 2.9(b). The noise power is maximal for laser detunings equal to the half linewidth of the transition,  $\Delta = \Gamma/2$ , and vanishes at  $\Delta = 0$ .

The Faraday rotation  $\mathcal{F}$  of the linearly polarized SNS probe beam can be conveniently measured in transmission. The transmitted beam is split into two linearly polarized components which are aligned along the axes rotated by  $\pm 45^\circ$  with respect to the initial polarization axis of the probe beam. The intensity difference of the two

components is then proportional to the Faraday rotation angle<sup>5</sup> and the refractive index difference  $\Delta n$  of the circular components of the probe beam. In case of small probe laser detuning, the Faraday rotation is accompanied by unequal absorption  $\Delta\alpha$  of the circular components, leading to ellipticity  $\mathcal{E}$  of the beam (cf. Fig. 2.8). However, the detection scheme described above is only sensitive to changes of the relative phase between  $\sigma^+$  and  $\sigma^-$  components of the probe beam, but is insensitive to changes of their amplitude. For this reason, only Faraday rotation is measured. A measurement of the ellipticity can be performed by changing the measurement basis. This is realized using a quarter wave plate before projecting the transmitted probe beam onto the two orthogonal  $\pm 45^\circ$  axes. The introduced phase shift of  $\pi/2$  makes the intensity difference sensitive to amplitude changes of the  $\sigma^+$  and  $\sigma^-$  polarized components, while the Faraday rotation signal is suppressed.

Faraday rotation is not only present in the transmitted probe beam, but can also be measured in the reflected probe light which is known as a Kerr rotation measurement. Similar to the detection scheme in transmission, the reflected probe light from the sample is split into the orthogonal linearly polarized components along  $\pm 45^\circ$  and their intensity difference is measured. Hence, in principle the Kerr rotation measurement can be considered equivalent to Faraday rotation being sensitive to the refractive index difference in the structure. However, for complex sample structures, e.g., QDs embedded in a solid-state matrix, the Kerr rotation signal  $\mathcal{K}$  can be very different from the Faraday rotation signal. Figure 2.9(a) depicts schematically the probe beam propagation through the QD sample. At the sample surface a fraction of the probe light is reflected. The transmitted part interacts with the QD collecting a Faraday and ellipticity signal according to the QD spin state. Part of the information-carrying probe light is transmitted, yielding the Faraday signal  $\mathcal{F}$  as described above. The reflected part of the information-carrying probe beam interferes with the probe light reflected on the sample surface and the resulting sum of the electro-

---

<sup>5</sup>The Faraday rotation angle is typically very small, so that  $\sin(\theta_F) \approx \theta_F$ .

## 2. General Background

---

magnetic fields is analyzed in a Kerr rotation measurement. The interference field depends on the relative phase  $\varphi$  between the light reflected from the surface and the light which interacted with the QDs. As a result, the measured intensity difference along  $\pm 45^\circ$  is not longer exclusively sensitive to Faraday rotation, but can be partially sensitive to the ellipticity of the probe beam, depending on the phase difference  $\varphi$ : [103]

$$\begin{aligned}\mathcal{K}(\varphi) &= \cos(\varphi) \mathcal{F} + \sin(\varphi) \mathcal{E} \\ &\propto \cos(\varphi) \Delta n + \sin(\varphi) \Delta\alpha.\end{aligned}\tag{2.14}$$

Eq. (2.14) shows that the Kerr rotation signal  $\mathcal{K}$  of the QD is in general case a superposition of the ellipticity and Faraday signal. Their relative strength in the Kerr rotation signal is determined by the interference with the probe light reflected from the sample surface. For interference with a phase difference of  $\varphi = n \cdot \pi$  ( $n = 0, 1, \dots$ ), the Kerr rotation measurement shows only the Faraday rotation, consistent with the measurement in transmission. In contrast, a phase difference of  $\varphi = n \cdot \pi/2$  results in exclusive detection of the ellipticity. Any phase difference in between leads to a mixed Kerr rotation signal. Since  $\Delta\alpha$  and  $\Delta n$  are both proportional to the spin state population difference, the Kerr rotation noise is, just like the Faraday rotation noise, proportional to the spin noise. However, the dependence of the noise power on the laser detuning can be different in a Kerr rotation measurement [cf. Fig. 2.9(b)]. Since the ellipticity ( $\Delta\alpha$ ) is an even function of the probe laser detuning and Faraday rotation ( $\Delta n$ ) is an odd function of the detuning, their sum has in general case an asymmetric dependence [103]. As a result, the measured noise power proportional to the square of  $\mathcal{K}$  is an asymmetric function of the laser detuning. The blue line in Fig. 2.9(b) shows the resulting Kerr rotation noise power spectrum for a phase difference of  $\varphi = 0.1 \pi$  as an example. The exact shape of the noise power spectrum is very sensitive to a variation in  $\varphi$ . Thereby, the analysis of the Kerr rotation noise power spectrum can provide insight into the sample structure, since  $\varphi$  is determined by the traveling length of the probe beam in the sample.



## 3. Experimental Aspects

This chapter discusses the experimental aspects relevant for the measurements and for the results presented in chapter 4. Section 3.1 introduces the QD sample. The measurement setup based on a low-temperature confocal microscope is described in section 3.2. The microscope enables PL characterization of single QDs prior to SN measurements. Detailed descriptions of the PL and SN measurements including technical aspects are given in sections 3.3 and 3.4, respectively.

### 3.1. Sample: Quantum Dots in a Microcavity

The investigated sample and measurements characterizing the microcavity and QD density were provided by K. Pierz (PTB Braunschweig). The measurements are shown in appendix A for reference. The structure of the MBE-grown sample is summarized in Fig. 3.1. Its core is a single layer of self-assembled (InGa)As QDs with a lateral gradient of the QD density varying from zero to about 100 QDs per  $\mu\text{m}^2$ . A density gradient of self-assembled QDs is obtained by exploiting the directionality of the molecular beam in MBE growth. The substrate holder is not rotated during indium deposition which leads to an inhomogeneous InAs coverage of the surface and thereby causes the gradient in the amount of QDs formed on the substrate [44]. The measurements in this thesis focus on QDs in the so called transition region which refers to the segment along the gradient just before the InAs coverage becomes too low for the formation of QDs [44]. In this region the QD density is very low being in the range of 0.1 to 1 QD per  $\mu\text{m}^2$ .

### 3. Experimental Aspects

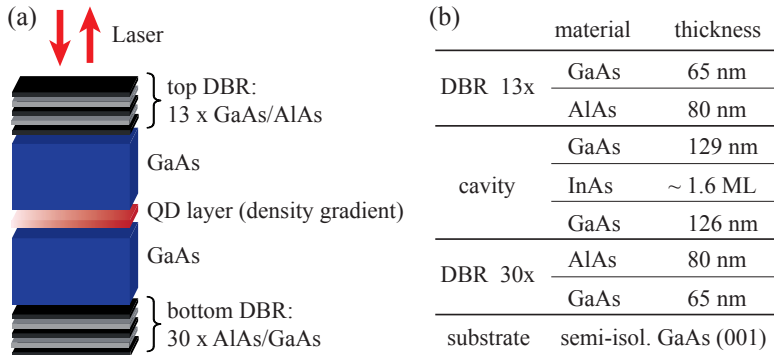


Figure 3.1.: (a) Schematic illustration of the sample structure. (b) Table of the MBE layers [104]. The thickness of the InAs layer varies across the wafer to obtain a gradient of the QD density. For the segment of the wafer studied in this work the InAs thickness is about 1.6 monolayers (ML).

The sample is nominally undoped. However, carbon residuals in the MBE chamber lead to an unintentional  $p$ -type background doping of the GaAs barrier material estimated to be about  $10^{14} \text{ cm}^{-3}$  [104]. This background doping ensures that a fraction of the QDs is occupied by a single hole providing an unpaired spin for SN measurements. The charge status of a specific QD can be deduced from its PL spectrum which will be discussed in Sec. 3.3.

The QD layer is embedded in a planar GaAs microcavity which is designed to have an optical thickness equal to the resonance wavelength of the cavity,  $d_{\text{cav}} = n_{\text{GaAs}} d_{\text{GaAs}} = \lambda_{\text{cav}}$ . The QDs are situated at the center of the cavity, i.e., in the antinode of the field of its fundamental mode. The microcavity is asymmetric meaning that top and bottom mirrors have different reflectivities. The mirrors are realized as MBE-grown distributed Bragg reflectors (DBR). The bottom DBR consists of 30 repetitions of alternating GaAs and AlAs layers of optical thickness  $\lambda_{\text{cav}}/4$ . The top DBR contains only

13 repetitions which results in a slightly lower reflectivity and provides easy optical access to the QDs. The reflectivity of a DBR stack with  $N_{\text{DBR}}$  double layers can be calculated by: [105]

$$R = \left( \frac{n_0(n_{\text{GaAs}})^{2N_{\text{DBR}}} - n_1(n_{\text{AlAs}})^{2N_{\text{DBR}}}}{n_0(n_{\text{GaAs}})^{2N_{\text{DBR}}} + n_1(n_{\text{AlAs}})^{2N_{\text{DBR}}}} \right)^2. \quad (3.1)$$

Here,  $n_0$  is the refractive index of the medium from which the light enters the DBR and  $n_1$  corresponds to the medium behind the DBR. For the bottom DBR  $n_0 = n_1 = n_{\text{GaAs}}$  and  $N_{\text{DBR}} = 30$ , which yields a reflectivity of  $R_{\text{b}} = 0.9999$  according to Eq. (3.1) using  $n_{\text{GaAs}} = 3.508$  and  $n_{\text{AlAs}} = 2.932$ .<sup>1</sup> For the top DBR with  $n_0 = n_{\text{GaAs}}$ ,  $n_1 = 1$  (vacuum) and  $N_{\text{DBR}} = 13$  a reflectivity of  $R_{\text{t}} = 0.9893$  is obtained.

The mirrors provide a high-reflectivity stop band for photon energies in between 1.30 to 1.42 eV which encloses the inhomogeneously broadened PL spectrum of the QD ensemble, cf. App. A. The resonance mode of the microcavity results in a dip in the stop-band reflectivity which is centered at 1.395 eV at the high energy tail of the QD PL spectrum. The dip defines the effective working range for optical measurements. The ratio of the cavity resonance frequency  $\omega_{\text{cav}}$  and the FWHM of the cavity mode  $\Delta\omega_{\text{cav}}$  is defined as the quality (Q-) factor: [106]

$$Q = \frac{\omega_{\text{cav}}}{\Delta\omega_{\text{cav}}}. \quad (3.2)$$

The Q-factor characterizes the microcavity as it is a measure for its capability to store optical energy [107]. The reflectivity and PL measurements depicted in Fig. A.1 indicate a width of the cavity mode of about  $\Delta\omega_{\text{cav}} = 4$  meV. Together with the resonance energy of 1.395 eV at low temperatures Eq. (3.2) yields a rather low measured Q-factor of about 350.

On the other hand, the Q-factor of a planar cavity can be calcu-

---

<sup>1</sup>The values of the refractive indices for GaAs and AlAs correspond to a temperature of 4.2 K and a wavelength of  $\lambda_{\text{cav}} \approx 888$  nm.

### 3. Experimental Aspects

---

lated theoretically by: [108, 109]

$$Q = \frac{2L_{\text{eff}}}{\lambda} \frac{\pi}{1 - \sqrt{R_t R_b}}, \quad (3.3)$$

with the top (bottom) DBR reflectivity  $R_{t(b)}$  and the effective cavity length

$$L_{\text{eff}} = n_{\text{cav}} d_{\text{cav}} + 2 n_{\text{eff}} d_m .$$

Here,  $n_{\text{cav}} = n_{\text{GaAs}}$  is the refractive index of the cavity and  $d_{\text{cav}} \approx 260$  nm is the cavity length.<sup>2</sup> In addition the effective cavity length accounts for the fact that the intra-cavity field significantly expands into the Bragg stacks. The effective mirror thickness which contributes to the cavity length is added in  $L_{\text{eff}}$  with

$$d_m \approx \frac{1}{2} \frac{n_{\text{AlAs}}}{(n_{\text{GaAs}} - n_{\text{AlAs}})} (d_{\text{GaAs}} + d_{\text{AlAs}})$$

as an effective mirror length and

$$n_{\text{eff}} = 2 n_{\text{GaAs}} n_{\text{AlAs}} / (n_{\text{GaAs}} + n_{\text{AlAs}})$$

being the effective refractive index. With a layer thicknesses of  $d_{\text{GaAs}} = 65$  nm and  $d_{\text{AlAs}} = 80$  nm (cf. Fig. 3.1) and the refractive indices as defined above, the effective cavity length results in  $L_{\text{eff}} = 3.3$   $\mu\text{m}$ . The theoretical Q-factor of the structure follows from Eq. (3.3) to be about 4000 for  $\lambda_{\text{cav}} \approx 888$  nm.

The theoretical Q-factor is about an order of magnitude larger than the Q-factor extracted from the measurements in App. A. A large discrepancy between theoretical and experimental Q-values is commonly observed for Bragg mirror microcavities and can be attributed to the following reasons [109–111]: Eq. (3.3) does not take into account any material absorption that might occur in the structure and reduces the Q-factor. In addition, the Q-factor can be decreased due to lateral imperfections of the MBE layers. On the other hand, the lower experimental Q-factor can be a measurement

---

<sup>2</sup>The QD layer is assumed to contribute to the cavity length with a thickness of 5 nm which is a typical height for self-assembled (InGa)As QDs.

artifact due to the finite laser spot size and the spread of the detection angle [110, 111]. However, even the theoretical value of 4000 corresponds to a relatively small Q-factor and in combination with the large mode volume of a planar cavity the light-matter interaction in the presented QD-microcavity structure can clearly be assigned to the weak-coupling regime [112, 113]. Furthermore, the decrease of the radiative lifetime of the QDs due to the Purcell effect is negligible for the small ratio of Q-factor and cavity mode volume [106, 112]. In summary, the microcavity does not alter the physical properties of the QDs but it provides certain benefits for the realization of the single-QD SN measurements. The cavity enables SN measurements in reflection geometry which simplifies the cryogenic cooling of the QDs. Moreover, the ratio of SN signal to optical photon shot noise on the detector is improved as a result of the electric field enhancement in the cavity which enhances the Kerr rotation angle and thereby significantly increases the SN sensitivity [114, 115].

## 3.2. Low-Temperature Confocal Microscope

PL characterization and SN measurements on the QDs are conducted at a cryogenic temperature of 4.2 K. This temperature is reached by mounting the sample at the bottom of a thin-walled tube which is filled with helium exchange gas and inserted in a customary dewar that contains 100 liters of liquid helium. This approach enables a vibration-free and comparatively cost-effective cooling of the sample with a measurement time of about four weeks until most of the liquid helium evaporated and the dewar has to be exchanged.

The tube constitutes the lower part of a confocal microscope. The upper part of the microscope operates at room temperature and contains the optics for PL characterization and SN measurements. The optics are mounted on an optical breadboard which sits on top of the dewar. Optical access to the cooled sample is provided by a window at the top of the tube which is attached to an aperture in the middle of the breadboard. Construction drawings of the microscope can be found in Refs. [116, 117]. A schematic illustration of the

### 3. Experimental Aspects

---

measurement setup is shown in Fig. 3.2. A laser source is coupled into the microscope via an optical fiber. The light is collimated and sent through a linear polarizer which ensures s-polarization. A beam splitter reflects 10 % of the incoming light down to the sample. The transmitted part of the light can be used to monitor the laser power during long-term measurements. At the bottom of the tube the light is focused onto the sample by an aspheric lens with a short focal length which yields a small laser focus with a diameter of about 1  $\mu\text{m}$ . The focusing lens also collects the QD photoluminescence or the Kerr-rotated laser light. In the upward path 90 % of the light from the sample are transmitted through the beam splitter and sent to one of the two detection arms of the microscope. The respective detection path for the light is chosen with a removable mirror. QD PL is sent into the PL-analysis arm which provides a polarization-sensitive detection. The polarized PL is coupled into a fiber which is connected to a high-resolution spectrometer. The PL analysis is discussed in detail in Sec. 3.3. Fluctuations of the Kerr rotation angle containing the spin noise are detected in the SN-spectroscopy arm with a polarization bridge and a balanced photo detector. The detector signal is sent to a computer where it is Fourier-transformed in real time. Small superconducting coils at the bottom of the tube provide a 2D magnetic field ( $B_z, B_x$ ) at the sample of about 30 mT in both directions. The external magnetic fields in longitudinal direction ( $z$  axis, laser propagation and QD-growth direction) and transverse direction ( $x$  axis) facilitate the SN measurements which are discussed in detail in Sec. 3.4.

The QD sample is mounted on piezo driven linear stages which enable accurate positioning of the sample in all three dimensions with a travel range of 5 mm and a spatial resolution of about 200 nm. Positioning in  $x$  and  $y$  direction permits navigation along the QD-density gradient and lateral alignment of single QDs in the center of the laser focus. Automated scanning in  $x$  and  $y$  direction is additionally used to obtain spatial QD-PL maps of small sample areas. These maps serve as a basis to select a single QD for SN measurements and allow to locate a specific QD again after the exchange of the helium dewar (see Sec. 3.3). The positioning in  $z$

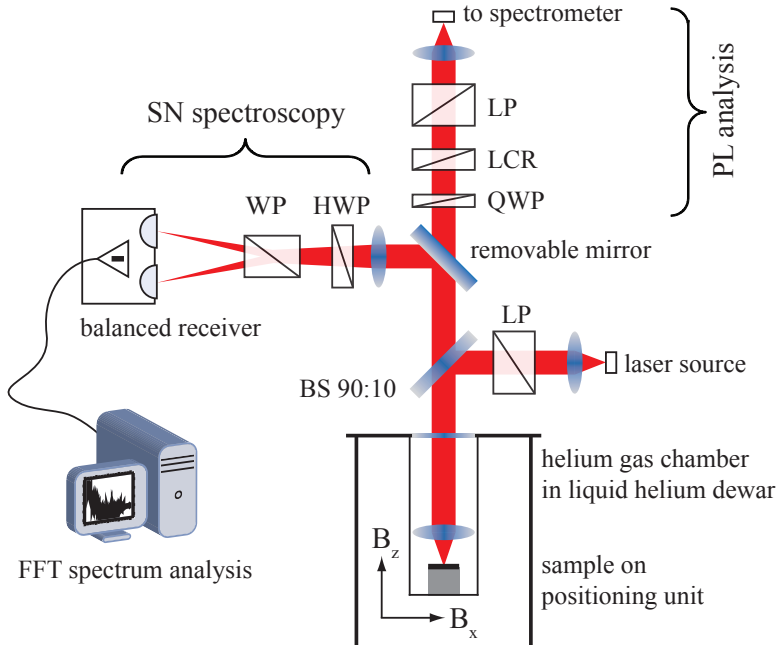


Figure 3.2.: Schematic of the low-temperature confocal microscope for PL and SN spectroscopy on single QDs. The beam splitter (BS) enables measurements in reflection geometry. Quarter-wave plate (QWP), liquid crystal retarder (LCR), and linear polarizer (LP) yield polarization-resolved PL measurements. Half-wave plate (HWP), Wollaston prism (WP) and a balanced photo receiver analyze fluctuations of the Kerr rotation angle for SN spectroscopy.

direction controls the distance between sample and lens to place the QD exactly in the laser focus which ensures maximum PL and SN signals.

The small spatial extent of laser focus and QD makes the measurement setup very vulnerable to external vibrations, especially in the case of long-term SN measurements. For this reason, the whole setup including the helium dewar is lifted on a platform with passive air isolation in order to decouple it from vibrations which could otherwise enter the setup via the laboratory floor.

## 3.3. Photoluminescence

PL spectroscopy is a well-suited tool to characterize and select single QDs for SN measurements. Single-QD SN measurements require a positively charged QD that provides an optical trion transition within the cavity resonance and is spectrally and spatially well separated from other QDs. Spatial scanning of polarization-resolved PL spectra of the sample permits to identify these QDs as outlined in the following.

For PL excitation, the light of a laser diode with a photon energy of 1.59 eV is coupled into the microscope. The high-energy photons excite electron-hole pairs in the GaAs barrier which relax independently into the QDs where they recombine radiatively, thereby revealing the QD resonance energies. A low laser power of about 100 nW is used for excitation since a high excitation power leads to strong saturation broadening of the QD resonances which in turn causes a drastic decrease of the PL signal. The QD PL is sent to a spectrometer with three grating stages providing a high spectral resolution of about 20  $\mu$ eV. The PL spectra are acquired with a low-noise liquid-nitrogen-cooled CCD. In order to distinguish neutral and charged excitons, a polarization-resolved detection of the PL spectra is necessary to reveal the fine-structure splitting of the neutral exciton, cf. Sec 2.1.2. For this purpose, a variable polarization filter is inserted in the microscope to transmit only PL with a selected linear polarization to the spectrometer. The filter consists



of a quarter wave plate, a liquid crystal retarder (LCR), and a linear polarizer (Fig. 3.2). The linear polarizer is aligned parallel to one of the crystal axis of the sample. The LCR in front of the polarizer can be switched between a retardation of  $\lambda/4$  and  $3\lambda/4$ . A quarter wave plate adds a retardation of  $\lambda/4$ . In total, the polarization of the incoming PL is rotated by either  $0^\circ$  or  $90^\circ$ . Hence, the linear polarizer transmits one of the two orthogonal linear polarizations along the crystal axis depending on the retardation at the LCR. These two linear polarizations are labeled  $\pi_x$  and  $\pi_y$  in the following and correspond to the polarizations of the exciton eigenstates which exhibit the small fine-structure splitting  $\Delta E_{\text{FS}}$  in the case of a neutral exciton [50, 51].<sup>3</sup>

Fig. 3.3 shows a typical polarization-resolved PL spectrum of a single positively charged QD. The spectrum shows two optical transitions separated by about  $400 \mu\text{eV}$ . The orthogonally polarized PL components  $\pi_x$  and  $\pi_y$  reveal a fine-structure splitting  $\Delta E_{\text{FS}} \approx 10 \mu\text{eV}$  for the transition at higher photon energy, which is thus attributed to the neutral exciton ( $X^0$ ). Note that  $\Delta E_{\text{FS}}$  is smaller than the absolute resolution of the spectrometer and can only be resolved as a result of the polarization-sensitive detection. The low-energy transition does not show a splitting of the PL components and is therefore assigned to the positively charged trion ( $X^{1+}$ ) (cf. Sec. 2.1.2). The assignment of the optical transitions is in good agreement with the PL studies on similar QDs in Ref. [118]. A low-energy transition without fine-structure splitting can in principle also originate from a negatively charged trion ( $X^{1-}$ ). However, the occurrence of the  $X^{1+}$  is more likely due to the  $p$ -type background doping of the sample and the assignment to the  $X^{1+}$  will also be confirmed by the SN measurements presented in chapter 4. The same pattern of a single-QD PL spectrum, with the  $X^{1+}$  transition observable a few  $100 \mu\text{eV}$  below the  $X^0$  transition, can be recorded for several single QDs on this sample, see e.g., Sec. 4.2 and Ref. [35]. The concurrent observation of the  $X^0$

<sup>3</sup>The polarization of the exciton eigenstates can slightly deviate from the crystal axes, see e.g. Ref. [52]. The extracted value of  $\Delta E_{\text{FS}}$  is not exact in this case but the identification of the neutral exciton is still possible.

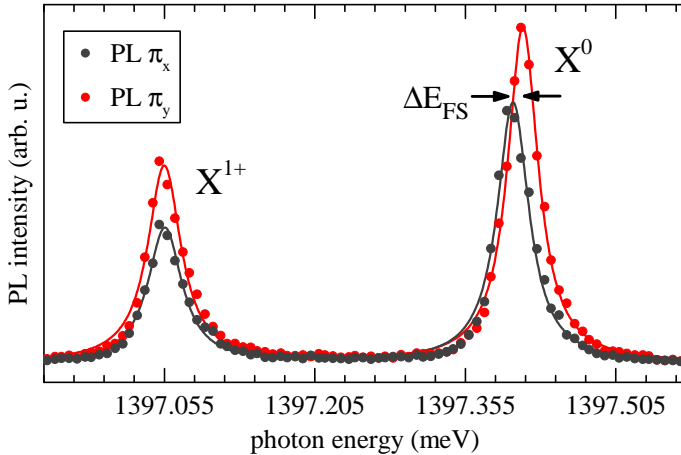


Figure 3.3.: Polarization-resolved PL spectrum of the QD revealing the positively charged trion ( $X^{1+}$ ) and exciton ( $X^0$ ) transition. The fine-structure splitting  $\Delta E_{FS}$  between the linearly polarized PL components  $\pi_x$  and  $\pi_y$  is typical for the uncharged QD state. The solid lines correspond to Lorentzian fits to each PL transition.

transition in the PL spectra of the positively charged QDs might be caused by a faster nonradiative relaxation of free electrons into the QD compared to the relaxation of free holes. However, this circumstance has no effect on the SN studies presented in chapter 4 since the QD is excited resonantly in the respective measurements.

The number of QDs on the sample which are occupied by a resident hole is quite low which is in agreement with the low  $p$ -type doping. The percentage of positively charged QDs is estimated to be only about 5% from the statistical analysis of a large number of PL spectra at different segments along the QD-density gradient, see Ref. [119]. QDs which are not occupied by a resident hole solely exhibit the  $X^0$  transition with a fine-structure splitting in the PL spectra. In order to find a positively charged QD in the sample re-

gion with low QD density, PL spectra on a square of typically a few  $100 \mu\text{m}^2$  are recorded and analyzed by a spatial 2D scanning routine, in steps of  $1 \mu\text{m}$ . This step size coincides with the focal diameter of the lens collecting the PL. Positions where the PL spectra show more resonances than the  $X^0$  and  $X^{1+}$  transition of a single QD are discarded to avoid a contribution to the Kerr rotation noise by other QDs in the probe laser focus. The occurrence of biexcitonic or p-shell recombination is negligible for the applied low excitation power as verified in intensity-dependent PL measurements on selected QDs. The observation of the sole single-QD signature in a PL spectrum can not definitely exclude the presence of additional QDs in the laser focus due to the fact that the width of the microcavity resonance is smaller than the inhomogeneous broadening of the QD distribution (cf. App. A). Additional QDs with an optical transition that is not in resonance with the microcavity are barely visible in the PL spectra due to the high stop-band reflectivity. However, as the cavity resonance is quite broad such QDs are spectrally very well separated from the QD observed within the cavity resonance so that a significant parasitic contribution to the Kerr rotation angle can be excluded.

The cavity resonance was measured at a specific spatial position along the QD gradient to be centered at a photon energy of  $1395 \text{ meV}$ , see Fig. A.1. The segment of the sample studied in this thesis is close to this position and the photon energy of the  $X^{1+}$  transition at  $1397 \text{ meV}$  in Fig. 3.3 lies within the width of the microcavity resonance. Note that the exact energy of the cavity resonance changes along the QD-density gradient which coincides with a gradient in thickness of the cavity as a result of the increased InAs coverage for higher QD densities. This effect was observed in an evaluation of a large number of QD resonances along the QD-gradient, see Ref. [119]. The evaluation also confirms that the PL spectra show mainly QD transitions lying within the resonance of the microcavity.

The specific spectral signature observed for a single charged QD, see Fig. 3.3, is quite unique in the low-density region of the sample. The exact resonance of the trion transition and the energetic sepa-

ration to the exciton transition characterizes each QD individually and thereby a specific QD can be located again after the exchange of the helium dewar. Warming up and cooling down of the lower part of the microscope usually causes a relative shift of the laser position on the sample of about  $10\ \mu\text{m}$  in  $x$  and  $y$  direction.<sup>4</sup> Hence, a PL scan of a  $20\ \mu\text{m} \times 20\ \mu\text{m}$  square in the new full dewar contains the specific QD from former measurements which is identified by its characteristic spectral pattern. This permits to continue the SN investigation on the specific QD. It is important that the SN measurements can be clearly assigned to a specific QD since different QDs can yield very different results depending on their solid-state environment as will be shown in chapter 4.

## 3.4. Spin Noise Spectroscopy

### 3.4.1. Measurement of Kerr Rotation Noise

Spin Noise Spectroscopy exploits the fact that spin fluctuations can be mapped onto the polarization of a probe laser via Faraday or Kerr rotation (cf. Sec. 2.2). In this thesis, the single-QD spin noise is studied in reflection geometry (see Fig. 3.2), corresponding to a measurement of the Kerr rotation noise.

The SN probe laser is a continuous-wave Ti:sapphire ring laser which provides mode-hop-free tuning over a large spectral range (1215–1823 meV) that includes the QD distribution. The laser system is equipped with an external reference cell and a Pound-Drever-Hall stabilization scheme which yields an ultra-narrow optical line width (60 kHz over 100 ms) and a high spectral stability. The long-term spectral stability is further improved with a Fizeau wavelength meter. The probe-laser photon energy measured with high accuracy by the wavelength meter is used as additional reference for the stabilization scheme. In this way a typical long-term laser stability

---

<sup>4</sup>In order to maintain such a small misalignment the microscope has to be handled very carefully during the exchange of the dewar and subsequent cooling down has to be done very slowly.

of  $\pm 10$  neV over many hours up to days is obtained. The spectral stability of the probe laser is essential for the accuracy of the highly detuning-dependent SN measurements on the narrow QD resonances. The impact of the laser stability on single-QD SN measurements has been investigated in detail in Ref. [120].

The stabilized laser is coupled into the microscope via an optical fiber and sent through a linear polarizer. The linearly polarized probe laser follows the same path as the PL excitation laser and is focused onto the sample to interact with the selected QD. The reflected light containing the Kerr rotation noise is collected and travels upwards where the inserted mirror guides the light into the SN-spectroscopy arm to analyze polarization fluctuations (see Fig. 3.2). The polarization fluctuations manifest as small rotations of the polarization plane of the linearly polarized probe light. These rotations are detected by a polarization bridge. The bridge consists of a lens, a half-wave plate, a Wollaston prism and a balanced photo detector. The lens has a long focal distance and focuses the light onto the photo detector. The Wollaston prism splits the light into two orthogonally polarized components which are each detected on one of the two photo diodes of the detector, respectively. The detector measures the intensity difference on the diodes and outputs a voltage signal proportional to this difference. The half-wave plate in front of the Wollaston prism rotates the average dc polarization of the light such that the intensity on the photo diodes is balanced and the mean detector output is zero. This detection scheme is very sensitive to the small rotations of the probe-laser polarization plane induced by the Kerr rotation noise and it translates the polarization rotations into an electrical signal for the noise analysis.<sup>5</sup> In addition, laser intensity fluctuations are efficiently suppressed by the balanced detection scheme.

The balanced detector provides a number of different detection bandwidths in the range of 0.22 to 180 MHz in conjunction with a bandwidth-dependent internal amplification of about  $5 \times 10^7$  to

---

<sup>5</sup>The Kerr rotation noise can be measured with a sensitivity of about  $10^{-15}$  rad<sup>2</sup>/Hz [35, 80].

$5 \times 10^1$  V/W. The detector configurations with a low bandwidth and a high amplification are particularly suitable for the single-QD SN measurements due to the small Kerr rotation angle and the comparably long spin life time associated with a single localized hole [35]. The detector output is sent to a computer where an analog-to-digital converter with a maximum sampling rate of 180 MHz processes the analog voltage signal. The sampling rate of the digitizer can be decreased appropriate to the detector bandwidth. Before digitizing, the detector output voltage is additionally amplified by an external electrical amplifier to optimize the input level for the digitizer card [121]. Finally, the digitized voltage signal is Fourier transformed in real-time and averaged over many time cycles which yields the spin noise power spectral density – in the following shortly referred to as “spin noise spectrum”.

#### 3.4.2. Spin Noise Spectrum and Projection of Spin Components

The spin noise (SN) spectrum shows the Kerr rotation noise power  $\delta\theta_K^2$  in each frequency bin within the detection bandwidth, where the width of the bins—and thereby the resolution of the spectrum—is determined by the FFT-size of the transformation. Figure 3.4(a) shows a SN spectrum of a single localized hole spin measured in a small longitudinal magnetic field of  $B_z = 31$  mT, with a probe-laser detuning of  $\Delta = 44$   $\mu$ eV with respect to the QD trion resonance. Typically,  $(\delta\theta_K^2)_\nu$  follows a Lorentzian line shape as a function of the noise frequency  $\nu$  with the Lorentzian maximum centered at zero frequency. The integrated noise spectrum given by the area of the Lorentzian fit yields the total Kerr rotation noise power which is determined by the refractive index difference of  $\sigma^+$  and  $\sigma^-$  polarized light (see Sec. 2.2.2). The total noise power is a function of the probe-laser detuning with respect to the trion transition and maximum at the HWHM of the optical transition.

The Lorentzian noise spectrum corresponds to an exponential decay of the spin projection in the time domain [33] and the Lorentzian HWHM yields the corresponding spin decay time  $\tau_s$  according to the

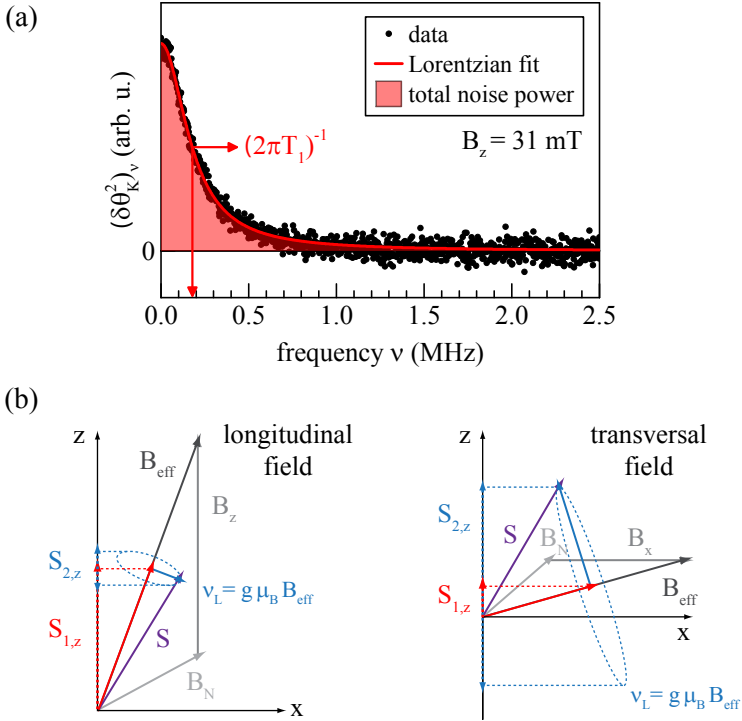


Figure 3.4.: (a) Typical **SN** spectrum acquired in a longitudinal magnetic field of  $B_z = 31$  mT with a laser detuning of  $\Delta = 44$   $\mu\text{eV}$  with respect to the trion resonance. The **HWHM** of the Lorentzian fit yields the longitudinal spin relaxation time  $T_1$ . (b) Schematic illustration of the transverse and longitudinal projection of spin components onto the measurement direction  $z$  in a transverse or longitudinal magnetic field, respectively (cf. Ref. [80]). In a transverse magnetic field the **SN** spectrum is dominated by the transverse spin projection  $S_{2,z}$ . In a longitudinal magnetic field the **SN** spectrum is dominated by the longitudinal spin projection  $S_{1,z}$ .

### 3. Experimental Aspects

---

relation:

$$\tau_s = 1/(2\pi \text{ HWHM}). \quad (3.4)$$

In a longitudinal magnetic field  $\tau_s$  corresponds to the longitudinal spin relaxation time  $T_1$  (c.f. Sec. 2.1.3). In contrast, a transverse magnetic field enables the observation of the transverse spin dephasing time,  $T_2$  or  $T_2^*$ . The relation between  $\tau_s$  and the direction of the magnetic field is explained by the fact that SN spectroscopy is only sensitive to the spin projection  $S_z$  onto the measurement direction  $z$ . Figure 3.4(b) illustrates schematically how the direction of the external magnetic field affects the spin projection onto the measurement direction. The vector addition of the external magnetic field  $\mathbf{B}_{z,x}$  and the stochastically oriented nuclear magnetic field  $\mathbf{B}_N$  yields a total effective magnetic field  $\mathbf{B}_{\text{eff}}$ . The stochastically oriented spin polarization  $\mathbf{S}$  is divided into the longitudinal component  $\mathbf{S}_1$ , which is parallel to  $\mathbf{B}_{\text{eff}}$ , and the transverse component  $\mathbf{S}_2$ , which is perpendicular to  $\mathbf{B}_{\text{eff}}$ . The direction of the longitudinal component stays constant, while the transverse component precesses around the magnetic field direction with a Larmor frequency of  $\nu_L = g\mu_B B_{\text{eff}}/h$ . The probe laser is only sensitive to the projections of these components onto the measurement direction,  $S_{1,z}$  and  $S_{2,z}$ , respectively. The diagram in Fig. 3.4(b) clearly shows that the SN in a transverse magnetic field is dominated by the  $S_{2,z}$  projection which decays with the  $T_2^*$  time.<sup>6</sup> In a longitudinal magnetic field, the SN is dominated by the  $S_{1,z}$  projection which decays with the  $T_1$  time. In general, both times can be visible in the SN spectrum at the same time, see e.g. [75]. In the case of the single-QD SN measurements the longitudinal magnetic field of  $B_z = 31$  mT clearly exceeds the effective nuclear magnetic field of  $B_N \approx 5$  mT [25] which makes the suppression of the  $S_{2,z}$ -projection in the SN spectrum very effective. Furthermore, the  $S_{2,z}$  contribution is significantly broader than the  $S_{1,z}$  contribution since  $T_2^* \ll T_1$  so that the  $S_{2,z}$  noise power is negligible in the small detection bandwidth of 2.5 MHz [see

---

<sup>6</sup>The temporal fluctuations of the nuclear magnetic field lead to inhomogeneous dephasing of the QD spin and thereby to the observation of a  $T_2^*$  time (instead of the  $T_2$  time) in the averaged SN spectrum.



Fig. 3.4(a)]. In addition, the  $S_{2,z}$  contribution is shifted from zero frequency in the SN spectrum to the Larmor frequency. Even small transverse g-factors,  $g_t \ll 1$ , result in a shift of a  $S_{2,z}$  contribution to frequencies well above the detection bandwidth. Altogether, a contribution of the  $S_{2,z}$  projection to the SN spectrum can be neglected and only the  $S_{1,z}$  projection yielding the  $T_1$  time determines the single-QD SN spectrum in the longitudinal magnetic field.

Note that the longitudinal magnetic field of  $B_z = 31$  mT significantly enhances the  $T_1$  time due to suppression of the hyperfine interaction [35]. The prolonged  $T_1$  time yields a narrower Lorentzian SN spectrum compared to the spectrum at zero magnetic field. At the same time, the total noise power is independent of a small external magnetic field. Hence, the constant total noise power is distributed over a smaller frequency range in the SN spectrum if a longitudinal magnetic field is applied. This results in an improved signal-to-noise ratio compared to zero magnetic field and allows for a shorter averaging time of the SN spectrum.

The sensitivity of the SN signal on the magnetic field is further exploited to isolate the SN from other noise sources. This technique will be discussed in the next section.

### 3.4.3. Background Noise and Detector Response Function

The Kerr rotation noise measured by the balanced photo detector is initially massively overlaid by the electrical noise of the detector and the photon shot noise of the probe-laser light. Figure 3.5(a) shows the isolated noise spectra of electrical noise, photon shot noise, and single-QD spin noise on a logarithmic scale for comparison of their respective magnitudes. The electrical noise is the dominant noise source with a noise power spectral density which is an order of magnitude large than photon shot noise and the maximum value of the SN spectrum. The photon shot noise and the maximum of the SN spectral density have the same order of magnitude. Note that photon shot noise and spin noise are both proportional to the probe-laser intensity. The spectra shown in Figure 3.5(a) are measured

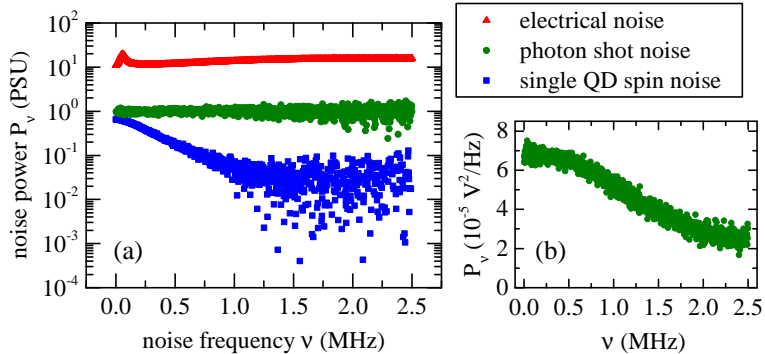


Figure 3.5.: The total measured noise is composed of electrical noise, photon shot noise and spin noise. The noise power spectral densities  $P_\nu$  of the respective contributions are shown individually in (a). They are normalized to the photon shot noise spectrum (PSU: photon shot noise units) in order to account for the detector response function. (b) The measured power spectral density of the photon shot noise reveals the detector response function.

with a moderate probe-laser intensity of  $I = 1.1 \mu\text{W}/\mu\text{m}^2$  and at a laser detuning of  $\Delta = -19 \mu\text{eV}$  with respect to the QD resonance.

The spin noise can be isolated from the dominant noise background (electrical + photon shot noise) exploiting its strong dependence on the direction of an external magnetic field, c.f. Sec. 3.4.2. In a longitudinal magnetic field, the SN is dominated by the  $S_{1,z}$  projection which yields a sharp peak at low frequencies in the noise spectrum. In a transverse magnetic field, the  $S_{1,z}$  projection is strongly suppressed and mainly the  $S_{2,z}$  projection determines the SN. The  $S_{2,z}$  projection decays fast compared to the  $S_{1,z}$  component and yields a broad noise spectrum which is additionally shifted by the Larmor frequency  $\nu_L$ . Hence, for measurements with a small detection bandwidth, e.g. 2.5 MHz (Fig. 3.5), the contribution of the SN to the total noise spectrum acquired in an external transver-

sal magnetic field is negligible. This noise spectrum can therefore be considered as a background-noise measurement since electrical noise and photon shot noise are independent of the magnetic field. A pure SN spectrum (cf. Fig. 3.4) is obtained by subtraction of a spectrum acquired in transverse magnetic field ( $B_x = 27$  mT). The background noise is typically stable on timescales on the order of a few minutes. On longer timescales small variations in the background noise spectrum are observed which might be related to thermal drifts. To ensure clean background subtraction, spectra with and without spin noise are recorded alternatingly with a typical single-spectrum measurement time of about 30 s. The respective difference spectra are subsequently averaged until a good signal-to-noise ratio is obtained. The total measurement time of the averaged SN spectrum depends strongly on the probe-laser intensity and detuning and varies between half an hour and up to 24 hours.

The pure electrical noise spectrum is measured without probe-laser light on the detector. The photon shot noise spectrum is obtained as the difference of a noise spectrum with probe-laser light in a transverse magnetic field (suppression of spin noise) and the dark electrical noise spectrum. Figure 3.5(b) shows a typical photon shot noise spectrum which exhibits a continuous decrease of the measured noise power spectral density towards the detection bandwidth. This decrease is not inherent to the laser photon shot noise which represents broadband white noise [122] and should therefore yield a constant noise spectrum. Instead, the noise spectrum reveals the characteristic frequency-dependent response of the detector, i.e., the detector has an optimal sensitivity for noise at low frequencies which decreases continuously towards the detection bandwidth. The detector response function can alter the SN spectrum significantly, thereby leading to the extraction of inaccurate spin relaxation times. This technical issue is accounted for by a normalization of the measured SN spectrum to the corresponding photon shot noise spectrum. The normalization eliminates the frequency-dependence of the measured noise which is simply related to the sensitivity of the detector. As a result of the normalization, the noise power spectral density is given in units of the photon shot noise which is indicated

### 3. *Experimental Aspects*

---

by the acronym [PSU](#) (c.f. [Fig. 3.5](#)).

## 4. Measurements & Results

**SNS** in the limit of just a single spin confined in a **QD** has been realized only recently [35]. These first measurements were strongly influenced by inhomogeneous broadening of the **QD** resonance due to charge fluctuations in the **QD** environment. This chapter presents **SN** measurements of two specific single **QDs** obtained on the same sample as used in Ref. [35] but in a sample region of lower **QD** density. The **SN** measurements presented in section 4.1 reveal a homogeneously broadened **QD** resonance, which is an evidence for negligible charge fluctuations in the environment. The resonance of the second **QD** investigated in section 4.2 shows a small inhomogeneous broadening on the order of the **QD** linewidth which represents the intermediate situation between the results of Ref. [35] and section 4.1.

**SN** measurements on both **QDs** are conducted in the quasiresonant regime where the laser not only probes the **SN** but also drives the optical transition leading to **SNS** under nonequilibrium conditions. The nonequilibrium **SN** allows to study the trion spin dynamics as well as the heavy-hole spin dynamics and can be interpreted in a dressed-state picture. Moreover, the quasiresonant measurements reveal an additional weak noise contribution which can be assigned to a (re-)occupation noise in the naturally charged **QDs**. The results in section 4.2 show that this additional noise not only contains information on the **QD** occupation but that it can even reveal a hole-capture competition between a **QD** and a nearby ionized acceptor.

The theoretical model presented with the experimental results was developed in collaboration with the Ioffe Institute, by Dmitry Smirnov and Mikhail Glazov. Parts of the results presented in this chapter are published in Refs. [123] and [65].

## 4.1. Homogeneous Broadening and Reoccupation Noise

### 4.1.1. Homogeneous Noise Power Spectrum

The impact of charge fluctuations acting on a QD resonance is linked to the presence of free charges and to the number of charge-binding defects in the surrounding environment. The presence of charges is naturally kept low by the SNS method which avoids nonresonant optical excitation and the number of defects is expected to be lowered by operating in a regime of very low QD density. For the sample under study (cf. sec. 3.1), this should result in a reduced number of ionized acceptors compared to the region of high QD density. The SN investigation presented in the following was conducted on a single QD situated in the low-density region of the sample. The QD density is estimated to be in the range of 0.1 to 1 dot/ $\mu\text{m}^2$  from spatially resolved PL measurements.<sup>1</sup>

Figure 4.1 shows the polarization-resolved PL spectrum of the selected QD. It shows the optical transitions of exciton ( $X^0$ ) and positively charged trion ( $X^{1+}$ ), identified by the fine structure splitting  $\Delta E_{\text{FS}}$  as discussed in detail in Sec. 3.3. The SN measurements are performed with respect to the trion resonance with a probe laser detuning  $\Delta$ . The probe laser is a Ti:sapphire ring laser, stabilized to a Fizeau wavelength meter (cf. Sec. 3.4). All measurements presented in the following are conducted with a laser intensity of  $I = 1.1 \mu\text{W}/\mu\text{m}^2$  and a longitudinal magnetic field of  $B_z = 31 \text{ mT}$  unless noted otherwise.

The dependence of the total SN power on the laser detuning reveals whether the SN results from a QD ensemble or just a single QD. The SN power spectrum  $P_{\text{SN}}(\Delta)$  measured on the selected QD is shown in Fig. 4.1 by the red dots and is clearly linked to the PL trion resonance.  $P_{\text{SN}}(\Delta)$  consists of two maxima which are symmetrically located around the resonance with a sharp dip at  $\Delta = 0$ .

---

<sup>1</sup>A more precise value of the QD density can not be given since only QDs with an optical transition within the cavity resonance are clearly observable in the PL measurements.

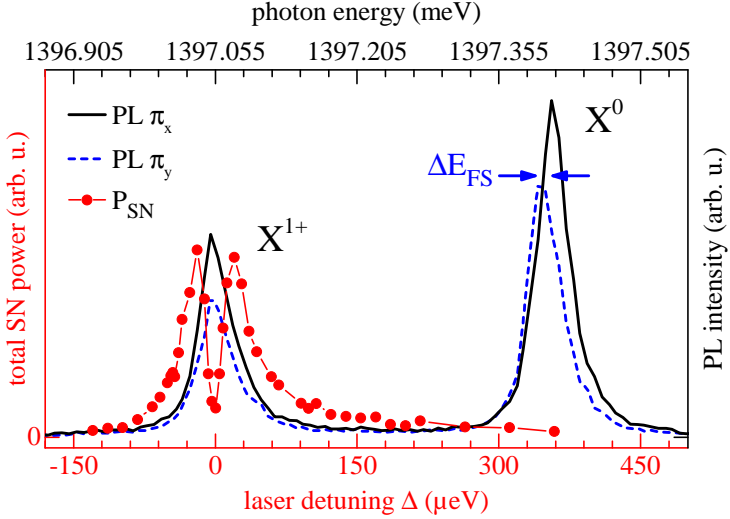


Figure 4.1.: Polarization-resolved PL spectrum of the QD showing the positively charged trion ( $X^{1+}$ ) and exciton ( $X^0$ ) transition. The red dots depict the SN power as a function of laser detuning with respect to the trion resonance. The red line is a guide to the eye.

This distinct shape coincides well with the theoretically expected SN power spectrum of a single homogeneously broadened optical transition (cf. Sec. 2.2.2) and is in stark contrast to the Gaussian line shape observed in Ref. [35]. The double-maximum structure and the pronounced drop in SN power at the trion resonance prove negligible inhomogeneous broadening as shown in Ref. [124] and Sec. 4.2. Thus, charge fluctuations in the environment play a negligible role for this QD.

On closer examination two discrepancies between the measured SN power spectrum and the theoretical spectrum of a homogeneously broadened two-level system become apparent: (i) the SN power minimum at  $\Delta = 0$  does not exactly reach zero power but

maintains a finite value and (ii) the energy distance of the SN power maxima is an order of magnitude larger than the typical optical linewidth of self-assembled QDs of about 1  $\mu\text{eV}$ . A more detailed investigation of the Fourier-transformed SN spectra in the quasi-resonant regime yields insight into the origin of these deviations and is presented in the next sections.

### 4.1.2. Quasiresonant Spin Noise Spectra

The noise spectra of the fluctuations of the Kerr rotation angle  $\delta\theta_K$  are acquired in maximal longitudinal magnetic field  $B_z = 31$  mT to increase the spin-relaxation time  $T_1$  for an improved signal-to-noise ratio and the SN is isolated from laser shot noise and electrical noise by subtracting a spectrum acquired in purely transverse magnetic field  $B_x = 27$  mT (cf. Sec. 3.4). At large probe laser detunings,  $|\Delta| \gtrsim 15$   $\mu\text{eV}$ , the noise spectra show a single Lorentzian line shape corresponding to the spin fluctuations in the QD. Figure 4.2(a) shows the SN spectrum at  $\Delta = -97$   $\mu\text{eV}$  as an example. In this case optical excitation of the QD is very small and the HWHM of the Lorentzian fit yields the spin relaxation time

$$T_1 = 1/(2\pi \text{HWHM}) = 2.51(11) \mu\text{s},$$

which is in good agreement with the hole-spin relaxation time measured on (InGa)As QDs in Refs. [98, 125]. However, using much smaller probe laser intensities a hole-spin relaxation time about two orders of magnitude longer has been observed in Ref. [35] for  $B_z = 31$  mT. This suggests that, despite the large detuning, optical excitation by the probe laser still affects the measured spin relaxation time. Consistently, a decrease of the laser detuning leads to significant broadening of the SN Lorentzian [(cf. Fig. 4.2(b)] which corresponds to a light absorption-induced increase of the spin relaxation rate. The effect of optical excitation on the spin relaxation rate will be discussed in detail in Sec. 4.1.4.

The SN spectra at small laser detunings reveal moreover an additional weak Lorentzian noise contribution as shown in Fig. 4.2(b) for the measurement at  $\Delta = 9$   $\mu\text{eV}$ . The experimental data are well



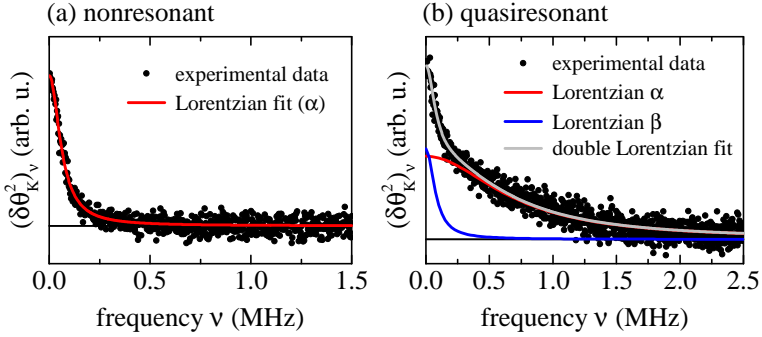


Figure 4.2.: Typical SN frequency spectrum measured with a probe laser energy well detuned from the trion resonance ((a)  $\Delta = -97 \mu\text{eV}$ ) and close to the trion resonance ((b)  $\Delta = 9 \mu\text{eV}$ ).

described by a double-Lorentzian function which is composed of a Lorentzian related to spin fluctuations, termed  $\alpha$  noise contribution, and a new additional Lorentzian, termed  $\beta$  noise contribution in the following. All SN spectra measured in the quasis resonant regime around the trion resonance are analyzed regarding the noise power (Lorentzian area) and the correlation rate (Lorentzian HWHM) of the respective contributions. The resulting detuning dependence of the noise power and correlation rates for  $\alpha$  and  $\beta$  are presented in Fig. 4.3.

The measured noise power spectrum of the  $\alpha$  contribution shown by the red data points in Fig. 4.3(a) agrees well with the theoretical line shape for the SN of a single spin:

$$P_{\text{SN}} = A \frac{\Delta^2}{(\Gamma^2 + \Delta^2)^2}, \quad (4.1)$$

where  $\Gamma$  is the width of the SN power spectrum and  $A$  describes the amplitude of the spectrum. A fit of Eq. (4.1) to the  $\alpha$  data (gray line) yields a relatively large value for  $\Gamma$  of  $17.08(58) \mu\text{eV}$ . The  $\beta$

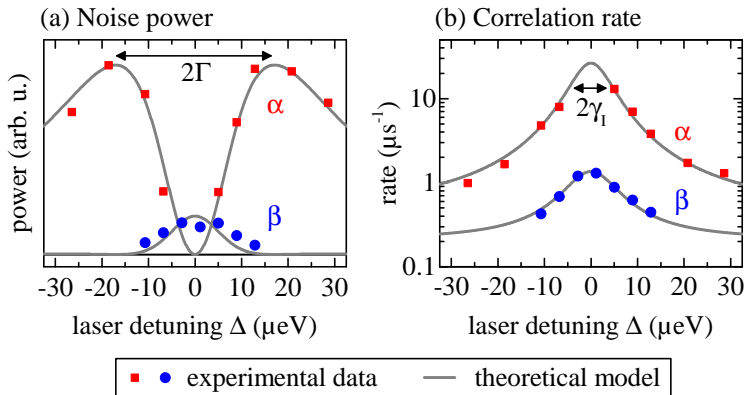


Figure 4.3.: (a) Noise power of  $\alpha$  and  $\beta$  contribution as a function of laser detuning. (b) Correlation rate of  $\alpha$  and  $\beta$  contribution as a function of laser detuning. The gray lines correspond to fit results based on the theoretical model described in the Sec. 4.1.3.

contribution shown by the blue data points in Fig. 4.3(a) exhibits a much lower maximal noise power and the power spectrum is characterized by a different line shape very similar to a Gaussian profile with a maximum at the trion resonance.

The correlation rates of  $\alpha$  and  $\beta$  contribution as a function of  $\Delta$  are shown in Fig. 4.3(b). Both rates exhibit a Lorentzian dependence (gray lines) centered at the trion resonance with a **HWHM**  $\gamma_I \approx 5.4 \mu\text{eV} < \Gamma$ . The  $\alpha$  rate, which is associated with the heavy-hole spin dynamics at large detunings, shows a strong increase by an order of magnitude towards the trion resonance at  $\Delta = 0$ . For laser detunings closest to the trion resonance the  $\alpha$  correlation rate becomes much larger than the measurement detection bandwidth of 2.5 MHz and the  $\alpha$  noise power approaches zero. As a result, the Lorentzian of the  $\alpha$  contribution in the Kerr rotation noise spectrum appears only as a negligibly small constant offset and the cor-

responding values of power and rate could not be extracted. Therefore only the data of the  $\beta$  contribution are displayed in Fig. 4.3 near  $\Delta = 0$ . The correlation rate of the  $\beta$  contribution is for all detunings significantly smaller than the rate of the  $\alpha$  contribution and the  $\beta$  contribution is not observed anymore in the noise spectra for laser detunings  $|\Delta| \gtrsim 15 \mu\text{eV}$ .

The Lorentzian detuning dependence of  $\alpha$  and  $\beta$  correlation rates coincides with the absorption profile of a homogeneously broadened trion transition which implies that optical excitation of the trion significantly influences both noise contributions. In the following it will be shown that the experimental results can be explained by: (i) considering a four-level system of the QD with significant population of the trion states, and (ii) including the occasional escape of the resident hole via an Auger process and the subsequent reoccupation of the QD. The dynamics in between the QD states determine the observed spin noise related to the  $\alpha$  contribution, while the dynamics related to the QD occupation by the resident hole are responsible for the additional  $\beta$  noise contribution.

### 4.1.3. Theoretical Model

The states of the QD and its environment and the transitions between them considered for the theoretical model are depicted in Fig. 4.4. The QD ground state comprises the two heavy-hole spin states with spin projections  $S_z^h = \pm 3/2$  on the growth axis and measurement direction  $z$ . The QD excited state is given by the positively charged trion composed of a pair of holes in the spin singlet state and an electron with the respective spin projections  $S_z^e = \pm 1/2$ . In an external longitudinal magnetic field  $B_z$ , ground and excited spin states exhibit a Zeeman splitting  $\hbar\Omega_z^{h(e)} = \mu_B g_z^{h(e)} B_z$ , with  $g_z^{h(e)}$  being the longitudinal hole and electron g-factor, respectively. Transitions between the hole-spin states are characterized by the hole-spin relaxation rate  $\gamma_s^h = 1/T_1^h$  and, likewise,  $\gamma_s^e = 1/T_1^e$  is the electron-spin relaxation rate between the trion-spin states. Absorption of a  $\sigma^-$  or  $\sigma^+$  photon of the quasiresonant probe-light field in the microcavity enables a transition from the hole  $|\pm 3/2\rangle$  state to

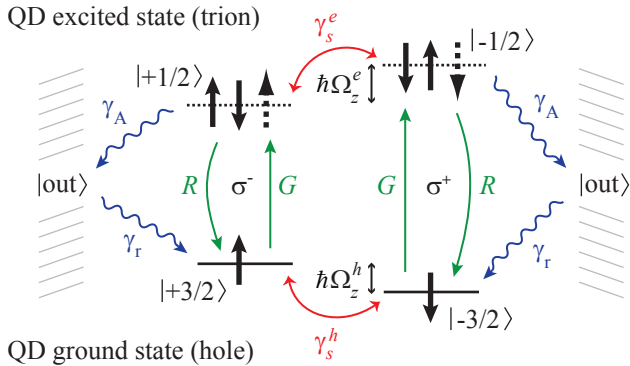


Figure 4.4.: Sketch of the QD states and transitions between them considered in the theoretical model. Note that  $|out\rangle$  on the left and right side of the level diagram denotes the same state, i.e., transitions from  $|\pm 1/2\rangle$  to  $|\mp 3/2\rangle$  via the outer state are possible.

the trion  $|\pm 1/2\rangle$  state, respectively, according to optical selection rules. These transitions are described by a generation rate  $G$ . The recombination of the trion is described by a recombination rate  $R$  and can be induced by stimulated photon emission or spontaneous trion recombination. In addition to the transition back to the QD ground state nonradiative recombination of the trion can take place via an Auger process. The recombination energy is transferred to the resident hole which thus leaves the QD. This process is modeled by the transition to an outer state  $|out\rangle$  in the solid-state environment with the Auger rate  $\gamma_A$ . A tunneling or relaxation process can return a hole from an outer state to the QD ground state with the reoccupation rate  $\gamma_r$ . Note that the state  $|out\rangle$  is a simplified representation for a multitude of outer states and  $\gamma_r$  can be the average transition rate from different outer states. The spin relaxation in the outer states is assumed to be very fast compared to any recapturing process, so that the hole returns to the QD with an arbitrary

spin.

The Hamiltonian of the system in an external magnetic field  $B_z$  in the presence of probe light has the form: [126, 127]

$$\mathcal{H} = \hbar \sum_{\pm} \left[ \omega_0 a_{\pm 1/2}^\dagger a_{\pm 1/2} \pm \frac{1}{2} \Omega_z^h a_{\pm 3/2}^\dagger a_{\pm 3/2} \right. \\ \left. \pm \frac{1}{2} \Omega_z^e a_{\pm 1/2}^\dagger a_{\pm 1/2} + \left( \mathcal{E}_\pm e^{-i\omega t} a_{\pm 1/2}^\dagger a_{\pm 3/2} + \text{h.c.} \right) \right]. \quad (4.2)$$

Here,  $a_{\pm 3/2}$  and  $a_{\pm 3/2}^\dagger$  are the annihilation and creation operators for the resident hole and  $a_{\pm 1/2}$  and  $a_{\pm 1/2}^\dagger$  are the corresponding operators of the trion. The trion resonance frequency is given by  $\omega_0$  and  $\omega$  is the frequency of the incident electromagnetic field. The laser detuning is defined as  $\Delta = \omega - \omega_0$ .  $\mathcal{E}_\pm$  denotes the trion optical transition matrix elements in  $\sigma^\mp$  polarizations. For linearly polarized probe light  $\mathcal{E}_\pm$  is equal to  $\mp \mathcal{E}/\sqrt{2}$ , where  $\mathcal{E}$  is proportional to the amplitude of the incident field and the optical transition dipole moment in the QD. The electromagnetic field can be treated classically since QD and microcavity are in the weak coupling regime.

The eigenstates of the Hamiltonian [Eq. (4.2)] depend on the intensity of the probe light and on the laser detuning. Strong coherent excitation of the QD at small laser detunings ( $|\Delta| < \mathcal{E}$ ) leads to the formation of dressed states [128], which are coherent superpositions of hole and trion states. The lower and upper dressed states (eigenstates) are given by: [65]

$$\Psi_l = \cos \theta |\pm 3/2\rangle + \sin \theta |\pm 1/2\rangle e^{-i\omega t}, \\ \Psi_u = -\sin \theta |\pm 3/2\rangle + \cos \theta |\pm 1/2\rangle e^{-i\omega t}, \quad (4.3)$$

respectively, where  $\theta \in [-\pi/4; \pi/4]$  is determined by

$$\tan(2\theta) = 2\mathcal{E}/\Delta. \quad (4.4)$$

In case of large detunings,  $|\Delta| \gg \mathcal{E}$ ,  $\theta$  approaches zero and the states  $\Psi_{l,u}$  become simply the hole and the trion states. Note that the energy difference between  $\sigma^+$  and  $\sigma^-$  polarized transitions due

to the Zeeman splitting (cf. Fig. 4.4) is neglected here for simplicity. Usually this is a good approximation for self-assembled QDs in a small magnetic field ( $B_z \ll 1$  T) and at high laser intensities since the Zeeman splitting is small compared to the linewidth of the saturation-broadened optical transition [22, 78]. However, the g-factors of electron and hole determining the Zeeman splitting can differ strongly from one QD to another [129], so that the energy difference is not negligible in general case. The consequences of a non-negligible Zeeman splitting will be discussed in Sec. 4.2.

The quantity  $\mathcal{E}$  in Eq. (4.4) can be associated with the quantum electrodynamic resonant Rabi frequency which describes the oscillations of population between ground (hole) and excited (trion) states and corresponds to the splitting between the dressed states at  $\Delta = 0$  [65, 130].

The Hamiltonian in Eq. (4.2) accounts for the coherent processes, e.g., the Rabi oscillations between hole and trion states. The incoherent processes corresponding to spontaneous recombination (with the rate  $\gamma_0$ ), spin relaxation ( $\gamma_s^e, \gamma_s^h$ ), Auger recombination and recharging ( $\gamma_A, \gamma_r$ ), cf. Fig. 4.4, are treated in the density matrix formalism, which yields the following set of coupled equations: [123]

$$\dot{n}_h = 2\mathcal{E}d_x'' + \gamma_0 n_{\text{tr}} + \gamma_r n_{\text{out}}, \quad (4.5a)$$

$$\dot{n}_{\text{tr}} = -2\mathcal{E}d_x'' - \gamma_0 n_{\text{tr}} - \gamma_A n_{\text{tr}}, \quad (4.5b)$$

$$\dot{S}_z^h = -\mathcal{E}d_y' - \gamma_s^h S_z^h + \gamma_0 S_z^e, \quad (4.5c)$$

$$\dot{S}_z^e = \mathcal{E}d_y' - \gamma_s^e S_z^e - \gamma_0 S_z^e - \gamma_A S_z^e, \quad (4.5d)$$

$$\dot{d}_x' = -\Delta d_x'' - \Omega_z d_y'/2 - \gamma d_x', \quad (4.5e)$$

$$\dot{d}_x'' = \mathcal{E}(n_{\text{tr}} - n_h)/2 + \Delta d_x' - \Omega_z d_y''/2 - \gamma d_x'', \quad (4.5f)$$

$$\dot{d}_y' = \mathcal{E}(S_z^h - S_z^e) - \Delta d_y'' + \Omega_z d_x'/2 - \gamma d_y', \quad (4.5g)$$

$$\dot{d}_y'' = \Delta d_y' + \Omega_z d_x''/2 - \gamma d_y''. \quad (4.5h)$$

Here  $n_h$ ,  $n_{\text{tr}}$  and  $n_{\text{out}}$  are the populations of the hole, trion and outer states with  $n_h + n_{\text{tr}} + n_{\text{out}} = 1$ .  $S_z^h$  and  $S_z^e$  are the spin projections of

hole and trion states and  $\hbar\Omega_z = \hbar\Omega_z^e - \hbar\Omega_z^h$  is the total spin splitting between  $\sigma^+$  and  $\sigma^-$  polarized optical transitions.  $\gamma$  is the trion dephasing rate corresponding to the linewidth of the optical transition. In general case  $\gamma$  is greater or equal to  $(\gamma_0 + \gamma_A)/2 + 1/T_2^e + 1/T_2^h$  with  $T_2^{e,h}$  being the hole and trion transverse spin relaxation times. The quantities  $d_x$  and  $d_y$  are proportional to the components of the dipole moment defined in the canonical basis [123] and one or two primes in Eqs. (4.5) denote the real and imaginary parts, respectively. The Faraday rotation angle is proportional to  $d_y''$ . The measured Kerr rotation angle can be contributed to by  $d_y''$  and  $d_y'$ , depending on the interference of the Kerr-rotated light with the light reflected from the top Bragg mirror (cf. Sec. 2.2.2). Here, we assume that the Kerr rotation is mainly determined by  $d_y''$  which is confirmed by the good agreement between theory and data presented below.

Trion generation and recombination in the QD are typically much faster than the processes related to spin and charge dynamics. Therefore a quasi-equilibrium is established on timescales  $\sim \gamma_0^{-1}$  with respect to the optical processes. In the quasi-steady state the time derivatives in Eqs. (4.5) are zero and the equations are linearly dependent as they have to preserve the total spin  $S_z = S_z^h + S_z^e$  and the total QD population  $n = n_h + n_{\text{tr}}$ . Under these assumptions the steady-state probability of trion excitation is found as: [123]

$$\frac{n_{\text{tr}}}{n} = \frac{S_z^e}{S_z} = \frac{G}{G + R}, \quad (4.6)$$

with

$$G = \frac{\mathcal{E}^2 \gamma}{\gamma^2 + \Delta^2}, \quad (4.7)$$

and

$$R = G + \gamma_0. \quad (4.8)$$

The component of the dipole moment  $d_y''$  and thereby the Kerr rotation angle is found as: [123]

$$\theta_K \propto d_y'' = \frac{\mathcal{E} \Delta}{\gamma_I^2 + \Delta^2} S_z - \frac{\mathcal{E}(\gamma_I^2 - \Delta^2)}{4(\gamma_I^2 + \Delta^2)^2} \Omega_z n, \quad (4.9)$$

where

$$\gamma_I = \gamma \sqrt{1 + 2\mathcal{E}^2/(\gamma\gamma_0)} = \gamma \sqrt{1 + (I/I_S)} \quad (4.10)$$

is the trion linewidth renormalized by the laser intensity  $I$ , an effect commonly known as saturation broadening [102].  $I_S$  is the saturation intensity of the optical transition.

Equation 4.9 shows that noise of the Kerr rotation angle can be induced by (i) fluctuations of the total spin  $S_z$ , either related to the hole or trion spin, and (ii) fluctuations of the QD occupancy  $n$ . A discussion of the spin noise (SN), related to the  $\alpha$  contribution presented in Fig. 4.3, follows in the next section 4.1.4. The occupation noise (ON), related to the  $\beta$  contribution in Fig. 4.3, will be discussed in section 4.1.5.

#### 4.1.4. Nonequilibrium Spin Noise

The theoretical analysis in the previous section showed that the nonequilibrium spin noise in the presence of optical excitation is no longer determined simply by the spin of the resident hole, but instead it is related to the pseudospin of the dressed states [Eq. (4.3)]. The corresponding dressed-state spin relaxation rate  $\gamma_s$  which determines the HWHM of the Lorentzian in the SN spectrum [ $\alpha$  contribution in Fig. 4.2(b)] can be derived from Eqs. (4.5c) and (4.5d) taking into account Eq. (4.6). For the pseudospin  $S_z$  follows: [123]

$$\dot{S}_z = -\gamma_s S_z, \quad (4.11)$$

with

$$\gamma_s = \frac{n_h}{n} \gamma_s^h + \frac{n_{tr}}{n} \gamma_s^e, \quad (4.12)$$

being the average spin-relaxation rate, which is intuitively given by the weighted sum of hole-spin relaxation in the ground state and electron-spin relaxation in the excited state, depending on the relative population of hole and trion states. Combining Eqs. (4.6), (4.7) and (4.12) shows that  $\gamma_s$  follows a Lorentzian profile as a function of the detuning  $\Delta$  which is in agreement with the observation depicted in Fig. 4.3(b). The HWHM of the Lorentzian is given by



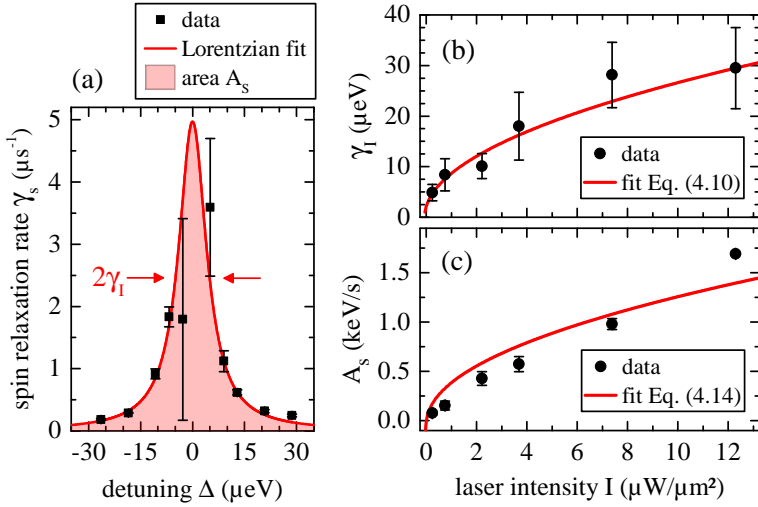


Figure 4.5.: (a) Spin-relaxation rate profile ( $\alpha$  contribution) at  $I = 0.25 \mu\text{W}/\mu\text{m}^2$ . (b) Trion linewidth  $\gamma_I$  as a function of laser intensity extracted from the spin-relaxation rate profiles. (c) Analysis of the area  $A_S$  of the spin-relaxation rate profile as a function of laser intensity enables estimation of the electron-spin relaxation rate. The error bars represent the uncertainty of the respective fit result.

the intensity-dependent trion linewidth  $\gamma_I$  [Eq. (4.10)]. Hence, the trion linewidth can be determined from the spin-relaxation rate profile  $\gamma_s(\Delta)$ . Figure 4.5(b) shows the trion linewidth extracted from the measurement of several spin-relaxation rate profiles at different laser intensities. The profile measured at the lowest laser intensity  $I = 0.25 \mu\text{W}/\mu\text{m}^2$  is exemplarily shown in Fig. 4.5(a) together with the Lorentzian fit yielding the linewidth  $\gamma_I$ . The values of  $\gamma_s(\Delta)$  are obtained from the fits to the  $\alpha$  contribution in the SN spectra (cf. Fig. 4.2). The error bars represent the uncertainty of the fit result. The large uncertainties at small detunings result from

$\gamma_s$  reaching the detection bandwidth (2.5 MHz). Accordingly, the measurements to determine  $\gamma_I$  at higher laser intensities are conducted with higher bandwidths of the tunable balanced detector (5 to 25 MHz, cf. Sec. 3.4). The observed intensity dependence of  $\gamma_I$  is in good agreement with a square-root function and a fit according to Eq. (4.10) yields the intrinsic transition linewidth  $\gamma = 2.2(23)$   $\mu\text{eV}$  and the saturation intensity  $I_S = 0.07(15)$   $\mu\text{W}/\mu\text{m}^2$ . The determination of the QD transition linewidth and saturation intensity is a useful add-on feature of the nonequilibrium SN measurements. These quantities are usually measured by resonance fluorescence, a technique which is experimentally much more challenging to realize compared to the measurement of the Kerr rotation noise [131].

At the same time the intensity-dependent measurement of the spin-relaxation rate profiles can be used to determine the electron-spin relaxation in the trion. For this purpose, the detuning-dependent part of the average spin-relaxation rate is considered:

$$\delta\gamma_s(\Delta) = \frac{G}{G+R}(\gamma_s^e - \gamma_s^h), \quad (4.13)$$

cf. Eq. (4.12) and (4.6). The hole spin relaxation is much slower than the electron spin relaxation, so that  $\gamma_s^h \sim 0$  is assumed in the following. Using the relations Eq. (4.7), (4.8) and  $I/I_S = 2\mathcal{E}^2/(\gamma\gamma_0)$  [cf. Eq. (4.10)] and integrating  $\delta\gamma_s$  over  $\Delta$ , the area of the Lorentzian profile is obtained as a function of the laser intensity: [123]

$$A_S(I) = \frac{\pi}{2} \frac{I\gamma}{\sqrt{I_S(I+I_S)}} \gamma_s^e. \quad (4.14)$$

Figure 4.5(c) shows  $A_S$  as a function of laser intensity extracted from the respective spin-relaxation rate profiles. A fit of Eq. (4.14) using  $\gamma$  and  $I_S$  as determined from Fig. 4.5(b) yields a relatively short electron-spin relaxation time of  $T_1^e = 1/\gamma_s^e = 32.8(32)$  ns, which can be related to the hyperfine interaction [100, 125]. The contribution of the electron spin relaxation rate to the measured average spin relaxation rate (4.12) is determined by the relative trion population (4.6) which can be expressed as a function of probe-laser

intensity  $I$  and laser detuning  $\Delta$ :

$$\frac{n_{\text{tr}}}{n} = \frac{I}{2I_S} \frac{\gamma^2}{(1 + I/I_S)\gamma^2 + \Delta^2}. \quad (4.15)$$

The SN measurement with a large laser detuning of  $\Delta = -97 \mu\text{eV}$  and a laser intensity of  $I = 1.1 \mu\text{W}/\mu\text{m}^2$  shown in Fig. 4.2(a) yield a very low trion population of  $n_{\text{tr}}/n \approx 0.004$ . However, in combination with the high electron spin relaxation rate of about 30 MHz this still yields a significant electron contribution to the average spin relaxation rate (4.12). This electron contribution to the spin relaxation corresponds to a relaxation timescale of a few microseconds. Thus, the measured relaxation time extracted from Fig. 4.2(a),  $T_1 = 2.5 \mu\text{s}$ , is indeed still dominated by the electron spin relaxation. A measurement of the slow hole spin relaxation rate ( $\gtrsim 100 \mu\text{s}$  [35]) at a detuning of about 100  $\mu\text{eV}$  requires a probe laser intensity which is at least an order of magnitude lower than the saturation intensity of the optical transition, i.e.,  $I < 0.007 \mu\text{W}/\mu\text{m}^2$ . In summary, the nonequilibrium SN measurements presented in this chapter are mainly dominated by the electron spin relaxation rate, even at large laser detunings where the optical excitation of the trion is small.

### 4.1.5. Occupation Noise

Recalling the expression for the Kerr rotation angle [Eq. (4.9)] derived in section 4.1.3, the Kerr rotation noise under quasi-resonant driving not only consists of the nonequilibrium SN but is also affected by fluctuations of the QD occupation (ON) as a result of Auger recombination. The noise power of the respective contributions is obtained from the average fluctuations  $\langle \delta\theta_K^2 \rangle$  using the correlation functions  $\langle \delta S_z^2 \rangle = \bar{n}/4$  and  $\langle \delta n^2 \rangle = (1 - \bar{n})\bar{n}$ : [123]

$$P_{\text{SN}}(\Delta) \propto \frac{\mathcal{E}^2 \Delta^2}{(\Gamma^2 + \Delta^2)^2} \bar{n}, \quad (4.16a)$$

$$P_{\text{ON}}(\Delta) \propto \frac{\mathcal{E}^2 (\Gamma^2 - \Delta^2)^2}{4(\Gamma^2 + \Delta^2)^4} \Omega_z^2 (1 - \bar{n}) \bar{n}, \quad (4.16b)$$

cf. Eq. (4.9). Here,  $\bar{n}$  denotes the average steady-state occupation of the QD, and  $\gamma_I$  in Eq. (4.9) is replaced by the renormalized width  $\Gamma \geq \gamma_I$ , which will be discussed in more detail below.

The noise power of the additional ON contribution exhibits a maximum at the trion resonance ( $\Delta = 0$ ) in contrast to the SN power, and the detuning dependence is very similar to a Gaussian function [see Fig. 4.6(a)]. Such a detuning dependence can in principle result from different origins. On the one hand it can be related to the occupation noise with the noise power spectrum given in Eq. (4.16b). The amplitude of the ON power spectrum is a function of the external longitudinal magnetic field due to the trion Zeeman splitting  $\hbar\Omega_z$ . Another possible origin is the spin-splitting noise of the circularly polarized trion transitions due to nuclear spin fluctuations [75]. The nuclear-induced Kerr rotation noise power exhibits exactly the same dependence on the detuning as the ON power but the Zeeman splitting due to the external magnetic field,  $\Omega_z$  in Eq. (4.16b), is replaced by the average amplitude of the Zeeman-splitting fluctuations which result from the nuclear magnetic field,  $\langle \delta\Omega_n^2 \rangle$  [123]. Hence, the noise power of the nuclear spin noise is independent of the external longitudinal magnetic field (similar to the noise power of the SN of the resident charge carrier). Finally, a third possible origin for the observed additional noise power spectrum can be found considering fast charge fluctuations on the order of  $\mu\text{s}$  in the QD environment. The charge noise causes fluctuations of the QD resonance  $\omega_0$  and thereby fluctuations of the laser detuning  $\Delta = \omega - \omega_0$ . Fluctuations of the detuning lead to fluctuations in both terms of the Kerr rotation angle [Eq. (4.9)]. The resulting additional noise contribution of the first (spin-)term in Eq. (4.9) exhibits again a power spectrum of the observed shape. However, this charge-noise contribution depends on the spin correlation function and therefore its correlation time can not be longer than the spin relaxation time [123]. This is in contradiction with the observed correlation rate of the additional contribution which is up to an order of magnitude lower than the spin-relaxation rate [cf. Fig. 4.3(b)]. Charge noise of the second term of the Kerr rotation angle yields a power spectrum that exhibits a different detuning dependence with

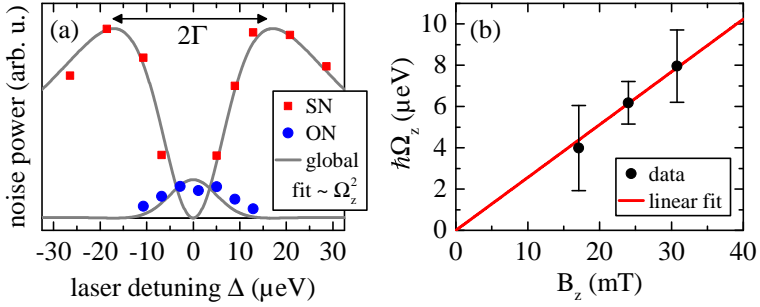


Figure 4.6.: (a) Example of the noise power spectrum of **SN** and **ON** at  $B_z = 31$  mT. The gray lines correspond to a global fit of the data according to Eqs. (4.16) which yields the value of  $\Omega_z$ . (b) Total Zeeman splitting of the trion transition  $\hbar\Omega_z$  as a function of the longitudinal magnetic field  $B_z$ . The error bars correspond to the uncertainty of the fit results.

a dip at the trion resonance [123] which is inconsistent with the observed power spectrum.

Altogether, the assignment of the additional Kerr rotation noise contribution to **ON** can be confirmed by a magnetic-field dependence of the **ON** power spectrum. The trion Zeeman splitting  $\hbar\Omega_z$  determines the amplitude of the **ON** power spectrum with respect to the **SN** spectrum. It can be extracted from the measured noise power by conducting a global fit of Eqs. (4.16) to the **SN** and **ON** data with shared fit parameters  $\Gamma$  and  $\mathcal{E}$  and assuming  $(1 - \bar{n}) \sim 1$ . Figure 4.6(a) shows the noise power spectra and the corresponding global-fit result at a magnetic field of  $B_z = 31$  mT. In Fig. 4.6(b) the trion Zeeman splittings extracted from the respective fits are plotted as a function of the magnetic field. The linear dependence of  $\hbar\Omega_z$  on  $B_z$  is in accordance with the observation of occupation noise and yields a value of  $|g_e - g_h| \sim 4$  for the difference of electron and hole g-factors which is reasonable for (InGa)As QDs [129,132].

At first glance it might be surprising that the fluctuations of QD occupation can be observed as Kerr rotation noise. The essential point for the explanation is that the occupation noise affects the Kerr rotation only in the presence of a longitudinal magnetic field. The external magnetic field leads to a dc Kerr rotation in the case that the laser is quasi-resonant with the trion transition and the QD is charged. SNS is not sensitive to dc signals, but the loss of the charge carrier results in disappearance of the dc Kerr rotation contribution at the trion resonance. Hence, the occupation noise can be understood as a random telegraph signal [60] of the dc Kerr rotation of a charged QD in a magnetic field.

The time scale of the occupancy fluctuations is determined by the Auger recombination and reoccupation dynamics. From Eqs. (4.5a), (4.5b) and (4.6) it follows that: [123]

$$\dot{n} = -\frac{G}{G+R}\gamma_A n + \gamma_r n_{\text{out}}. \quad (4.17)$$

At this point, a model for the outer states has to be adopted to continue the analysis. For simplicity, the outer states are assumed to be given by a single quantum level in the following. Under this assumption the correlation rate of the occupation noise is given by: [123]

$$\gamma_n = \frac{n_{\text{tr}}}{n}\gamma_A + \gamma_r, \quad (4.18)$$

with the Auger recombination rate  $\gamma_A$  and the reoccupation rate  $\gamma_r$ . The rate  $\gamma_n$  depends on the relative population of the trion state and represents a Lorentzian with  $\text{HWHM} = \gamma_I$  as a function of the laser detuning  $\Delta$ , similar to the dressed-state spin relaxation rate (cf. Sec. 4.1.4). Close to the trion resonance  $\gamma_n$  is dominated by Auger recombination and for large detunings  $\gamma_n$  tends towards the reoccupation rate. Hence, the intensity-dependent measurements of the occupation-rate profile  $\gamma_n(\Delta)$  can be used to determine  $\gamma_A$  in a similar way as presented for the electron-spin relaxation rate  $\gamma_s^e$  in Sec. 4.1.4. The QD reoccupation is assumed to be much slower than Auger recombination<sup>2</sup>,  $\gamma_r \sim 0$ , and only the detuning-dependent

<sup>2</sup>This assumption is consistent with a small average QD occupation  $\bar{n}$ , which

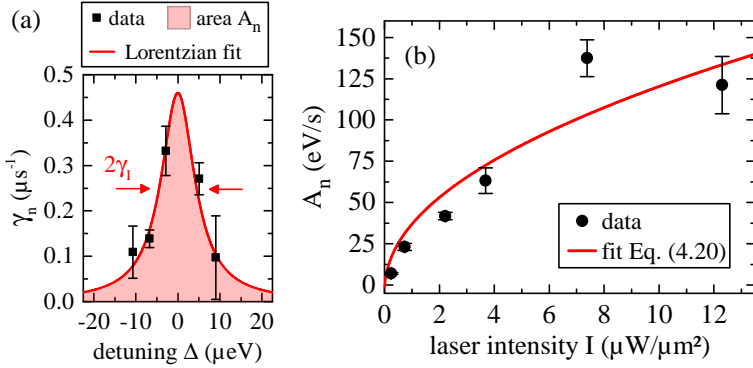


Figure 4.7.: (a) Occupation-rate profile ( $\beta$  contribution) at  $I = 0.25 \mu\text{W}/\mu\text{m}^2$ . (b) Analysis of the area of the occupation-rate profile  $A_n$  enables estimation of the intrinsic Auger recombination rate. The error bars represent the uncertainty of the respective fit result.

part of the occupation rate is considered:

$$\delta\gamma_n(\Delta) = \frac{G}{G+R}\gamma_A. \quad (4.19)$$

Using the relations Eq. (4.7), (4.8) and  $I/I_S = 2\mathcal{E}^2/(\gamma\gamma_0)$ , and integrating  $\delta\gamma_n$  over  $\Delta$ , yields the Lorentzian area as a function of the laser intensity: [123]

$$A_n(I) = \frac{\pi}{2} \frac{I\gamma}{\sqrt{I_S(I+I_S)}}\gamma_A. \quad (4.20)$$

Figure 4.7(b) shows  $A_n$  as a function of laser intensity as it is determined from the measured occupation-rate profiles. As an example Fig. 4.7(a) shows the occupation-rate profile at the lowest laser intensity of  $I = 0.25 \mu\text{W}/\mu\text{m}^2$  together with the Lorentzian

---

is essential for the observation of occupation noise [see Eq. (4.16b)].

fit which yields  $A_n$ . The data  $\gamma_n(\Delta)$  are obtained from the fits to the  $\beta$  contribution in the SN spectra (cf. Fig. 4.2) and the error bars represent the uncertainty of the fit result. Note that the number of data points obtained for the occupation-rate profile is lower compared to the spin-relaxation rate profile [Fig. 4.5(a)] since the ON power drops much faster to zero than the SN power, cf. Fig. 4.6(a). The theoretical analysis shows that both profiles have the same Lorentzian width  $\gamma_I$ , therefore  $\gamma_I$  is adopted from the spin-relaxation rate profiles (Fig. 4.5) to decrease the fit uncertainty of  $\gamma_n(\Delta)$  and the resulting value of  $A_n$ . A fit of Eq. (4.20) to the experimentally determined Lorentzian areas is shown in Fig. 4.7(b). Based on the results in Sec. 4.1.4 the intrinsic linewidth  $\gamma = 2.2 \mu\text{eV}$  and the saturation intensity  $I_S = 0.07 \mu\text{W}/\mu\text{m}^2$  are used for the fit, which yields a value of  $\gamma_A = 2.93(28) \mu\text{s}^{-1}$  for the Auger rate. This value is in very good agreement with recent measurements of the Auger recombination in similar QDs via resonance fluorescence [28].

The rate of the QD reoccupation is given by  $\gamma_n(\Delta)$  at large detunings where the trion population tends towards zero [cf. Eq. (4.18)]. But due to the fast decreasing ON power it is not possible to measure  $\gamma_n(\Delta)$ , and thereby the reoccupation rate  $\gamma_r$ , directly at sufficiently large detunings. However,  $\gamma_r$  can be estimated from the offset of the occupation-rate profile. A good Lorentzian fit result is achieved for the data set presented in Fig. 4.3(b) which contains the highest number of data points as a function of  $\Delta$  for the presented measurements. The fit yields a reoccupation rate of  $\gamma_r = 0.207(96) \mu\text{s}^{-1}$ , suggesting that the average reoccupation of the QD is slow in the studied sample in agreement with the low  $p$ -type background doping (cf. Sec. 3.1).

It is important to note that the exact detuning dependence of the SN and ON noise power [Eqs. (4.16)] also depends on the details of charge dynamics in the outer states, as they are a function of the average QD occupation. In the simplest case of just a single quantum level describing the outer state, the average QD occupation



is found to be: [123]

$$\bar{n} = \frac{\gamma_r(G + R)}{\gamma_r(G + R) + \gamma_A G}. \quad (4.21)$$

Substituting  $\bar{n}$  into the expression for the noise power [Eqs. (4.16)] yields: [123]

$$P_{\text{SN}} \sim \frac{2(\mathcal{E}\Delta)^2}{(\gamma_I^2 + \Delta^2)(\gamma_2^2 + \Delta^2)}, \quad (4.22a)$$

$$P_{\text{ON}} \sim \frac{(\mathcal{E}\Omega_z)^2(\gamma_2^2 - \gamma_I^2)(\gamma_I^2 - \Delta^2)^2}{4(\gamma_I^2 + \Delta^2)^3(\gamma_2^2 + \Delta^2)^2}, \quad (4.22b)$$

with the additional width:

$$\gamma_2 = \sqrt{\gamma_I^2 + \frac{\gamma_A \gamma \mathcal{E}^2}{\gamma_r \gamma_0}}. \quad (4.23)$$

One can see that  $\gamma_2$  is larger than  $\gamma_I$  as a consequence of Auger recombination and this results in a broadening of the noise power spectra beyond  $\gamma_I$ . This broadening can be understood intuitively, especially in the case of the SN power. The efficient emptying of the QD leads to a strong reduction of the average SN power at small detunings, while the SN power at larger detunings is barely affected since Auger recombination gets less probable. As a result the SN power maxima shift to larger detunings, yielding a width of the power spectrum which is larger than the linewidth  $\gamma_I$ .

The noise power spectra in Eqs. (4.22) describe the measured noise power spectra qualitatively correctly. However, they do not provide a good quantitative agreement. The reason is most likely the strong simplification to a single outer state. For this reason the measured noise power spectra are described by Eqs. (4.16), which use a phenomenological renormalization of  $\gamma_I$  to  $\Gamma$ , to account for the additional broadening. Although the charge dynamics in the outer states modify the noise power spectra, they do not affect the spin relaxation rate  $\gamma_s$  [Eq. (4.12)], which was derived without any assumptions about the outer state. The charge dynamics outside the

QD only affect the second term of the occupation rate  $\gamma_n$  [Eq. (4.18)] which becomes relevant just at large detunings where Auger recombination is not dominant anymore. This fact ensures the reliable determination of electron-spin relaxation rate, QD linewidth, saturation intensity, and Auger recombination rate.

In summary, the presented results reveal the capability of SNS to study not only the nonequilibrium spin dynamics but also the charge dynamics in the system in the presence of a small external magnetic field. The occupation noise, which was observed in a SNS measurement for the first time, enabled a quantitative analysis of the Auger process in self-assembled (InGa)As QDs. In fact, the occupation noise can even provide further insight into the charge dynamics in the QD environment as will be shown for a special case presented in the next section.

## 4.2. Inhomogeneous Broadening and Acceptor-Occupation Noise

In contrast to atoms, the results found on a specific self-assembled QD can not be generalized to every QD, not even to QDs on the same wafer. Many of the physical properties depend strongly on the QD's size, material composition and morphology [45, 112, 129]. In addition, the nature of the solid-state environment surrounding the QD, e.g. the presence of defects, significantly alters the single-QD physics. This section presents Kerr rotation noise measurements on a second QD in the sample region of low QD density which yield some complementary results to the measurements presented in section 4.1.

Figure 4.8(a) shows the polarization-resolved PL spectrum of the QD which is qualitatively very similar to the QD-PL spectrum in Sec. 4.1. The optical transitions corresponding to the positively charged trion ( $X^{1+}$ ) and the exciton ( $X^0$ ) resonances are both shifted to slightly higher photon energies by about 0.3 meV compared to the QD investigated in Sec. 4.1. The Kerr rotation noise relating to the trion transition is measured in a longitudinal mag-

netic field of  $B_z = 31$  mT and with a probe-laser intensity of  $I = 0.4 \mu\text{W}/\mu\text{m}^2$ . Figure 4.8(b) shows the noise spectrum of the Kerr rotation angle on a logarithmic scale for a laser detuning of  $\Delta = -22.6 \mu\text{eV}$  with respect to the trion resonance. The noise spectrum at this comparably large detuning shows a single-Lorentzian line shape and is solely determined by spin noise (SN). The HWHM of the Lorentzian yields a spin relaxation time of  $1.3 \mu\text{s}$  which approaches the intrinsic hole-spin relaxation time but still contains a contribution related to the electron-spin relaxation due to residual absorption [cf. Eq. (4.12)].

### 4.2.1. A More Complex Form of Occupation Noise

The QD occupation noise becomes relevant for the Kerr rotation noise spectra at smaller laser detunings shown in Fig. 4.8(c) and (d) for  $\Delta = -6.9 \mu\text{eV}$  and  $\Delta = 1 \mu\text{eV}$ , respectively. Indeed, these spectra show a significant noise contribution at lower frequencies in addition to the SN. But instead of a single additional Lorentzian (cf. Sec. 4.1), two Lorentzians (labeled ON-D and ON-O) are observed here. The HWHM of the two Lorentzian contributions differ by an order of magnitude. However, both contributions exhibit an increase of their width and total noise power with decreasing laser detuning and clearly dominate the Kerr rotation noise spectrum close to the trion resonance [Fig. 4.8(d)]. The HWHM of the SN Lorentzian also shows a strong increase for smaller laser detunings due to the increased probability of trion population and the corresponding stronger influence of the short electron-spin relaxation time, in agreement with the nonequilibrium SN discussed in Sec. 4.1.4. The assignment of the contributions to SN and ON, respectively, is confirmed by laser-detuning and magnetic-field dependent measurements of the respective noise power of each contribution. The noise power of each contribution is extracted from the Lorentzian fits to the measured Kerr rotation noise spectra (cf. Fig. 4.8). Figure 4.9(a) shows the respective noise powers as a function of the laser detuning for a longitudinal magnetic field of  $B_z = 31$  mT. The SN contribution is again identified by the distinct double-maximum

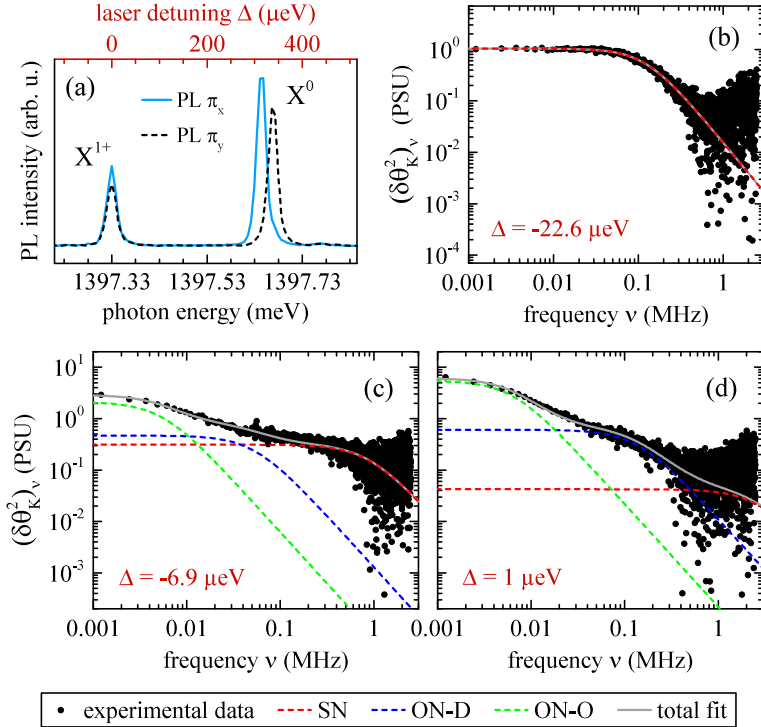


Figure 4.8.: (a) Polarization-resolved PL spectrum of the QD showing the trion resonance at 1397.33 meV. (b)-(d) Kerr rotation noise spectra measured at different laser detunings  $\Delta$  with respect to the trion resonance. The spectrum at large detunings (b) is solely determined by spin noise (SN). The additional low-frequency contributions in the spectra at smaller detunings (c and d) can be assigned to occupation noise (ON-D and ON-O). The solid gray lines correspond to a joint fit of the measured spectra with the sum of the three Lorentzian functions.

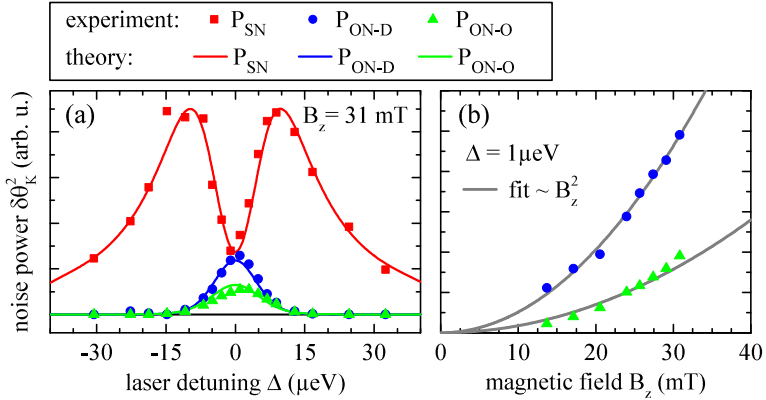


Figure 4.9.: (a) Noise power of all three noise contributions as a function of the laser detuning. The solid lines correspond to the respective noise power calculated by Eqs. (4.35) of the theoretical model (Sec. 4.2.3). (b) Noise power of the two low-frequency contributions (ON-D and ON-O) as a function of the longitudinal magnetic field.

line shape of the noise power spectrum  $P_{\text{SN}}(\Delta)$  which is characteristic for spin fluctuations (cf. Sec. 4.1). The noise power spectra of the two additional contributions,  $P_{\text{ON-D}}(\Delta)$  and  $P_{\text{ON-O}}(\Delta)$ , show a single maximum at the trion resonance ( $\Delta = 0$ ) in agreement with occupation noise theory. The unambiguous assignment to occupation noise further demands the investigation of the noise power as a function of the longitudinal magnetic field  $B_z$ , as outlined in Sec. 4.1.5. Figure 4.9(b) shows the noise power of ON-D and ON-O as a function of  $B_z$  at a small laser detuning of  $\Delta = 1 \mu\text{eV}$ . The noise power of both contributions increases proportional to the square of  $B_z$  which confirms that both contributions correspond to occupation noise since the ON power is proportional to the square of the trion Zeeman splitting  $\hbar\Omega_z$  [see Eq. (4.16b)]. The observation of

more than one contribution to the occupation noise suggests more complex charge dynamics in the QD environment compared to the QD investigated in Sec. 4.1. In particular, the strongly differing correlation times associated with the Lorentzian HWHMs of ON-D and ON-O indicate two distinct reoccupation channels for this QD after Auger recombination: one channel is characterized by a very long reoccupation time (ON-O), while the other channel provides a much faster reoccupation of the QD (ON-D). A detailed model for the charge dynamics between the QD and its environment will be presented in Sec. 4.2.3 together with a theoretical analysis.

### 4.2.2. Broadening due to Slow Charge Fluctuations

The more complex occupation noise is not the only deviation apparent in the experimental results compared to the measurements in Sec. 4.1. The measured SN power shown in Fig. 4.9(a) as a function of the laser detuning (the red squares) is not dropping to zero at  $\Delta = 0$  [c.f. Eq. (4.16a)], but maintains a significant value of about one third of the noise power maxima. This “imperfect” dip of the SN power spectrum at the trion resonance signifies the presence of slow charge fluctuations in the QD environment [124]. Stochastic fluctuations of charges in the solid-state environment are commonly observed in self-assembled QDs and occur typically on the order of milliseconds [27, 133]. The redistribution of charges leads to a continuous change of the trion resonance energy via the Stark effect with shifts typically on the order of a few  $\mu\text{eV}$  [64]. The resonance fluctuations translate into fluctuations of the laser detuning and thereby affect the Kerr rotation angle. Fast charge fluctuations on the order of microseconds manifest themselves as additional noise contributions in the Kerr rotation noise spectrum (cf. Sec. 4.1.5 and Ref. [123]). Slow changes of the resonance frequency on a millisecond timescale do not affect individual noise spectra, but become visible in the detuning-dependent quantities extracted from the time-averaged spectra, e.g. the total noise power. In fact, the charge fluctuations result in an inhomogeneous broadening of the average trion resonance over time. In order to account for this

inhomogeneous broadening, the noise power spectrum of a homogeneously broadened optical transition,  $P_{\text{SN/ON}}^0(\Delta)$  [cf. Eqs. (4.16)], has to be convolved with a Gaussian distribution of the fluctuating trion resonance shifts:

$$P_{\text{SN/ON}}^{\delta\omega_0}(\Delta) = \int P_{\text{SN/ON}}^0(\Delta') \frac{e^{-(\Delta-\Delta')^2/(\delta\omega_0)^2}}{\sqrt{\pi}\delta\omega_0} d\Delta', \quad (4.24)$$

where  $\delta\omega_0$  is the mean amplitude of the slow resonance changes. The resulting modification of the homogeneous noise power spectrum depends on the magnitude of the inhomogeneous broadening with respect to the homogeneous linewidth  $\gamma_I$  of the optical transition. For the SN power spectrum, a small inhomogeneous broadening  $\delta\omega_0 \lesssim \gamma_I$  results primarily in a “smearing” of the narrow noise power dip at  $\Delta = 0$ . This leads to the increase of the noise power from zero to a finite value at the (average) trion resonance, as it is present in the data shown in Fig. 4.9(a). A large inhomogeneous broadening,  $\delta\omega_0 \gg \gamma_I$ , leads to complete disappearance of the noise power dip and the SN power spectrum simply follows the Gaussian distribution  $\exp[-(\Delta/\delta\omega_0)^2]$  which was observed in Ref. [35]. For the ON power spectra, the modification due to the inhomogeneous broadening is less noticeable. The convolution with the Gaussian distribution of resonance fluctuations leads to a stretching of the homogeneous ON power spectrum causing a slightly lower maximal power and a larger width of the spectrum.

Note that not only the noise power, but all detuning-dependent quantities are modified by the inhomogeneous broadening. This includes the probability of the trion population which determines the average spin relaxation rate, and also the effective Auger recombination rate which finally defines the average QD occupation. A detailed analysis of these quantities including the inhomogeneous broadening is presented in the following section using a refined version of the theoretical model developed in Sec. 4.1 to describe the differing observations on the present QD.

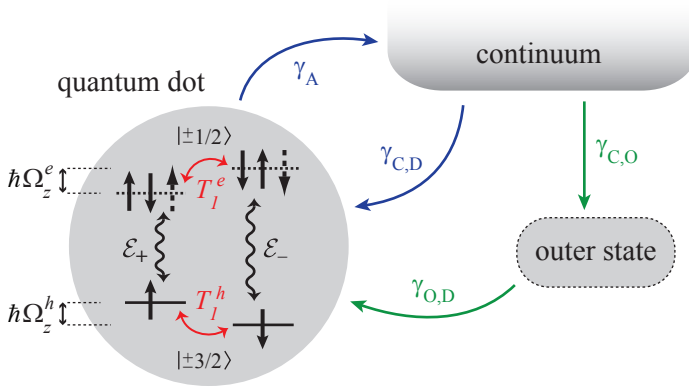


Figure 4.10.: Sketch of ground and excited spin states in the QD and of the hole states in the QD environment. The arrows illustrate all relevant transitions considered for the theoretical model.

### 4.2.3. Theoretical Model of Coupled Spin and Charge Dynamics

Figure 4.10 illustrates the underlying scenario described by the theoretical model. The quantum dot is still described by the four-level system including the hole ground states with the spin projections  $|\pm 3/2\rangle$  and the excited trion states with the spin projections  $|\pm 1/2\rangle$ . The states are coupled by  $\sigma^-$  and  $\sigma^+$  polarized laser light, respectively, which is denoted by the trion optical transition matrix elements  $\mathcal{E}_\pm$  (cf. Sec. 4.1.3). The spin dynamics in the ground state are characterized by the hole-spin relaxation time  $T_1^h$ , while in the excited state the unpaired electron determines the spin relaxation with the time  $T_1^e$  which is typically much shorter than  $T_1^h$ .

Trion recombination can lead to an Auger process which excites the resident hole into the continuum and leaves an empty QD behind. The probability of Auger recombination is determined by the



intrinsic Auger rate  $\gamma_A$  and the population of the trion states. After an Auger process the QD is recharged by a hole with an arbitrary spin. According to the two ON contributions in the Kerr rotation noise spectra (Fig. 4.8) the recharging of the QD can take place via two different channels. The first recharging channel is linked to the broader contribution ON-D and enables a fast reoccupation of the QD. This process is modeled by direct recharging of the QD from the continuum with a rate  $\gamma_{C,D}$ , where  $C$  and  $D$  label the continuum and the (quantum) dot, respectively. The second recharging channel is linked to the narrow ON contribution ON-O and should be significantly slower than the first channel. The slow channel is modeled with a single localized outer state in the immediate vicinity of the QD. On account of the  $p$ -type background doping, the outer state will most likely correspond to an ionized acceptor which provided a hole for the QD initially. The acceptor is assumed to be situated within a distance of a few Bohr radii of the acceptor hole ( $a_B^{acc} \approx 2 \text{ nm}$  [134]) with respect to the QD. In this scenario, QD and ionized acceptor compete for a hole after Auger recombination since Coulomb repulsion effectively suppresses simultaneous occupation of acceptor and QD. Hence, after Auger recombination either the QD is charged with the rate  $\gamma_{C,D}$  or the acceptor, representing the outer state in Fig. 4.10, is charged with a rate  $\gamma_{C,O}$  ( $O$  denotes the outer state). Charging of the outer state inhibits charging of the QD from the continuum due to Coulomb repulsion and only a tunneling process from the outer state can recharge the QD with a slow rate  $\gamma_{O,D}$ .

At first glance, a number of slightly different models of charge dynamics are conceivable to describe the observed Kerr rotation noise spectra. In particular, it can be assumed that Coulomb repulsion between outer state and QD is weak enough, such that both can be charged with a hole at the same time. Furthermore, a charged outer state in the vicinity of the QD should result in a significant Stark shift of the trion resonance compared to an empty outer state (consistent with the charge fluctuations responsible for inhomogeneous broadening, cf. Sec. 4.2.2). The shift of the resonance with respect to the fixed probe-laser energy alters the probability for

Auger recombination which can result in two differing ON contributions linked to the charge status of the outer state. However, the theoretically calculated Kerr rotation noise spectra based on such alternative models show results which are in contradiction with the measured Kerr rotation noise spectra. Appendix B presents the calculated Kerr rotation noise spectra of the alternative theoretical descriptions and outlines their deviation to the measured spectra. In the following, the theoretical derivation of the Kerr rotation noise spectra based on the Coulomb-repulsion model (described above) is presented. The resulting calculated noise spectra are in good agreement with the experimental results and enable the determination of the parameters of spin and charge dynamics in Sec. 4.2.4.

The QD interacting with the probe light in a longitudinal magnetic field is described by the Hamiltonian defined in Eq. (4.2) and the eigenstates of the Hamiltonian are the dressed states which are coherent superpositions of the hole and trion states, cf. Sec. 4.1.3. For the QD investigated in this section, the Zeeman splitting  $\hbar\Omega_z$  is on the order of the trion linewidth  $\gamma_T$ , as will be shown by the comparison of experiment and theory in Sec. 4.2.4. In this case, the Zeeman splitting should not be neglected in the theoretical analysis since it results in important consequences for the spin and charge dynamics of the system. In the first place, the effective probe-laser detuning differs for light interaction with the “spin up” or “spin down” states and is given by  $\Delta_+ = \Delta + \Omega_z/2$  and  $\Delta_- = \Delta - \Omega_z/2$ , respectively (cf. Fig. 4.10). As a result, the upper and lower dressed states [Eq. (4.3)] depend on the orientation of the QD pseudo spin  $S_z = \pm 1/2$  and are given by: [65]

$$\begin{aligned}\Psi_t^\pm &= \cos\theta_\pm |\pm 3/2\rangle + \sin\theta_\pm |\pm 1/2\rangle e^{-i\omega t}, \\ \Psi_u^\pm &= -\sin\theta_\pm |\pm 3/2\rangle + \cos\theta_\pm |\pm 1/2\rangle e^{-i\omega t},\end{aligned}\tag{4.25}$$

respectively, with  $\theta_\pm \in [-\pi/4; \pi/4]$  being determined by

$$\tan(2\theta_\pm) = 2\mathcal{E}_\pm/\Delta_\pm.\tag{4.26}$$

The incoherent processes related to recombination and dephasing are again treated in the density matrix formalism and evaluated for

the quasi-steady state with respect to the much faster optical processes (cf. Sec. 4.1.3). This approach yields the quasi-steady state occupancies of the hole and trion states  $n_s$  with  $s = \pm 3/2, \pm 1/2$ , and in particular the probability for excitation of the respective trion states: [65]

$$\frac{n_{\pm 1/2}}{n_{\pm 3/2} + n_{\pm 1/2}} = \frac{\mathcal{E}^2 \gamma}{\gamma_0(\gamma_I^2 + \Delta_{\pm}^2)}, \quad (4.27)$$

where  $\gamma$  denotes the intrinsic trion linewidth,  $\gamma_0$  corresponds to the spontaneous recombination rate, and  $\gamma_I$  is the “dressed” trion linewidth renormalized by the light intensity ( $\propto \mathcal{E}^2$ ), cf. Eq. (4.10). In contrast to Sec. 4.1, the excitation probability is not equal for both trion spin states, but depends on the orientation of the pseudo spin with respect to the magnetic field due to  $\Delta_{\pm}$ . The effective Auger rate  $\tilde{\gamma}_A$  is given by the product of trion excitation probability and intrinsic Auger rate, which ultimately results in a coupling of spin orientation and QD occupation via the external magnetic field.

The Kerr rotation angle is again deduced from the imaginary part of the component  $d_y$  of the dipole moment, yielding: [65]

$$\theta_K \propto \frac{\mathcal{E}}{(\gamma_I^2 + \Delta_+^2)(\gamma_I^2 + \Delta_-^2)} \times \left[ 4\Delta(\gamma_I^2 - \frac{\Omega_z^2}{4} + \Delta^2)S_z - \Omega_z(\gamma_I^2 + \frac{\Omega_z^2}{4} - \Delta^2)n \right], \quad (4.28)$$

which is qualitatively similar to Eq. (4.9): both, fluctuations of the pseudo spin, as well as fluctuations of the QD occupation, will lead to Kerr rotation noise.

The kinetic equations for spin and charge dynamics based on the phenomenological model introduced in Fig. 4.10 are given by: [65]

$$\dot{S}_z = -S_z/\tilde{T}_1 + \lambda n, \quad (4.29a)$$

$$\dot{n} = -\tilde{\gamma}_A n - \lambda' S_z + \gamma_{C,D}(1 - n - n_{\text{out}}) + \gamma_{O,D} n_{\text{out}}, \quad (4.29b)$$

$$\dot{n}_{\text{out}} = \gamma_{C,O}(1 - n - n_{\text{out}}) - \gamma_{O,D} n_{\text{out}}. \quad (4.29c)$$

Here, the average spin relaxation time  $\tilde{T}_1$ , the effective Auger rate  $\tilde{\gamma}_A$ , and the coupling parameters between QD pseudo spin and occupancy,  $\lambda$  and  $\lambda'$ , have been introduced as

$$\frac{1}{\tilde{T}_1} = \frac{\gamma_I^2 + \Omega_z^2/4 + \Delta^2}{2T_1^e \Gamma^2}, \quad (4.30a)$$

$$\tilde{\gamma}_A = \gamma_A \frac{\gamma_I^2 + \Omega_z^2/4 + \Delta^2}{2\Gamma^2}, \quad (4.30b)$$

$$\lambda = -\frac{\Delta\Omega_z}{4T_1^e \Gamma^2}, \quad (4.30c)$$

$$\lambda' = \gamma_A \frac{\Delta\Omega_z}{\Gamma^2}, \quad (4.30d)$$

$$\text{with } \Gamma = \sqrt{(\gamma_I^2 + \Delta_+^2)(\gamma_I^2 + \Delta_-^2)}/\gamma_I. \quad (4.30e)$$

The Eqs. (4.30) are only valid in the limit of a large probe-laser intensity ( $I \gg I_S$ ) and if the pseudo spin relaxation is dominated by electron-spin flips, i.e.,  $1/T_1^e \gg 1/T_1^h, \gamma_A$ . These criteria are fulfilled for the measurements presented in this thesis, cf. Sec. 4.1. However, in general case Eqs. (4.30) are more complex, cf. Ref. [65].

The kinetic Eqs. (4.29) demonstrate the coupling of QD pseudo spin  $S_z$  and occupancy  $n$  by the external magnetic field which has two main consequences: (i) the rate of emptying of the QD depends on its pseudo spin and (ii) the quasi-resonant excitation of the QD in a longitudinal magnetic field leads to a spin polarization. The spin polarization follows from the unequal optical pumping of “spin up” and “spin down” states in conjunction with the much slower spin relaxation in the ground states compared to the trion states ( $T_1^h \gg T_1^e$ ). As a result, the ground and excited spin states with the larger effective laser detuning  $\Delta_+$  provide a longer average spin relaxation time  $\tilde{T}_1$  compared to the states with smaller detuning  $\Delta_-$  which have a higher average population of the trion state yielding a shorter  $\tilde{T}_1$ . The superior conservation of the pseudo spin orientation in the states with larger laser detuning leads to a preferential

spin orientation over time and determines the average spin polarization. Note, that the unequal spin population due to optical pumping with the linearly polarized probe-light becomes only relevant if the effective Zeeman splitting  $\hbar\Omega_z$  is at least on the order of the trion linewidth.

The average spin polarization  $\bar{P}_z$ , the average QD occupation  $\bar{n}$ , and the average occupation of the outer state  $\bar{n}_{out}$  are found from Eqs. (4.29) as: [65]

$$\bar{P}_z = \frac{2\bar{S}_z}{\bar{n}} = -\frac{\Delta\Omega_z}{\gamma_I^2 + \Omega_z^2/4 + \Delta^2}, \quad (4.31a)$$

$$\bar{n} = \frac{\gamma_{O,D}(\gamma_{C,O} + \gamma_{C,D})}{\gamma_{O,D}(\gamma_{C,O} + \gamma_{C,D}) + (\gamma_{O,D} + \gamma_{C,O})\left(\lambda\lambda\tilde{T}_1 + \tilde{\gamma}_A\right)}, \quad (4.31b)$$

$$\bar{n}_{out} = (1 - \bar{n})\gamma_{C,O}/(\gamma_{C,O} + \gamma_{O,D}), \quad (4.31c)$$

and completely define the steady state of the QD.

Fluctuations of the average quantities in Eqs. (4.31) lead to the fluctuations of the Kerr rotation angle and the experimental results suggest that these fluctuations occur on three well separated timescales. The spin fluctuations, which are dominated by the electron spin relaxation time, define the shortest timescale. The intermediate timescale is determined by Auger recombination and direct QD recharging from the continuum. The slowest process results from hole capture to the outer state and subsequent tunneling to the QD. In summary this yields:

$$\frac{1}{\tilde{T}_1} \gg \tilde{\gamma}_A, \gamma_{C,D} \gg \gamma_{C,O}, \gamma_{O,D}, \quad (4.32)$$

with three corresponding contributions to the Kerr rotation noise given by spin noise (SN), QD occupation noise (ON-D), and additionally noise of the outer-state occupation (ON-O). The outer-state occupation noise manifests in the Kerr rotation noise of the QD by forcing a longer period of QD reoccupation in the case of an occupied outer state, which blocks the hole-capture from the continuum due

to Coulomb repulsion. Hence, the varying periods with an empty QD defining the QD occupation noise include the information about the occupation of the outer state.

The Kerr rotation noise spectrum is obtained as the Fourier transform of the correlation functions of the fluctuations of spin, QD occupation, and outer-state occupation. The correlation functions are deduced with the quantum regression theorem for the separation of timescales defined in Eq. (4.32). The detailed derivation can be found in Ref. [65] yielding the final result:

$$\begin{aligned}
 (\delta\theta_K^2)_\nu &= A_S \frac{2\pi\tilde{T}_1}{1 + (2\pi\tilde{T}_1\nu)^2} \\
 &+ A_D \frac{\gamma'_A/2\pi}{(\gamma'_A/2\pi)^2 + \nu^2} + A_O \frac{\gamma'_{C,O}/2\pi}{(\gamma'_{C,O}/2\pi)^2 + \nu^2}.
 \end{aligned} \tag{4.33}$$

The calculated Kerr rotation noise spectrum consists of three Lorentzian contributions centered at zero frequency with the three correlation rates:

$$1/\tilde{T}_1, \tag{4.34a}$$

$$\gamma'_A = \tilde{\gamma}_A + \lambda\lambda'\tilde{T}_1 + \gamma_{C,D}, \tag{4.34b}$$

$$\gamma'_{C,O} = \gamma_{C,O} + \gamma_{O,D} - \gamma_{C,O}\gamma_{C,D}/\gamma'_A, \tag{4.34c}$$

corresponding to the respective Lorentzian HWHM multiplied by  $2\pi$ . The coefficients  $A_S$ ,  $A_D$ , and  $A_O$  in Eq. 4.33 correspond to the total noise power of the respective contributions and are given by:

$$A_S = 2C_s \left( \langle \delta\theta_K \delta S_z \rangle - \lambda\tilde{T}_1 \langle \delta\theta_K \delta n \rangle \right), \tag{4.35a}$$

$$A_D = 2 \left( C_s \lambda\tilde{T}_1 + C_n \right) \left( \langle \delta\theta_K \delta n \rangle + \frac{\gamma_{C,D}}{\gamma'_A} \langle \delta\theta_K \delta n_{out} \rangle \right), \tag{4.35b}$$

$$A_O = -2 \left( C_s \lambda\tilde{T}_1 + C_n \right) \frac{\gamma_{C,D}}{\gamma'_A} \langle \delta\theta_K \delta n_{out} \rangle. \tag{4.35c}$$

Here,  $C_s$  and  $C_n$  are the coefficients of spin and occupation contributions to the Kerr rotation angle, which follow from Eq. (4.28) as:

$$C_s = \frac{4\mathcal{E}\Delta (\gamma_I^2 - \Omega_z^2/4 + \Delta^2)}{(\gamma_I^2 + \Delta_+^2) (\gamma_I^2 + \Delta_-^2)}, \quad (4.36a)$$

$$C_n = -\frac{\mathcal{E}\Omega_z (\gamma_I^2 + \Omega_z^2/4 - \Delta^2)}{(\gamma_I^2 + \Delta_+^2) (\gamma_I^2 + \Delta_-^2)}, \quad (4.36b)$$

and the correlators in Eqs. (4.35) are given by: [65]

$$\langle \delta\theta_K \delta S_z \rangle = C_s \left( \frac{\bar{n}}{4} - \bar{S}_z^2 \right) + C_n \bar{S}_z (1 - \bar{n}), \quad (4.37a)$$

$$\langle \delta\theta_K \delta n \rangle = C_s \bar{S}_z (1 - \bar{n}) + C_n \bar{n} (1 - \bar{n}), \quad (4.37b)$$

$$\langle \delta\theta_K \delta n_{out} \rangle = -C_s \bar{S}_z \bar{n}_{out} - C_n \bar{n} \bar{n}_{out}. \quad (4.37c)$$

Finally, the Kerr rotation noise spectrum  $(\delta\theta_K^2)_\nu$  [Eq. (4.33)] has to be convolved with the Gaussian distribution of frequency fluctuations  $\delta\omega_0$  in order to account for the inhomogeneous broadening of the trion transition due to slow charge fluctuations, cf. Sec 4.2.2:

$$(\delta\theta_K^2)_\nu^{\delta\omega_0}(\Delta) = \int (\delta\theta_K^2)_\nu(\Delta') \frac{e^{-(\Delta - \Delta')^2 / (\delta\omega_0)^2}}{\sqrt{\pi} \delta\omega_0} d\Delta'. \quad (4.38)$$

#### 4.2.4. Comparison of Experiment and Theory

The theoretical calculation of the Kerr rotation noise according to Eq. (4.38) involves a number of physical quantities describing the studied QD and its environment. These quantities are summarized in Tab. 4.1 and determined by adjusting the calculated Kerr rotation noise spectra to the experimentally observed spectra using the physical quantities as adjustable parameters. The Kerr rotation noise spectra have been measured at eighteen different laser detunings in the range from  $\Delta = -35 \mu\text{eV}$  to  $\Delta = 35 \mu\text{eV}$ , cf. Sec. 4.2.1. The set of parameter values yielding a good agreement between the calculated and measured Kerr rotation noise spectra for all detunings is displayed in Tab. 4.1. Figure 4.11 shows the calculated Kerr rotation noise spectra together with the measured spectra at four different laser detunings as an example. In addition, the solid lines

#### 4. Measurements & Results

---

physical quantity	symbol	value
“dressed” homogeneous trion linewidth	$\gamma_I$	4.3(6) $\mu\text{eV}$
inhomogeneous broadening	$\hbar\delta\omega_0$	4.5(2) $\mu\text{eV}$
effective Zeeman splitting at 31 mT	$\hbar\Omega_z$	5.2(7) $\mu\text{eV}$
electron spin relaxation time	$T_1^e$	24(8) ns
Auger recombination rate	$\gamma_A$	2.0(4) $\mu\text{s}^{-1}$
QD reoccupation rate from continuum	$\gamma_{C,D}$	0.7(1) $\mu\text{s}^{-1}$
outer-state reoccupation rate from cont.	$\gamma_{C,O}$	0.06(1) $\mu\text{s}^{-1}$
QD reoccupation rate from outer state	$\gamma_{O,D}$	0.03(1) $\mu\text{s}^{-1}$

Table 4.1.: Parameters of spin and charge dynamics determined by comparison of the theoretical calculations and experimental results.

in Fig. 4.9(a) show the calculated noise power of the three contributions as a function of the laser detuning [cf. Eqs. (4.35)] for the parameter values given in Tab. 4.1, showing good agreement with the noise powers extracted from the measured spectra. In the following, the relation of each specific physical quantity to distinct characteristics observed in the measured spectra will be outlined, which is important for the estimation of the physical quantities regarding the large number of parameters to adjust the calculated spectra.

The physical quantities related to the optical transition, namely, the homogeneous trion linewidth  $\gamma_I$ , the inhomogeneous broadening  $\hbar\delta\omega_0$ , and the effective Zeeman splitting  $\hbar\Omega_z$ , follow most clearly from the detuning dependence of the noise powers presented in Fig. 4.9(a). The homogeneous linewidth is the main determinant of the energy splitting between the two noise power maxima of the SN contribution. The splitting is reproduced best by the calculated noise power for a value of  $\gamma_I = 4.3 \mu\text{eV}$ . The inhomogeneous broadening follows from the finite SN power value at  $\Delta = 0$ , which is determined by the ratio between homogeneous and inhomogeneous broadening [124]. Comparison with the observed noise power  $P_{\text{SN}}$  closest to  $\Delta = 0$  yields an inhomogeneous broadening of  $\hbar\delta\omega_0 = 4.5 \mu\text{eV}$  which is on the order of the homogeneous



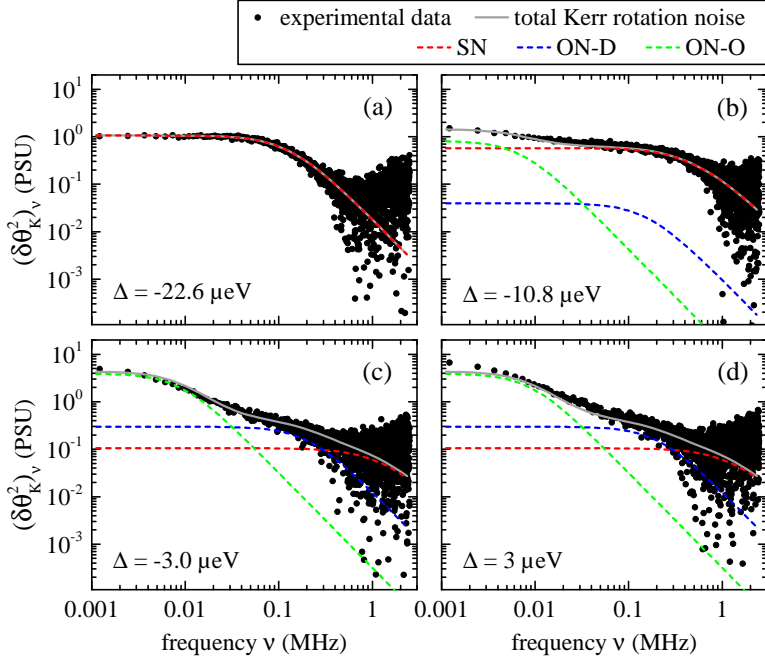


Figure 4.11.: Comparison between measured and calculated Kerr rotation noise spectra at different laser detunings  $\Delta$  with respect to the trion resonance. The noise spectra are calculated according to Eq. (4.38) using the parameters summarized in Tab. 4.1. The total Kerr rotation noise at large detunings (a) is fully described by SN. The Kerr rotation noise at smaller detunings (b to d) includes the occupation noise of the QD (ON-D) and the outer state (ON-O).

broadening. The effective Zeeman splitting between hole and trion spin states can be deduced from the ratio of **SN** to **ON** power (cf. Sec. 4.1.5). The measurements performed in an external magnetic field of  $B_z = 31$  mT suggest an absolute value of the trion Zeeman splitting of  $\hbar\Omega_z = 5.2$   $\mu\text{eV}$ .

Knowing the characteristics of the optical transition, the electron-spin relaxation rate can be extracted from the Lorentzian **HWHM** of the **SN** spectra (red dashed lines in Fig. 4.11), which is proportional to the average spin relaxation rate  $1/\tilde{T}_1$  [Eq. (4.30a)]. Good agreement between measured and calculated **SN** spectra is achieved for  $T_1^e = 24$  ns which is consistent with the electron-spin relaxation time found in Sec. 4.1.4 and Ref. [100]. Note that  $\tilde{T}_1$  is significantly longer than  $T_1^e$  as it depends on the average trion population. The trion population can in theory reach a maximum value of 1/2 in the case of fast Rabi oscillations. Here, this maximum value is decreased by the non-negligible Zeeman splitting and the inhomogeneous broadening of the investigated **QD**. In addition, the hole-spin relaxation rate is neglected in  $\tilde{T}_1$ . This is a good approximation for the quasiresonant **SN** spectra at laser detunings  $|\Delta| \lesssim 25$   $\mu\text{eV}$  (cf. Fig. 4.11) but leads to a deviation between the calculated and measured spectra for larger detunings (not shown) where the electron-spin relaxation is not clearly dominating  $\tilde{T}_1$  anymore.

In the following, the quantities related to the charge dynamics will be discussed. The Auger recombination rate  $\gamma_A$  and the rate for direct **QD** recharging  $\gamma_{C,D}$  follow from the **ON-D** spectra (blue dashed lines in Fig. 4.11). The sum of  $\gamma_A$  and  $\gamma_{C,D}$  determines the **HWHM** of the spectrum [Eq. (4.34b)]. At the same time, their ratio is essential for the average occupation of the **QD** which determines the total noise power [Eq. (4.35b)] and thereby the amplitude of the **ON-D** spectrum. Amplitude and width of the experimental spectra are well reproduced by the calculation for  $\gamma_A = 2$   $\mu\text{s}^{-1}$  and  $\gamma_{C,D} = 0.7$   $\mu\text{s}^{-1}$  in agreement with the results in Sec. 4.1.5 and Ref. [28]. Similarly, the **ON-O** spectrum (green dashed lines in Fig. 4.11) is determined by the sum and ratio of the charging rate of the outer state  $\gamma_{C,O}$  and its emptying rate  $\gamma_{O,D}$ , given by the tunneling into the **QD**. Here, comparison with the experimental spectra yields

$$\gamma_{C,O} = 0.06 \mu\text{s}^{-1} \text{ and } \gamma_{C,D} = 0.03 \mu\text{s}^{-1}.$$

All in all, the physical quantities of spin and charge dynamics can be estimated quite well from comparison with the experimental spectra, despite the large number of adjustable values and the complexity of the theoretical expression for the total Kerr rotation noise spectrum [Eq. (4.38)]. The theoretical Kerr rotation noise spectra show an overall good agreement with the set of experimental noise spectra at different detunings. However, for positive detunings a deviation between experimental and theoretical Kerr rotation noise spectra can be observed compared to the spectra at negative detunings. The deviation can be seen comparing Fig. 4.11(c) and 4.11(d) which show the spectra at  $\Delta = -3 \mu\text{eV}$  and  $\Delta = 3 \mu\text{eV}$ , respectively. The theoretical Kerr rotation noise spectra are symmetric in  $\Delta$  and thus identical for positive and negative detuning. In contrast, the experimental spectrum at positive detuning shows a slightly higher amplitude compared to the spectrum at negative detuning. This deviation becomes more pronounced for higher absolute values of  $\Delta$  resulting in a reduced agreement between experimental and theoretical spectra at positive laser detunings compared to the good agreement at negative laser detunings [Fig. 4.11(a)-(c)]. On the one hand, the asymmetry of the experimental spectra in  $\Delta$  can be caused by fluctuations of charges in further localized states in the wider QD environment (cf. App. B), i.e., the description of charge noise by a Gaussian distribution in Eq. (4.38) is too simplified. On the other hand, an asymmetry can also be caused by an ellipticity contribution to the Kerr rotation noise which depends on the interference of the Kerr rotated light with the laser light reflected at the top Bragg mirror of the cavity (cf. Sec. 2.2.2). Accounting for these additional effects to describe the asymmetry correctly would lead to a much higher complexity of the theoretical modeling, but should not significantly alter the parameters of spin and charge dynamics summarized in Tab. 4.1.

Using the quantities in Tab. 4.1, the average spin polarization [Eq. (4.31a)] and the average occupation [Eq. (4.31b)] describing the steady state of the QD can be calculated as a function of the laser detuning. The resulting curves are shown in Fig. 4.12. Figure 4.12(a)

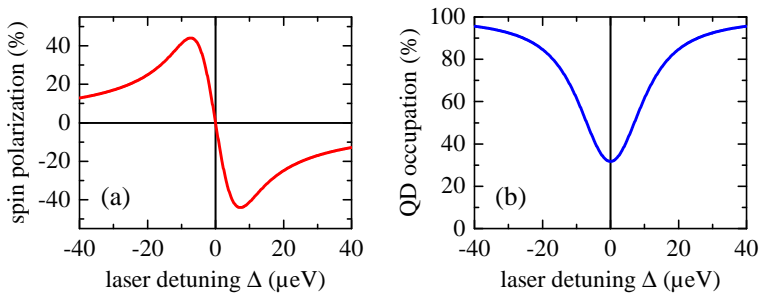


Figure 4.12.: (a) Calculated degree of the average spin polarization in the QD as a function of laser detuning according to Eq. (4.31a). (b) Calculated average occupation of the QD as a function of laser detuning according to Eq. (4.31b). The parameters used for the calculation are given in Tab. 4.1.

shows that the Zeeman splitting (on the order of the homogeneous linewidth) results in a significant spin polarization by optical pumping with linearly polarized light. The degree of spin polarization is maximum at a laser detuning of  $|\Delta| = \sqrt{\gamma_I^2 + \Omega_z^2}/4 \approx 5 \mu\text{eV}$  reaching almost 50%, with the spin orientation depending on the sign of the detuning. Figure 4.12(b) shows the average QD occupation resulting from the interplay of Auger recombination, direct QD recharging from the continuum, and slow recharging via the ionized acceptor (outer state). Comparison of the rates  $\gamma_{C,D} = 0.7 \mu\text{s}^{-1}$  and  $\gamma_{C,O} = 0.06 \mu\text{s}^{-1}$  shows that the capture cross section of the QD is an order of magnitude larger than the capture cross section of the acceptor. However, the hole-tunneling time from the acceptor into the QD is very slow with  $1/\gamma_{O,D} \approx 33 \mu\text{s}$  causing long time periods with an empty QD in the case of hole-capture by the acceptor. This reduces the average occupation of the investigated QD by a hole to only 30% for resonant driving of the trion transition [cf. Fig. 4.12(b)]. Note that the tunneling-time between QD and

acceptor depends exponentially on their distance. For this reason, a slightly different configuration of QD and acceptor can potentially result in a much lower average QD occupation, leaving the QD effectively uncharged under resonant optical driving.

In summary, the Kerr rotation noise measurements on a second QD together with the refined theoretical model provide two main results. Firstly, the concept of nonequilibrium SN and Auger-recombination-induced occupation noise could be confirmed, as well as the corresponding quantities determined in Sec. 4.1. Furthermore, the understanding of the QD spin and charge dynamics in the presence of resonant optical driving could be extended to more complex environmental conditions: a significant Zeeman splitting of the spin states due to the external magnetic field and an ionized acceptor in the QD environment. The Zeeman splitting leads to a spin polarization via optical pumping and to a coupling of the spin and charge dynamics. The adjacent acceptor alters the recharging dynamics which leads to an additional contribution in the QD occupation noise. The analysis revealed that QD and acceptor compete for a single hole, which results in a significant decrease of the average QD occupation.



## 5. Conclusion & Outlook

This thesis presented spin noise spectroscopy on single hole spins in QDs under nonequilibrium conditions due to resonant driving of the optical transition. The measurements in combination with a theoretical analysis showed that the spin fluctuations in the presence of optical driving are strongly influenced by the electron spin dynamics in the excited trion state. The nonequilibrium spin relaxation rate is found to be a combination of hole spin relaxation in the ground state and electron spin relaxation in the trion state. The relative contributions of electron and hole spin relaxation are determined by the relative population of ground and excited states in the QD. The electron spin relaxation rate in the trion state is found to be very high, i.e., on the order of 30 to  $42 \mu\text{s}^{-1}$  in a longitudinal magnetic field of  $B_z = 31 \text{ mT}$ . The high electron spin relaxation rate can be related to the efficient hyperfine interaction between the electron spin and the nuclear spins. The small magnetic field of  $B_z = 31 \text{ mT}$  is strong enough to suppress the weak hyperfine interaction between the hole spin and the nuclear spins [35], but not sufficient to protect the electron spin from fast inhomogeneous dephasing in the fluctuating effective nuclear magnetic field. As a result, the electron spin relaxation is about 4 orders of magnitude faster than the hole spin relaxation. The overall spin relaxation rate of the optically driven hole spin is therefore strongly increased compared to the hole spin in thermal equilibrium due to the fast decay of the corresponding electron spin in the excited state. This poses a challenge in view of potential applications that depend on spin information.

The presented investigation of the nonequilibrium spin relaxation rate as a function of laser detuning and intensity also enabled the characterization of the optical transition by determining the intrinsic linewidth and the saturation intensity. Furthermore, the inho-

homogeneous broadening of the optical transition was precisely determined from the detuning dependence of the SN power. In the absence of inhomogeneous broadening, the SN power drops to zero at the resonance due to the dispersion of the optical transition. Small inhomogeneous broadening results in a finite value of the SN power at the resonance, while strong inhomogeneous broadening leads to a Gaussian line shape of the SN power with a maximum at the resonance. On the present sample, the inhomogeneous broadening caused by charge noise in the QD environment was found to be very strong for moderate QD densities [35]. The measurements in this thesis have been conducted in a region of very low QD density which significantly reduced the typically large inhomogeneous broadening of the optical transition to the same order of magnitude as the homogeneous linewidth. Remarkably, even a QD transition with completely negligible inhomogeneous broadening was observed. The strong reduction of the inhomogeneous broadening at low QD densities might be explained by the smaller number of ionized acceptors in the QD environment as a result of the smaller number of QDs which trap the acceptor holes. Thus, the smaller number of potentially charge-binding defects in the environment reduces the charge fluctuations which are responsible for the inhomogeneous broadening. The observation of completely negligible inhomogeneous broadening demonstrates the high purity of the low-doped GaAs environment in the studied structure. This is an encouraging result in view of optical applications for the studied QD system.

The nonequilibrium spin fluctuations furthermore revealed a new noise contribution beyond the spin dynamics, which was observed via SNS for the first time. Theoretical modeling of the laser-detuning and magnetic-field dependent measurements showed that this nonequilibrium contribution is related to fluctuations of the QD occupation by the resident hole. The escape of the hole from the QD is initiated by nonradiative Auger recombination and quenches the SN signal until a new hole with an arbitrary spin is provided to the QD by its environment. The correlation time observed in the occupation noise spectrum is determined by the probability of Auger recombination and by the charge dynamics in the environment that define



---

the periods during which the QD is unoccupied. Measurements as a function of laser detuning and intensity enabled the determination of the intrinsic Auger rate of holes in InAs QDs to be about 2 to  $3 \mu\text{s}^{-1}$ . The reoccupation of the QDs was found to be relatively slow, i.e., on the order of several microseconds in the high-quality, low-doped sample. Moreover, it was shown that the presence of an ionized acceptor in the close vicinity of a QD can further increase the reoccupation time to several tens of microseconds. In this case, the ionized acceptor competes with the QD in capturing a hole while Coulomb repulsion suppresses hole occupation of acceptor and QD at the same time. This results in a strong reduction of the average QD occupation such that the resonantly driven QD does not host a spin for more than 50% of the time. Thus, the occupation noise of the optically driven QD spin system constitutes a strong parasitic effect causing dead times in potential quantum-information devices which rely on the spin-photon interface. In fact, the Auger recombination is intrinsic to the spin-photon interaction and can hardly be avoided in semiconductor nanostructures. This in turn poses a second important challenge for future applications.

The challenges identified above can be addressed in future studies. Regarding the first challenge of fast excited state spin relaxation, it can be expected that the application of higher magnetic fields on the order of 1 T will suppress the efficient hyperfine interaction of the electron spin and thus restores small spin relaxation rates in the presence of optical driving. A new confocal microscope setup which enables the application of longitudinal magnetic fields up to 2 T has been built and will enable to study the limitations of the spin relaxation time of electrons and holes beyond the hyperfine interaction.

A possibility to mitigate the detrimental effect of Auger recombination in future applications is the implementation of fast QD recharging times. Fast recharging can be realized by embedding the QDs in a field-effect structure that comprises a charge reservoir [135, 136]. In contrast to the slow stochastic recharging in low-doped samples, this enables deterministic recharging of the QDs through a bias-controllable tunneling barrier. However, care must

be taken, since small tunnel barriers which enable fast recharging are accompanied by a degradation of the QD spin lifetime as a result of co-tunneling effects [63]. Potential devices therefore have to be carefully balanced in order to enable reasonable recharging times while still maintaining long spin lifetimes.

In view of future experiments further changes to the experimental setup are conceivable to improve the SNS method. The presented results – in a row with several other recent publications [35, 75, 99, 115, 127, 137–139] – clearly show that SNS is a powerful tool to study spin dynamics, spin interactions, and optical properties of semiconductor nanostructures under various conditions. However, the Faraday rotation signal due to spin fluctuations is typically small and strongly overlaid by photon shot noise of the laser and electronic noise of the detection process. The presence of these strong extrinsic noise sources necessitates long measurement times to acquire SN spectra with a good signal-to-noise ratio and even impedes measurements at extremely low light intensities or of high-frequency single spin dynamics. The single QD SN measurements are typically significantly dominated by electronic noise (see Fig. 3.5). A way to reduce the impact of the electronic noise is optical amplification of the SN signal via homodyne detection [140, 141]. In this technique, the low-intensity SN probe laser interferes with a phase-stabilized high-intensity local oscillator. Constructive interference increases the detected intensity difference at the balanced receiver which originates from the small Faraday rotation angle. As a result, the SN signal is increased relative to the electronic noise as a function of the local-oscillator intensity. An increase of the SN signal-to-noise ratio has been demonstrated for electron spins in bulk GaAs with a heterodyne [142] and a homodyne [143] detection scheme for spin noise signals at high frequencies. However, the QD SN measurements in a longitudinal magnetic field require an amplification scheme which is applicable for noise frequencies close to zero frequency. For this reason, a SNS homodyne amplification scheme working at low detection frequencies has already been designed and tested in a proof-of-principle measurement on Rubidium vapor [144]. In a next step, this homodyne amplification scheme can be transferred to the single

---

QD SN measurements. This improvement on the noise limitation of the SNS method enhances the capabilities of the SN measurements and will facilitate the characterization of advanced semiconductor nanostructure devices.



# Appendices



# A. Additional Information on the Sample

This supplement presents broadband reflectivity and PL measurements of the investigated QD sample. The measurements have been performed by the PTB in Braunschweig after the sample growth [104]. They provide the basis for the sample characterization in section 3.1.

Figure A.1 shows reflectivity and PL measurements in growth direction which corresponds to the measurement direction  $z$  in this thesis. The measurements are conducted on a wafer segment with low QD density with a high PL excitation power. PL and reflectivity spectra in growth direction are determined by the properties of the microcavity and reveal the center and the width of the cavity resonance at 8 K as well as at 300 K.

The PL measurements presented in Fig. A.2 are conducted from the side of the wafer, perpendicular to the cavity, in order to investigate the QD density and energy distribution at different wafer positions along the density gradient. The graphs are shown in ascending order regarding the QD density. The energy distribution of the QD ensemble is in general much broader than the width of the microcavity (cf. Fig. A.1). At lower QD densities a small shift of the QD distribution to higher photon energies is observed.

A. Additional Information on the Sample

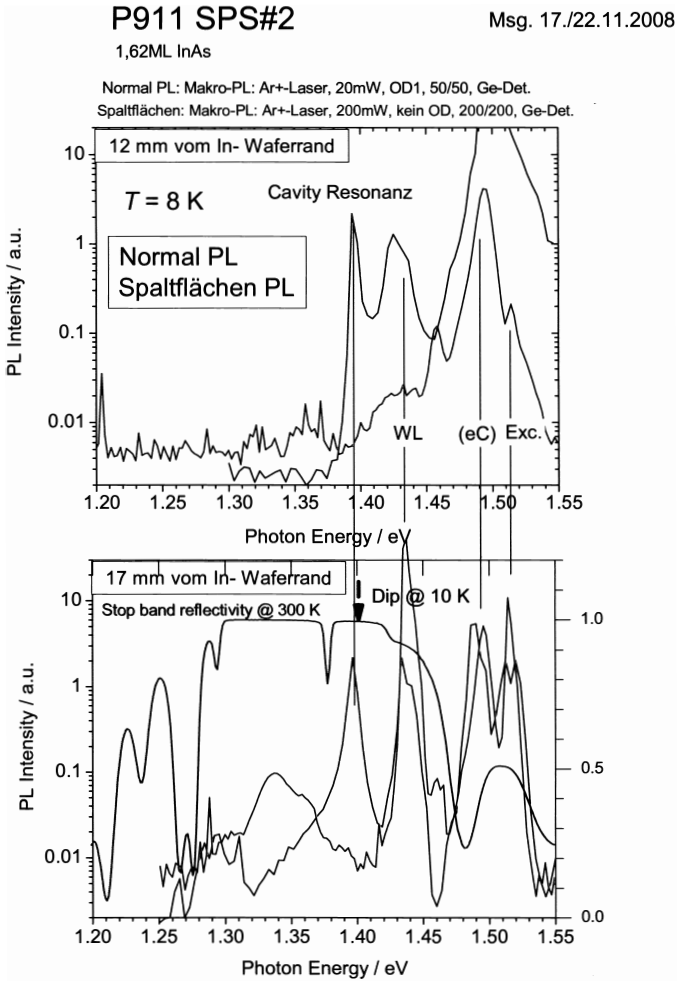


Figure A.1.: Investigation of the microcavity (see text).



## P911 SPS#2

Makro-PL: Ar+-Laser, 200mW, kein OD, 200/200, Ge-Det.

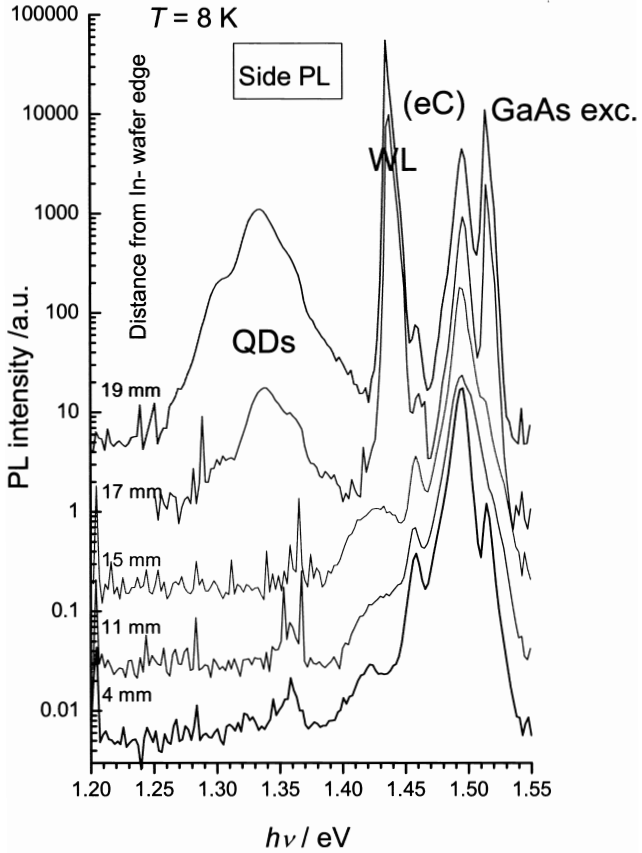


Figure A.2.: Investigation of the QDs at different densities (see text).



## B. Alternative Models of Charge Dynamics

This supplementary section presents the results of two variations of the theoretical model which has been used to describe the Kerr rotation noise measurements presented in Sec. 4.2. The alternative models are only slightly different from the model presented in the main text. However, their resulting calculated Kerr rotation noise spectra show clear deviations from the measured spectra, as will be shown in the following.

The states of the QD and the considered hole states in the QD environment are the same for all models. They are depicted in Fig. B.1(a) together with the relevant transitions and their corresponding rates. Auger recombination with a rate  $\gamma_A$  describes the escape of the hole from the QD. The QD can be recharged from the continuum with a rate  $\gamma_{C,D}$ . At the same time, an ionized acceptor, represented as the outer state, can be charged from the continuum with a rate  $\gamma_{C,O}$ . A hole in the outer state can tunnel into the QD with a rate  $\gamma_{O,D}$ . In the main text it was assumed that Coulomb repulsion prohibits the simultaneous occupation of QD and outer state. In the first alternative model, this assumption is released such that the QD can be charged from the continuum independent of the charge status of the outer state. Fig. B.1(b) shows the resulting calculated Kerr rotation noise spectrum together with the measured spectrum at a laser detuning of  $\Delta = 1 \mu\text{eV}$ . The parameters used to calculate the noise spectrum are summarized in Tab. B.1. They are equivalent to the parameters derived in the main text. In particular, the rates from the continuum into the outer state and from the outer state into the QD are by an order of magnitude smaller than the direct recharging rate from the continuum into the QD.

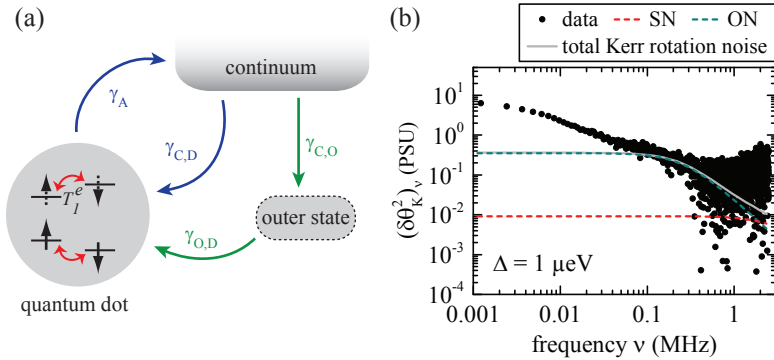


Figure B.1.: (a) Sketch of the QD states and of the hole states in the QD environment. The arrows illustrate all relevant transitions considered for the theoretical model. (b) Measured Kerr rotation noise spectrum at a small laser detuning of  $1 \mu\text{eV}$  and the corresponding calculated Kerr rotation noise spectrum [composed of spin noise (SN) and occupation noise (ON)]. The calculation assumes no Coulomb repulsion between QD and acceptor. This model can not reproduce the low-frequency component of the measured ON spectrum related to the outer-state tunneling. The parameters used for the calculation are summarized in Tab. B.1.

Nevertheless, the calculated occupation noise spectrum (ON) does not show a significant additional contribution at low frequencies, which is in strong contradiction with the measured Kerr rotation noise spectrum. The absence of the low-frequency noise can be explained by the absent blocking of the QD recharging process for a charged outer state in contrast to the Coulomb-repulsion model used in Sec. 4.2. In the model without Coulomb repulsion (Fig. B.1) the QD can always be charged from the continuum with the higher rate  $\gamma_{C,D}$ , even if the outer state is charged. This situation leads to the absence of the occasionally long unoccupied periods of the QD which occur in the model that assumed Coulomb repulsion between

---

physical quantity	symbol	value
trion linewidth	$\gamma_I$	4.3 $\mu\text{eV}$
effective Zeeman splitting at 31 mT	$\hbar\Omega_z$	5.2 $\mu\text{eV}$
electron spin relaxation time	$T_1^e$	24 ns
Auger recombination rate	$\gamma_A$	2.0 $\mu\text{s}^{-1}$
QD reoccupation rate from continuum	$\gamma_{C,D}$	0.7 $\mu\text{s}^{-1}$
outer-state reoccupation rate from cont.	$\gamma_{C,O}$	0.06 $\mu\text{s}^{-1}$
QD reoccupation rate from outer state	$\gamma_{O,D}$	0.03 $\mu\text{s}^{-1}$

Table B.1.: Parameters of spin and charge dynamics for the calculations based on the model without Coulomb repulsion.

QD and outer state. As a result, the QD occupation noise in the absence of Coulomb repulsion is governed by the fast recharging of the QD from the continuum while the rare slow recharging events via the outer state barely influence the average reoccupation time of the QD. For this reason, the model of charge dynamics without Coulomb repulsion between QD and outer state can not describe the observed data.

In order to model the additional low-frequency component of the ON spectrum, it is necessary that the charging of the outer state significantly changes the average QD occupation compared to the situation with an empty outer state. On the one hand, this can be realized assuming Coulomb repulsion which prevents the charging of the QD in the case of a charged outer state, but there is a second possible scenario: we assume that the QD and the outer state can be charged at the same time, but the charging of the outer state leads to a significant Stark shift of the QD resonance since the additional charge in the QD vicinity changes the electric field at the QD position. A positive charge trapped by a nearby ionized acceptor can cause a Stark shift of the trion resonance which is on the order of 10  $\mu\text{eV}$  [64]. Such a shift of the the trion resonance changes the detuning between the trion transition and the laser energy, which in turn changes the population of the trion state. The population of the trion state determines the probability of an Auger process:

in the case of a large laser detuning, the relative population of the trion state is small and the effective Auger rate  $\tilde{\gamma}_A \propto n_{\text{tr}}/n \cdot \gamma_A$  becomes small. On the other hand, a small laser detuning yields a relatively large population of the trion state and a much higher effective Auger rate. Hence, a theoretical model which includes a Stark shift of the trion resonance for a charged outer state can yield low-frequency occupation noise as a result of a temporarily strongly reduced effective Auger rate. Fig. B.2 shows the calculated Kerr rotation noise spectrum based on the Stark-shift model, again for a laser detuning of  $\Delta = 1 \mu\text{eV}$ . The parameters used for the calculation are summarized in Tab. B.2. The intrinsic Auger rate and the transition rates to QD and outer state have again similar values as in Sec. 4.2. For a charged outer state, a trion resonance shift of  $\Delta_2 = 17 \mu\text{eV}$  is assumed. This resonance shift is large compared to the trion linewidth of  $\gamma_I = 7 \mu\text{eV}$  such that an initially resonant laser ( $\Delta_1 = 0$ ) becomes nearly off-resonant with the shifted trion transition in the case of a charged outer state. This results in a very low effective Auger rate,  $\tilde{\gamma}_{A,2} \ll \tilde{\gamma}_{A,1}$ , until the hole from the outer state tunnels into the QD, which shifts the trion resonance back to  $\Delta_1$  where Auger recombination empties the QD efficiently. As can be seen for the calculated Kerr rotation noise spectrum shown in Fig. B.2, this model indeed yields a strong additional ON component at low noise frequencies which is related to long occupied periods of the QD in the case of a charged outer state. As a result, the calculated Kerr rotation noise spectrum can qualitatively reproduce the measured noise spectrum at the small laser detuning (with respect to the unshifted trion resonance). However, the temporary shift of the trion resonance has a strong impact on the detuning dependence of the SN and ON power. The calculated average noise power of SN and ON contribution as a function of the laser detuning is shown by the solid lines in Fig. B.3. The parameters used for the calculation are again the parameters summarized in Tab. B.2. Fig. B.3 shows that a temporary shift of the trion resonance theoretically results in an additional ON power maximum centered at the Stark-shifted trion resonance at  $\Delta_2 = 17 \mu\text{eV}$ . Furthermore, the SN power spectrum is significantly modified by the

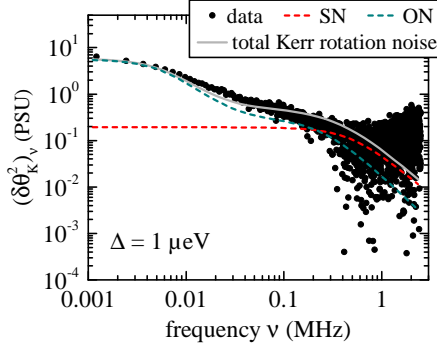


Figure B.2.: Measured Kerr rotation noise spectrum at a small laser detuning of  $1 \mu\text{eV}$  and the corresponding calculated Kerr rotation noise spectrum for assuming a Stark shift of the **QD** resonance depending on the charge status of the outer state. A temporary **QD** resonance shift lowers the effective Auger rate  $\tilde{\gamma}_A$  and leads to a low-frequency component in the calculated **ON** spectrum, reproducing the measured spectrum. The parameters used for the calculation are summarized in Tab. B.2.

physical quantity	symbol	value
trion linewidth	$\gamma_I$	$7 \mu\text{eV}$
Stark-shift for a charged outer state	$\Delta_2$	$17 \mu\text{eV}$
effective Zeeman splitting at 31 mT	$\hbar\Omega_z$	$8 \mu\text{eV}$
electron spin relaxation time	$T_1^e$	$24 \text{ ns}$
Auger recombination rate	$\gamma_A$	$2.0 \mu\text{s}^{-1}$
<b>QD</b> reoccupation rate from continuum	$\gamma_{C,D}$	$0.6 \mu\text{s}^{-1}$
outer-state reoccupation rate from cont.	$\gamma_{C,O}$	$0.02 \mu\text{s}^{-1}$
<b>QD</b> reoccupation rate from outer state	$\gamma_{O,D}$	$0.03 \mu\text{s}^{-1}$

Table B.2.: Parameters of spin and charge dynamics for the calculations with the Stark-shift model.

temporary resonance shift compared to the typical single-resonance spectrum with a vanishing SN noise power at the resonance and two equal SN power maxima at positive and negative detunings. The occasional shift of the trion resonance to higher energy leads to an asymmetric average SN spectrum, with a decreased SN power maximum at the low energy site (negative laser detuning) and a finite noise power at the initial trion resonance. In addition, a third small SN power maximum related to the Stark-shifted trion transition appears at higher energies. In contrast, the measured power spectrum of both, SN and ON contribution (shown by the dots and squares in Fig. B.3), are symmetric around zero laser detuning. Hence, the Stark-shift model can also not describe the measured QD Kerr rotation noise correctly. The best agreement between measured and calculated Kerr rotation noise is obtained assuming Coulomb repulsion between QD and outer state, as presented in Sec. 4.2. The finite value of the measured SN power at zero detuning and the broadening of the ON power spectrum (cf. Fig. B.3) can be captured in the Coulomb-repulsion model by assuming small Stark-shifts of the trion resonance equally distributed around zero detuning. The small resonance shifts can be caused by charge fluctuations in the wider QD environment as described in the main text in Sec. 4.2.



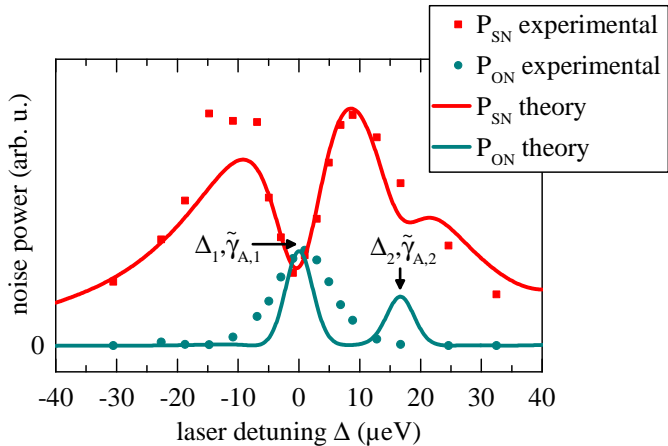


Figure B.3.: The measured SN and ON power as a function of the laser detuning and the calculated noise power spectra for assuming a Stark shift of the QD resonance depending on the charge status of the outer state. A temporary QD resonance shift of  $\Delta_2 = 17 \mu\text{eV}$  alters the effective Auger rate  $\tilde{\gamma}_A$  and results in an additional ON power maximum. Additionally, the resonance shift leads to an asymmetric SN power spectrum. In contrast, the measured noise power spectra (dots and squares) are symmetric around  $\Delta = 0$ . The parameters used for the calculation are summarized in Tab. B.2.



# Bibliography

- [1] C. H. Bennett and D. P. DiVincenzo, “Quantum information and computation”, *Nature* **404**, 247 (2000).
- [2] P. Shor, “Polynomial-Time Algorithms for Prime Factorization and Discrete Logarithms on a Quantum Computer”, *SIAM Review* **41**, 303 (1999).
- [3] S. Ritter, C. Nölleke, C. Hahn, A. Reiserer, A. Neuzner, M. Uphoff, M. Mücke, E. Figueroa, J. Bochmann, and G. Rempe, “An elementary quantum network of single atoms in optical cavities”, *Nature* **484**, 195 (2012).
- [4] E. A. Martinez, C. A. Muschik, P. Schindler, D. Nigg, A. Erhard, M. Heyl, P. Hauke, M. Dalmonte, T. Monz, P. Zoller, and R. Blatt, “Real-time dynamics of lattice gauge theories with a few-qubit quantum computer”, *Nature* **534**, 516 (2016).
- [5] M. Saffman, “Quantum computing with atomic qubits and Rydberg interactions: progress and challenges”, *Journal of Physics B: Atomic, Molecular and Optical Physics* **49**, 202001 (2016).
- [6] S. Debnath, N. M. Linke, C. Figgatt, K. A. Landsman, K. Wright, and C. Monroe, “Demonstration of a small programmable quantum computer with atomic qubits”, *Nature* **536**, 63 (2016).
- [7] H. Bernien, S. Schwartz, A. Keesling, H. Levine, A. Omran, H. Pichler, S. Choi, A. S. Zibrov, M. Endres, M. Greiner,

- V. Vuletic, and M. D. Lukin, “Probing many-body dynamics on a 51-atom quantum simulator”, *Nature* **551**, 579 (2017).
- [8] M. Saffman, “Quantum computing with neutral atoms”, *National Science Review* , nwy088 (2018).
- [9] P. Michler, A. Imamoglu, M. D. Mason, P. J. Carson, G. F. Strouse, and S. K. Buratto, “Quantum correlation among photons from a single quantum dot at room temperature”, *Nature* **406**, 968 (2000).
- [10] V. Zwiller, H. Blom, P. Jonsson, N. Panev, S. Jeppesen, T. Tsegaye, E. Goobar, M.-E. Pistol, L. Samuelson, and G. Björk, “Single quantum dots emit single photons at a time: Antibunching experiments”, *Appl. Phys. Lett.* **78**, 2476 (2001).
- [11] H. Kamada, H. Gotoh, J. Temmyo, T. Takagahara, and H. Ando, “Exciton Rabi Oscillation in a Single Quantum Dot”, *Phys. Rev. Lett.* **87**, 246401 (2001).
- [12] X. Xu, B. Sun, P. R. Berman, D. G. Steel, A. S. Bracker, D. Gammon, and L. J. Sham, “Coherent Optical Spectroscopy of a Strongly Driven Quantum Dot”, *Science* **317**, 929 (2007).
- [13] E. B. Flagg, A. Muller, J. W. Robertson, S. Founta, D. G. Deppe, M. Xiao, W. Ma, G. J. Salamo, and C. K. Shih, “Resonantly driven coherent oscillations in a solid-state quantum emitter”, *Nature Physics* **5**, 203 (2009).
- [14] M. Benyoucef, M. Yacob, J. P. Reithmaier, J. Kettler, and P. Michler, “Telecom-wavelength (1.5  $\mu\text{m}$ ) single-photon emission from InP-based quantum dots”, *Appl. Phys. Lett.* **103**, 162101 (2013).
- [15] M. Paul, F. Olbrich, J. Höschel, S. Schreier, J. Kettler, S. L. Portalupi, M. Jetter, and P. Michler, “Single-photon emission

- at 1.55  $\mu\text{m}$  from MOVPE-grown InAs quantum dots on InGaAs/GaAs metamorphic buffers”, *Appl. Phys. Lett.* **111**, 033102 (2017).
- [16] M. Atatüre, J. Dreiser, A. Badolato, A. Högele, K. Karrai, and A. Imamoglu, “Quantum-dot spin-state preparation with near-unity fidelity.”, *Science* **312**, 551 (2006).
- [17] X. Xu, Y. Wu, B. Sun, Q. Huang, J. Cheng, D. G. Steel, A. S. Bracker, D. Gammon, C. Emary, and L. J. Sham, “Fast Spin State Initialization in a Singly Charged InAs-GaAs Quantum Dot by Optical Cooling”, *Phys. Rev. Lett.* **99**, 097401 (2007).
- [18] M. Atatüre, J. Dreiser, A. Badolato, and A. Imamoglu, “Observation of Faraday rotation from a single confined spin”, *Nature Physics* **3**, 101 (2007).
- [19] J. Berezovsky, M. H. Mikkelsen, N. G. Stoltz, L. A. Coldren, and D. D. Awschalom, “Picosecond Coherent Optical Manipulation of a Single Electron Spin in a Quantum Dot”, *Science* **320**, 349 (2008).
- [20] D. Press, T. D. Ladd, B. Zhang, and Y. Yamamoto, “Complete quantum control of a single quantum dot spin using ultrafast optical pulses”, *Nature* **456**, 218 (2008).
- [21] D. P. DiVincenzo, “The Physical Implementation of Quantum Computation”, *Fortschritte der Physik* **48**, 771 (2000).
- [22] B. Urbaszek, X. Marie, T. Amand, O. Krebs, P. Voisin, P. Maletinsky, A. Högele, and A. Imamoglu, “Nuclear spin physics in quantum dots: An optical investigation”, *Rev. Mod. Phys.* **85**, 79 (2013).
- [23] I. A. Merkulov, A. L. Efros, and M. Rosen, “Electron spin relaxation by nuclei in semiconductor quantum dots”, *Phys. Rev. B* **65**, 205309 (2002).

- [24] D. Brunner, B. D. Gerardot, P. A. Dalgarno, G. Wüst, K. Karrai, N. G. Stoltz, P. M. Petroff, and R. J. Warburton, “A Coherent Single-Hole Spin in a Semiconductor”, *Science* **325**, 70 (2009).
- [25] B. Eble, C. Testelin, P. Desfonds, F. Bernardot, A. Balocchi, T. Amand, A. Miard, A. Lemaître, X. Marie, and M. Chamarro, “Hole–Nuclear Spin Interaction in Quantum Dots”, *Phys. Rev. Lett.* **102**, 146601 (2009).
- [26] R. J. Warburton, “Single spins in self-assembled quantum dots”, *Nature Materials* **12**, 483 (2013).
- [27] A. V. Kuhlmann, J. Houel, A. Ludwig, L. Greuter, D. Reuter, A. D. Wieck, M. Poggio, and R. J. Warburton, “Charge noise and spin noise in a semiconductor quantum device”, *Nature Physics* **9**, 570 (2013).
- [28] A. Kurzmann, A. Ludwig, A. D. Wieck, A. Lorke, and M. Geller, “Auger Recombination in Self-Assembled Quantum Dots: Quenching and Broadening of the Charged Exciton Transition”, *Nano Letters* **16**, 3367 (2016).
- [29] E. B. Aleksandrov and V. S. Zapasskii, “Magnetic resonance in the Faraday-rotation noise spectrum”, *Zh. Eksp. Teor. Fiz* **81**, 132 (1981).
- [30] S. A. Crooker, D. G. Rickel, A. V. Balatsky, and D. L. Smith, “Spectroscopy of spontaneous spin noise as a probe of spin dynamics and magnetic resonance”, *Nature* **431**, 49 (2004).
- [31] M. Oestreich, M. Römer, R. J. Haug, and D. Hägele, “Spin Noise Spectroscopy in GaAs”, *Phys. Rev. Lett.* **95**, 216603 (2005).
- [32] V. S. Zapasskii, “Spin-noise spectroscopy: from proof of principle to applications”, *Adv. Opt. Photonics* **5**, 131 (2013).

- [33] J. Hübner, F. Berski, R. Dahbashi, and M. Oestreich, “The rise of spin noise spectroscopy in semiconductors: From acoustic to GHz frequencies”, *Phys. Status Solidi B* **251**, 1824 (2014).
- [34] M. Römer, J. Hübner, and M. Oestreich, “Spin noise spectroscopy in semiconductors”, *Rev. Sci. Instrum.* **78**, 103903 (2007).
- [35] R. Dahbashi, J. Hübner, F. Berski, K. Pierz, and M. Oestreich, “Optical Spin Noise of a Single Hole Spin Localized in an (InGa)As Quantum Dot”, *Phys. Rev. Lett.* **112**, 156601 (2014).
- [36] N. A. Sinitsyn and Y. V. Pershin, “The theory of spin noise spectroscopy: a review”, *Reports on Progress in Physics* **79**, 106501 (2016).
- [37] P. Michler, editor, *Quantum Dots for Quantum Information Technologies*, Springer International Publishing, 2017.
- [38] V. I. Klimov, editor, *Nanocrystal Quantum Dots*, CRC Press, 2010.
- [39] R. Keil, M. Zopf, Y. Chen, B. Höfer, J. Zhang, F. Ding, and O. G. Schmidt, “Solid-state ensemble of highly entangled photon sources at rubidium atomic transitions”, *Nature Communications* **8**, 15501 (2017).
- [40] R. Hanson, L. P. Kouwenhoven, J. R. Petta, S. Tarucha, and L. M. K. Vandersypen, “Spins in few-electron quantum dots”, *Rev. Mod. Phys.* **79**, 1217 (2007).
- [41] I. N. Stranski and L. Krastanow, “Zur Theorie der orientierten Ausscheidung von Ionenkristallen aufeinander”, *Monatshefte für Chemie* **71**, 351 (1938).
- [42] D. Leonard, M. Krishnamurthy, C. M. Reaves, S. P. Denbaars, and P. M. Petroff, “Direct formation of quantum-sized dots

- from uniform coherent islands of InGaAs on GaAs surfaces”, *Appl. Phys. Lett.* **63**, 3203 (1993).
- [43] C. Klingshirn, *Semiconductor Optics*, Springer-Verlag Berlin Heidelberg, 2007.
- [44] O. Gywat, H. J. Krenner, and J. Berezovsky, *Spins in Optically Active Quantum Dots*, Wiley-VCH, 2010.
- [45] A. Tartakovskii, editor, *Quantum Dots: Optics, Electron Transport and Future Applications*, Cambridge University Press, 2012.
- [46] M. Fox, *Optical Properties of Solids*, Oxford University Press, 2010.
- [47] D. Bimberg, M. Grundmann, and N. N. Ledentsov, *Quantum Dot Heterostructures*, Wiley, 1999.
- [48] O. Stier, M. Grundmann, and D. Bimberg, “Electronic and optical properties of strained quantum dots modeled by 8-band k-p theory”, *Phys. Rev. B* **59**, 5688 (1999).
- [49] D. I. Lubyshv, P. P. González-Borrero, E. Marega, E. Petitprez, N. La Scala, and P. Basmaji, “Exciton localization and temperature stability in self-organized InAs quantum dots”, *Appl. Phys. Lett.* **68**, 205 (1996).
- [50] M. Bayer, G. Ortner, O. Stern, A. Kuther, A. A. Gorbunov, A. Forchel, P. Hawrylak, S. Fafard, K. Hinzer, T. L. Reinecke, S. N. Walck, J. P. Reithmaier, F. Klopff, and F. Schäfer, “Fine structure of neutral and charged excitons in self-assembled In(Ga)As/(Al)GaAs quantum dots”, *Phys. Rev. B* **65**, 195315 (2002).
- [51] R. Seguin, A. Schliwa, S. Rodt, K. Pötschke, U. W. Pohl, and D. Bimberg, “Size-Dependent Fine-Structure Splitting in Self-Organized InAs/GaAs Quantum Dots”, *Phys. Rev. Lett.* **95**, 257402 (2005).



- [52] J. Zhang, J. S. Wildmann, F. Ding, R. Trotta, Y. Huo, E. Zallo, D. Huber, A. Rastelli, and O. G. Schmidt, “High yield and ultrafast sources of electrically triggered entangled-photon pairs based on strain-tunable quantum dots”, *Nature Communications* **6**, 10067 (2015).
- [53] B. D. Gerardot, D. Brunner, P. A. Dalgarno, P. Öhberg, S. Seidl, M. Kroner, K. Karrai, N. G. Stoltz, P. M. Petroff, and R. J. Warburton, “Optical pumping of a single hole spin in a quantum dot”, *Nature* **451**, 441 (2008).
- [54] J. Hansom, C. H. H. Schulte, C. Le Gall, C. Matthiesen, E. Clarke, M. Hugues, J. M. Taylor, and M. Atatüre, “Environment-assisted quantum control of a solid-state spin via coherent dark states”, *Nature Physics* **10**, 725 (2014).
- [55] Z. Sun, A. Delteil, S. Faelt, and A. Imamoglu, “Measurement of spin coherence using Raman scattering”, *Phys. Rev. B* **93**, 241302 (2016).
- [56] P. Auger, “Sur les rayons  $\beta$  secondaires produits dans un gaz par des rayons X”, *C.R.A.S.* **177**, 169 (1923).
- [57] I. Pelant and J. Valenta, *Luminescence Spectroscopy of Semiconductors*, Oxford University Press, 2012.
- [58] W. Demtröder, *Experimental Physik 3: Atome, Moleküle und Festkörper*, Springer-Verlag Berlin Heidelberg, 2005.
- [59] M. Nirmal, B. O. Dabbousi, M. G. Bawendi, J. J. Macklin, J. K. Trautman, T. D. Harris, and L. E. Brus, “Fluorescence intermittency in single cadmium selenide nanocrystals”, *Nature* **383**, 802 (1996).
- [60] A. L. Efros and M. Rosen, “Random Telegraph Signal in the Photoluminescence Intensity of a Single Quantum Dot”, *Phys. Rev. Lett.* **78**, 1110 (1997).

- [61] R. Vaxenburg, A. Rodina, A. Shabaev, E. Lifshitz, and A. L. Efros, “Nonradiative Auger Recombination in Semiconductor Nanocrystals”, *Nano Letters* **15**, 2092 (2015).
- [62] V. I. Klimov, A. A. Mikhailovsky, D. W. McBranch, C. A. Leatherdale, and M. G. Bawendi, “Quantization of Multiparticle Auger Rates in Semiconductor Quantum Dots”, *Science* **287**, 1011 (2000).
- [63] J. Dreiser, M. Atatüre, C. Galland, T. Müller, A. Badolato, and A. Imamoglu, “Optical investigations of quantum dot spin dynamics as a function of external electric and magnetic fields”, *Phys. Rev. B* **77**, 075317 (2008).
- [64] J. Houel, A. V. Kuhlmann, L. Greuter, F. Xue, M. Poggio, B. D. Gerardot, P. A. Dalgarno, A. Badolato, P. M. Petroff, A. Ludwig, D. Reuter, A. D. Wieck, and R. J. Warburton, “Probing Single-Charge Fluctuations at a GaAs / AlAs Interface Using Laser Spectroscopy on a Nearby InGaAs Quantum Dot”, *Phys. Rev. Lett.* **108**, 107401 (2012).
- [65] J. Wiegand, D. S. Smirnov, J. Osberghaus, L. Abaspour, J. Hübner, and M. Oestreich, “Hole-capture competition between a single quantum dot and an ionized acceptor”, *Phys. Rev. B* **98**, 125426 (2018).
- [66] J. H. Rice, J. W. Robinson, A. Jarjour, R. A. Taylor, R. A. Oliver, G. A. D. Briggs, M. J. Kappers, and C. J. Humphreys, “Temporal variation in photoluminescence from single InGaN quantum dots”, *Appl. Phys. Lett.* **84**, 4110 (2004).
- [67] A. Högele, S. Seidl, M. Kroner, K. Karrai, R. J. Warburton, B. D. Gerardot, and P. M. Petroff, “Voltage-Controlled Optics of a Quantum Dot”, *Phys. Rev. Lett.* **93**, 217401 (2004).
- [68] F. Bloch, “Nuclear Induction”, *Phys. Rev.* **70**, 460 (1946).
- [69] R. Loudon, *The Quantum Theory of Light*, Oxford University Press, 2000.

- [70] I. Žutić, J. Fabian, and S. Das Sarma, “Spintronics: Fundamentals and applications”, *Rev. Mod. Phys.* **76**, 323 (2004).
- [71] M. I. Dyakonov and V. I. Perel, “Spin relaxation of conduction band electrons in noncentrosymmetric semiconductors”, *Sov. Phys. Solid State* **13**, 3023 (1972).
- [72] R. J. Elliott, “Theory of the Effect of Spin-Orbit Coupling on Magnetic Resonance in Some Semiconductors”, *Phys. Rev.* **96**, 266 (1954).
- [73] Y. Yafet, “g Factors and Spin-Lattice Relaxation of Conduction Electrons”, volume 14 of *Solid State Physics*, pages 1 – 98, Academic Press, 1963.
- [74] G. L. Bir, A. G. Aronov, and G. E. Pikus, “Spin relaxation of electrons due to scattering by holes”, *JETP* **42**, 705 (1976).
- [75] F. Berski, J. Hübner, M. Oestreich, A. Ludwig, A. D. Wieck, and M. Glazov, “Interplay of Electron and Nuclear Spin Noise in n-Type GaAs”, *Phys. Rev. Lett.* **115**, 176601 (2015).
- [76] M. Paillard, X. Marie, P. Renucci, T. Amand, A. Jbeli, and J. M. Gérard, “Spin Relaxation Quenching in Semiconductor Quantum Dots”, *Phys. Rev. Lett.* **86**, 1634 (2001).
- [77] A. Abragam, *The Principles of Nuclear Magnetism*, Oxford University Press, 1961.
- [78] J. H. Prechtel, A. V. Kuhlmann, J. Houel, A. Ludwig, S. R. Valentin, A. D. Wieck, and R. J. Warburton, “Decoupling a hole spin qubit from the nuclear spins”, *Nature Materials* **15**, 981 (2016).
- [79] P.-F. Braun, X. Marie, L. Lombez, B. Urbaszek, T. Amand, P. Renucci, V. K. Kalevich, K. V. Kavokin, O. Krebs, P. Voisin, and Y. Masumoto, “Direct Observation of the Electron Spin Relaxation Induced by Nuclei in Quantum Dots”, *Phys. Rev. Lett.* **94**, 116601 (2005).

- [80] R. Dahbashi, “Spinrauschen in nulldimensionalen Strukturen”, PhD thesis, Leibniz Universität Hannover, 2015.
- [81] J. Fischer, W. A. Coish, D. V. Bulaev, and D. Loss, “Spin decoherence of a heavy hole coupled to nuclear spins in a quantum dot”, *Phys. Rev. B* **78**, 155329 (2008).
- [82] M. Kroutvar, Y. Ducommun, D. Heiss, M. Bichler, D. Schuh, G. Abstreiter, and J. J. Finley, “Optically programmable electron spin memory using semiconductor quantum dots”, *Nature* **432**, 81 (2004).
- [83] L. M. Woods, T. L. Reinecke, and Y. Lyanda-Geller, “Spin relaxation in quantum dots”, *Phys. Rev. B* **66**, 161318 (2002).
- [84] A. V. Khaetskii and Y. V. Nazarov, “Spin-flip transitions between Zeeman sublevels in semiconductor quantum dots”, *Phys. Rev. B* **64**, 125316 (2001).
- [85] D. Heiss, S. Schaeck, H. Huebl, M. Bichler, G. Abstreiter, J. J. Finley, D. V. Bulaev, and D. Loss, “Observation of extremely slow hole spin relaxation in self-assembled quantum dots”, *Phys. Rev. B* **76**, 241306 (2007).
- [86] M. Trif, P. Simon, and D. Loss, “Relaxation of Hole Spins in Quantum Dots via Two-Phonon Processes”, *Phys. Rev. Lett.* **103**, 106601 (2009).
- [87] D. Press, K. De Greve, P. L. McMahon, T. D. Ladd, B. Friess, C. Schneider, M. Kamp, S. Höfing, A. Forchel, and Y. Yamamoto, “Ultrafast optical spin echo in a single quantum dot”, *Nature Photonics* **4**, 367 (2010).
- [88] R. Stockill, C. Le Gall, C. Matthiesen, L. Huthmacher, E. Clarke, M. Hugues, and M. Atatüre, “Quantum dot spin coherence governed by a strained nuclear environment”, *Nature Communications* **7**, 12745 (2016).

- [89] N. A. Sinitsyn, Y. Li, S. A. Crooker, A. Saxena, and D. L. Smith, “Role of Nuclear Quadrupole Coupling on Decoherence and Relaxation of Central Spins in Quantum Dots”, *Phys. Rev. Lett.* **109**, 166605 (2012).
- [90] J. Houel, J. H. Prechtel, A. V. Kuhlmann, D. Brunner, C. E. Kuklewicz, B. D. Gerardot, N. G. Stoltz, P. M. Petroff, and R. J. Warburton, “High Resolution Coherent Population Trapping on a Single Hole Spin in a Semiconductor Quantum Dot”, *Phys. Rev. Lett.* **112**, 107401 (2014).
- [91] A. J. Bennett, M. A. Pooley, Y. Cao, N. Sköld, I. Farrer, D. A. Ritchie, and A. J. Shields, “Voltage tunability of single-spin states in a quantum dot”, *Nature Communications* **4**, 1522 (2013).
- [92] R. Kubo, “The fluctuation-dissipation theorem”, *Reports on Progress in Physics* **29**, 255 (1966).
- [93] J. Hübner, R. Dahbashi, F. Berski, J. Wiegand, H. Kuhn, J. Lonnemann, and M. Oestreich, “Spin noise spectroscopy in semiconductors: from a billion down to single spins”, *Proc. SPIE* **9167**, 91672R (2014).
- [94] N. Wiener, “Generalized harmonic analysis”, *Acta Math.* **55**, 117 (1930).
- [95] A. Khintchine, “Korrelationstheorie der stationären stochastischen Prozesse”, *Mathematische Annalen* **109**, 604 (1934).
- [96] G. M. Müller, M. Oestreich, M. Römer, and J. Hübner, “Semiconductor spin noise spectroscopy: Fundamentals, accomplishments, and challenges”, *Physica E: Low-dimensional Systems and Nanostructures* **43**, 569 (2010).
- [97] M. M. Glazov and E. L. Ivchenko, “Spin noise in quantum dot ensembles”, *Phys. Rev. B* **86**, 115308 (2012).

- [98] Y. Li, N. Sinitsyn, D. L. Smith, D. Reuter, A. D. Wieck, D. R. Yakovlev, M. Bayer, and S. A. Crooker, “Intrinsic Spin Fluctuations Reveal the Dynamical Response Function of Holes Coupled to Nuclear Spin Baths in (In,Ga)As Quantum Dots”, *Phys. Rev. Lett.* **108**, 186603 (2012).
- [99] P. Glasenapp, N. A. Sinitsyn, L. Yang, D. G. Rickel, D. Roy, A. Greilich, M. Bayer, and S. A. Crooker, “Spin Noise Spectroscopy Beyond Thermal Equilibrium and Linear Response”, *Phys. Rev. Lett.* **113**, 156601 (2014).
- [100] D. S. Smirnov, P. Glasenapp, M. Bergen, M. M. Glazov, D. Reuter, A. D. Wieck, M. Bayer, and A. Greilich, “Nonequilibrium spin noise in a quantum dot ensemble”, *Phys. Rev. B* **95**, 241408(R) (2017).
- [101] M. M. Glazov, “Spin fluctuations of nonequilibrium electrons and excitons in semiconductors”, *JETP* **122**, 472 (2016).
- [102] W. Demtröder, *Laserspektroskopie*, Springer-Verlag Berlin Heidelberg, 2007.
- [103] I. A. Yugova, M. M. Glazov, E. L. Ivchenko, and A. L. Efros, “Pump-probe Faraday rotation and ellipticity in an ensemble of singly charged quantum dots”, *Phys. Rev. B* **80**, 104436 (2009).
- [104] K. Pierz, “Informationen zu Probe P911”, 2010.
- [105] C. J. R. Sheppard, “Approximate calculation of the reflection coefficient from a stratified medium”, *Pure and Applied Optics: Journal of the European Optical Society Part A* **4**, 665 (1995).
- [106] A. Kavokin, J. J. Baumberg, G. Malpuech, and F. P. Laussy, *Microcavities*, Oxford University Press, 2007.
- [107] C. Schneider, P. Gold, S. Reitzenstein, S. Höfling, and M. Kamp, “Quantum dot micropillar cavities with quality factors exceeding 250,000”, *Applied Physics B* **122**, 19 (2016).

- [108] E. F. Schubert, *Light-Emitting Diodes*, Cambridge University Press, 2003.
- [109] A. Löffler, J. P. Reithmaier, G. Şek, C. Hofmann, S. Reitzenstein, M. Kamp, and A. Forchel, “Semiconductor quantum dot microcavity pillars with high-quality factors and enlarged dot dimensions”, *Appl. Phys. Lett.* **86**, 111105 (2005).
- [110] D. Sanvitto, A. Daraei, A. Tahraoui, M. Hopkinson, P. W. Fry, D. M. Whittaker, and M. S. Skolnick, “Observation of ultrahigh quality factor in a semiconductor microcavity”, *Appl. Phys. Lett.* **86**, 191109 (2005).
- [111] R. P. Stanley, R. Houdré, U. Oesterle, M. Gailhanou, and M. Ilegems, “Ultrahigh finesse microcavity with distributed Bragg reflectors”, *Appl. Phys. Lett.* **65**, 1883 (1994).
- [112] P. Michler, editor, *Single Semiconductor Quantum Dots*, Nanoscience and Technology, Springer-Verlag Berlin Heidelberg, 2009.
- [113] K. J. Vahala, “Optical microcavities”, *Nature* **424**, 839 (2003).
- [114] C. Arnold, J. Demory, V. Loo, A. Lemâitre, I. Sagnes, M. Glazov, O. Krebs, P. Voisin, P. Senellart, and L. Lanco, “Macroscopic rotation of photon polarization induced by a single spin”, *Nature Communications* **6**, 6236 (2015).
- [115] S. V. Poltavtsev, I. I. Ryzhov, M. M. Glazov, G. G. Kozlov, V. S. Zapasskii, A. V. Kavokin, P. G. Lagoudakis, D. S. Smirnov, and E. L. Ivchenko, “Spin noise spectroscopy of a single quantum well microcavity”, *Phys. Rev. B* **89**, 081304(R) (2014).
- [116] R. Dahbashi, “Spinrauschspektroskopie an Halbleiter-Quantenpunkten”, Master’s thesis, Leibniz Universität Hannover, 2011.

- [117] R. Dahbashi, “Konstruktion eines Tieftemperaturmessplatzes und Aufbau eines Diodenlasers zur Vermessung von Halbleiternanostrukturen”, Bachelor’s thesis, Leibniz Universität Hannover, 2009.
- [118] I. Schwartz, E. R. Schmidgall, L. Gantz, D. Cogan, E. Bordo, Y. Don, M. Zielinski, and D. Gershoni, “Deterministic Writing and Control of the Dark Exciton Spin Using Single Short Optical Pulses”, *Phys. Rev. X* **5**, 011009 (2015).
- [119] J. Wiegand, “Photolumineszenz und Spinrauschspektroskopie an selbstorganisierten InAs Quantenpunkten”, Bachelor’s thesis, Leibniz Universität Hannover, 2011.
- [120] A. P. Frauendorf, “Spinrauschspektroskopie an künstlichen Atomen”, Bachelor’s thesis, Leibniz Universität Hannover, 2016.
- [121] G. M. Müller, M. Römer, J. Hübner, and M. Oestreich, “Efficient data averaging for spin noise spectroscopy in semiconductors”, *Appl. Phys. Lett.* **97**, 192109 (2010).
- [122] M. Fox, *Quantum Optics: An Introduction*, Oxford University Press, 2006.
- [123] J. Wiegand, D. S. Smirnov, J. Hübner, M. M. Glazov, and M. Oestreich, “Spin and reoccupation noise in a single quantum dot beyond the fluctuation-dissipation theorem”, *Phys. Rev. B* **97**, 081403(R) (2018).
- [124] V. S. Zapasskii, A. Grelich, S. A. Crooker, Y. Li, G. G. Kozlov, D. R. Yakovlev, D. Reuter, A. D. Wieck, and M. Bayer, “Optical Spectroscopy of Spin Noise”, *Phys. Rev. Lett.* **110**, 176601 (2013).
- [125] P. Glasenapp, D. S. Smirnov, A. Grelich, J. Hackmann, M. M. Glazov, F. B. Anders, and M. Bayer, “Spin noise of electrons and holes in (In,Ga)As quantum dots: Experiment and theory”, *Phys. Rev. B* **93**, 205429 (2016).



- [126] D. S. Smirnov, M. M. Glazov, E. L. Ivchenko, and L. Lanco, “Theory of optical spin control in quantum dot microcavities”, *Phys. Rev. B* **92**, 115305 (2015).
- [127] D. S. Smirnov, B. Reznichenko, A. Auffèves, and L. Lanco, “Measurement back action and spin noise spectroscopy in a charged cavity QED device in the strong coupling regime”, *Phys. Rev. B* **96**, 165308 (2017).
- [128] G. Compagno, R. Passante, and F. Persico, *Atom-field interactions and dressed atoms*, volume 17 of *Cambridge studies in modern optics*, Cambridge University Press, 2005.
- [129] T. Nakaoka, T. Saito, J. Tatebayashi, and Y. Arakawa, “Size, shape, and strain dependence of the  $g$  factor in self-assembled In(Ga)As quantum dots”, *Phys. Rev. B* **70**, 235337 (2004).
- [130] C. Gerry and P. Knight, *Introductory Quantum Optics*, Cambridge University Press, 2004.
- [131] A. V. Kuhlmann, J. Houel, D. Brunner, A. Ludwig, D. Reuter, A. D. Wieck, and R. J. Warburton, “A dark-field microscope for background-free detection of resonance fluorescence from single semiconductor quantum dots operating in a set-and-forget mode”, *Rev. Sci. Instrum.* **84**, 073905 (2013).
- [132] M. Bayer, A. Kuther, A. Forchel, A. Gorbunov, V. B. Timofeev, F. Schäfer, J. P. Reithmaier, T. L. Reinecke, and S. N. Walck, “Electron and Hole  $g$  Factors and Exchange Interaction from Studies of the Exciton Fine Structure in  $\text{In}_{0.60}\text{Ga}_{0.40}\text{As}$  Quantum Dots”, *Phys. Rev. Lett.* **82**, 1748 (1999).
- [133] M. J. Stanley, C. Matthiesen, J. Hansom, C. Le Gall, C. H. H. Schulte, E. Clarke, and M. Atatüre, “Dynamics of a mesoscopic nuclear spin ensemble interacting with an optically driven electron spin”, *Phys. Rev. B* **90**, 195305 (2014).

- [134] A. Baldereschi and N. O. Lipari, “Spherical Model of Shallow Acceptor States in Semiconductors”, *Phys. Rev. B* **8**, 2697 (1973).
- [135] R. J. Warburton, C. Schäfflein, D. Haft, F. Bickel, A. Lorke, K. Karrai, J. M. Garcia, W. Schoenfeld, and P. M. Petroff, “Optical emission from a charge-tunable quantum ring”, *Nature* **405**, 926 (2000).
- [136] M. Baier, F. Findeis, A. Zrenner, M. Bichler, and G. Abstreiter, “Optical spectroscopy of charged excitons in single quantum dot photodiodes”, *Phys. Rev. B* **64**, 195326 (2001).
- [137] F. Li, Y. V. Pershin, V. A. Slipko, and N. A. Sinitsyn, “Nonequilibrium Spin Noise Spectroscopy”, *Phys. Rev. Lett.* **111**, 067201 (2013).
- [138] F. Berski, H. Kuhn, J. G. Lonnemann, J. Hübner, and M. Oestreich, “Ultrahigh Bandwidth Spin Noise Spectroscopy: Detection of Large g-Factor Fluctuations in Highly-n-Doped GaAs”, *Phys. Rev. Lett.* **111**, 186602 (2013).
- [139] L. Yang, P. Glasenapp, A. Greulich, D. Reuter, A. D. Wieck, D. R. Yakovlev, M. Bayer, and S. A. Crooker, “Two-colour spin noise spectroscopy and fluctuation correlations reveal homogeneous linewidths within quantum-dot ensembles”, *Nature Communications* **5**, 4949 (2014).
- [140] J. M. LaForge and G. M. Steeves, “Noninvasive optical amplification and detection of Faraday rotation”, *Appl. Phys. Lett.* **91**, 121115 (2007).
- [141] J. M. LaForge and G. M. Steeves, “A Mach-Zehnder interferometer for the detection and noninvasive optical amplification of polarization rotation”, *Rev. Sci. Instrum.* **79**, 063106 (2008).
- [142] S. Cronenberger and D. Scalbert, “Quantum limited heterodyne detection of spin noise”, *Rev. Sci. Instrum.* **87**, 093111 (2016).

- [143] M. Y. Petrov, A. N. Kamenskii, V. S. Zapasskii, M. Bayer, and A. Grelich, “Increased sensitivity of spin noise spectroscopy using homodyne detection in  $n$ -doped GaAs”, *Phys. Rev. B* **97**, 125202 (2018).
- [144] P. Sterin, J. Wiegand, J. Hübner, and M. Oestreich, “Optical Amplification of Spin Noise Spectroscopy via Homodyne Detection”, *Phys. Rev. Appl.* **9**, 034003 (2018).



# List of Figures

2.1.	QD dimensions and bandstructure . . . . .	21
2.2.	Optical transitions of neutral and charged exciton . . . . .	25
2.3.	Auger effect and charge fluctuations . . . . .	29
2.4.	The Bloch sphere . . . . .	32
2.5.	Hyperfine interaction of electrons and holes in QDs . . . . .	35
2.6.	Principle of spin noise spectroscopy . . . . .	39
2.7.	Spin noise autocorrelation and power spectral density . . . . .	41
2.8.	Circular dichroism and birefringence . . . . .	44
2.9.	Faraday and Kerr rotation noise power . . . . .	46
3.1.	Sample characteristics . . . . .	50
3.2.	Low-temperature confocal microscope . . . . .	55
3.3.	Single QD PL spectrum . . . . .	58
3.4.	SN spectrum and schematic of spin projection . . . . .	63
3.5.	Background noise and detector response function . . . . .	66
4.1.	Homogeneous noise power spectrum . . . . .	71
4.2.	Spin noise frequency spectra . . . . .	73
4.3.	Power spectra and correlation rates of the two noise contributions . . . . .	74
4.4.	QD states and transitions of the theoretical model . . . . .	76
4.5.	Nonequilibrium spin dynamics . . . . .	81
4.6.	Magnetic field dependence of the occupation noise . . . . .	85
4.7.	Occupation dynamics . . . . .	87
4.8.	Kerr rotation noise spectra with 3 contributions . . . . .	92
4.9.	Noise power as a function of magnetic field and laser detuning . . . . .	93
4.10.	Model of Acceptor-occupation noise . . . . .	96
4.11.	Calculated Kerr rotation noise spectra . . . . .	105

4.12. Spin polarization and QD occupation . . . . .	108
A.1. PL and reflectivity of the cavity . . . . .	120
A.2. Side PL at different QD densities . . . . .	121
B.1. Charge dynamics model without Coulomb repulsion	124
B.2. Charge dynamics model with Stark shift of the QD resonance: noise spectrum . . . . .	127
B.3. Charge dynamics model with Stark shift of the QD resonance: noise power . . . . .	129

# Curriculum Vitae

**Julia Susan Wiegand,**  
born September 14th, 1988 in Hannover

- 2016 - today**    Employment as a research assistant at the  
Institute for Solid State Physics of the  
Leibniz Universität Hannover (LUH)
- 2013 - 2016**    Scholarship as a fellow of the Hannover  
School for Nanotechnology
- 2013 - today**    Preparation of the Dissertation at the In-  
stitute for Solid State Physics of the LUH,  
supervised by Prof. Dr. M. Oestreich
- Nov. 2013**        MSc degree in physics at the LUH
- Oct. 2011**        BSc degree in physics at the LUH
- 2008 - 2013**     Study of physics at the LUH
- June 2008**        Abitur at the Gymnasium Goetheschule in  
Hannover
- 1995 - 2008**     School education





# List of Publications

- **J. Wiegand**, D. S. Smirnov, J. Osberghaus, L. Abaspour, J. Hübner, and M. Oestreich, *Hole-capture competition between a single quantum dot and an ionized acceptor*, Phys. Rev. B **98**, 125426 (2018).
- **J. Wiegand**, D. S. Smirnov, J. Hübner, M. M. Glazov, and M. Oestreich, *Spin and reoccupation noise in a single quantum dot beyond the fluctuation-dissipation theorem*, Phys. Rev. B **97**, 081403(R) (2018).
- P. Sterin, **J. Wiegand**, J. Hübner, and M. Oestreich, *Optical amplification of spin noise spectroscopy via homodyne detection*, Phys. Rev. Applied **9**, 034003 (2018).
- A. Rinn, T. Breuer, **J. Wiegand**, M. Beck, J. Hübner, R. C. Döring, M. Oestreich, W. Heimbrodt, G. Witte, and S. Chatterjee, *Interfacial molecular packing determines exciton dynamics in molecular heterostructures: the case of pentacene-perfluoropentacene* ACS Appl. Mater. Interfaces **9** (48), 42020 (2017).
- J. Aprojanz, B. Dreyer, M. Wehr, **J. Wiegand**, J. Baringhaus, J. Koch, F. Renz, R. Sindelar, and C. Tegenkamp, *Highly anisotropic electric conductivity in PAN-based carbon nanofibers*, J. Phys.: Condens. Matter **29**, 494002 (2017).
- J. Baringhaus, J. Aprojanz, **J. Wiegand**, D. Laube, M. Halbauer, J. Hübner, M. Oestreich, and C. Tegenkamp, *Growth and characterization of sidewall graphene nanoribbons*, Appl. Phys. Lett. **106**, 043109 (2015).

- J. Hübner, R. Dahbashi, F. Berski, **J. Wiegand**, H. Kuhn, J. Lonnemann, and M. Oestreich, *Spin noise spectroscopy in semiconductors: from a billion down to single spins*, Proc. SPIE **9167**, Spintronics VII, 91672R (2014).

# Contributions to Scientific Conferences

- J. Wiegand, R. Dahbashi, J. Hübner, K. Pierz, and M. Oestreich, *Spin noise spectroscopy on single InAs quantum dots* (Poster), DPG Spring Meeting of the Condensed Matter Section, Regensburg (2016).
- J. Wiegand, R. Dahbashi, J. Hübner, K. Pierz, and M. Oestreich, *Spin noise spectroscopy on single InAs quantum dots* (Poster), International Winterschool on New Developments in Solid State Physics, Mauterndorf (2016).
- J. Wiegand, D. Unruh, J. Hübner, F. Renz, and M. Oestreich, *Optical spectroscopy of spin state switching in metal-organic complexes* (Poster), NanoDay of the Laboratory for Nano and Quantum Engineering, Hannover (2015).
- J. Wiegand, R. Dahbashi, J. Hübner, K. Pierz, A. Ludwig, A. Wieck, and M. Oestreich, *Spin noise spectroscopy on single InAs quantum dots* (Poster), DPG Spring Meeting of the Condensed Matter Section, Berlin (2015).
- J. Wiegand, R. Dahbashi, H. Kuhn, J. Hübner, and M. Oestreich, *Optical Determination of spin dynamics in distinct nanostructures* (Poster), NanoDay of the Laboratory for Nano and Quantum Engineering, Hannover (2014).
- J. Wiegand, R. Dahbashi, C. Mayer, J. Hübner, D. Schaadt, and M. Oestreich, *Optical spectroscopy of site-controlled InAs quantum dots* (Poster), DPG Spring Meeting of the Condensed Matter Section, Dresden (2014).



# Acknowledgements

First of all, I would like to thank my supervisor Prof. Dr. Michael Oestreich for giving me the opportunity to do a PhD in his group and for providing many exciting research topics. Thank you very much for the supervision, support and many helpful discussions during the last years!

I would like to thank Prof. Dr. Fei Ding for being the second reviewer and I thank Prof. Dr. Daniel Hägele for being the external reviewer, especially considering the short notice. Furthermore, I thank Prof. Dr. Klemens Hammerer for heading the examination committee.

Special thanks go to Dr. Ramin Dabhashi who designed and set up the [QD SNS](#) microscope, performed the very first measurements on single [QDs](#) and supervised my first attempts in conducting the [SNS](#) measurements. I really enjoyed working together in the lab with you and I learned a lot from you!

Great measurements are of small value if you can't explain them properly. I am very thankful for a fruitful collaboration with Prof. Dr. Mikhail Glazov and Dr. Dmitry Smirnov who enabled the theoretical analysis of the nonequilibrium [SN](#) measurements. In particular, I thank Dmitry for his very productive visit in Hannover, many long enjoyable skype sessions, and a lot of detailed theory explanations. I have benefitted a lot from our collaboration, thank you so much!

I would like to specially thank PD Dr. Jens Hübner for ensuring a pleasant working atmosphere and for always finding time to help, although there are often many students with many issues at the same time. Thank you for many tips and tricks in the lab, your active involvement in solving complex data analysis problems, numerous helpful discussions and many encouraging words!

I thank PD Dr. Jens Hübner, Dr. Dmitry Smirnov and Dr. Carsten Schulte for proofreading the thesis and providing many helpful comments and suggestions.

I thank Jakob Osberghaus and André Frauendorf for their contribution to the presented results in the framework of their Bachelor's thesis. I also thank Lida Abaspour for joining the [QD](#) measurements for a couple of weeks. I enjoyed working together with the three of you!

I thank Pavel Sterin for his help with computer issues of all kinds and especially for his improvements on the [FFT](#) software. It has never again produced an error since your update! I also thank Michael Beck, Dr. Hendrik Kuhn and Dr. Jan-Gerrit Lonnemann for being always motivated to discuss physics beyond their own research projects and for many good ideas, suggestions and explanations. I thank Dr. Fabian Berski for many helpful tips in the lab and an introduction to programming.

I specially thank my office mates: Ramin, Hendrik, Christopher, André, Michi, Magnus, Pavel and Lida, for making the office a great place to spend time at. Thank you for many dart turns, extensive Radio-21 listening, a lot of cookies and cake, office modification activities, photoshop masterpieces, and at least one joke a day. It was a terrific time with you!

Furthermore, I thank all members and former members of the nanostructures group for a nice and friendly working atmosphere and especially Prof. Dr. Rolf Haug for always having an open door and for taking an active interest in everybody's problems and worries.

I thank the Hannover School for Nanotechnology for financial support in my first years as a PhD student and for offering many interesting seminars and workshops. In this context, I would like to thank Dr. Fritz Schulze-Wischeler for the great organization, his personal commitment and an open ear for all questions and wishes.

I also thank the research training group "Quantum mechanical noise in complex systems" for providing many interesting seminars with great invited speakers and a lot of valuable PhD-student activities.

Finally, I thank my parents for always supporting and encouraging me in whatever I do. Mama und Papa, danke für alles!

Most of all, I thank Carsten for being at my side. Thank you so much for your support, for always being understanding, for cheering me up whenever I'm not doing well, and for the many happy moments together! I look forward to spending the rest of my life with you.